


1990

Design of an expert system for failed fuel identification and surveillance in EBR-II

Ramin Mikaili
Iowa State University

Follow this and additional works at: <https://lib.dr.iastate.edu/rtd>

 Part of the [Artificial Intelligence and Robotics Commons](#), and the [Nuclear Engineering Commons](#)

Recommended Citation

Mikaili, Ramin, "Design of an expert system for failed fuel identification and surveillance in EBR-II " (1990). *Retrospective Theses and Dissertations*. 9863.
<https://lib.dr.iastate.edu/rtd/9863>

This Dissertation is brought to you for free and open access by the Iowa State University Capstones, Theses and Dissertations at Iowa State University Digital Repository. It has been accepted for inclusion in Retrospective Theses and Dissertations by an authorized administrator of Iowa State University Digital Repository. For more information, please contact digirep@iastate.edu.

91

10536

U·M·I

MICROFILMED 1991

INFORMATION TO USERS

The most advanced technology has been used to photograph and reproduce this manuscript from the microfilm master. UMI films the text directly from the original or copy submitted. Thus, some thesis and dissertation copies are in typewriter face, while others may be from any type of computer printer.

The quality of this reproduction is dependent upon the quality of the copy submitted. Broken or indistinct print, colored or poor quality illustrations and photographs, print bleedthrough, substandard margins, and improper alignment can adversely affect reproduction.

In the unlikely event that the author did not send UMI a complete manuscript and there are missing pages, these will be noted. Also, if unauthorized copyright material had to be removed, a note will indicate the deletion.

Oversize materials (e.g., maps, drawings, charts) are reproduced by sectioning the original, beginning at the upper left-hand corner and continuing from left to right in equal sections with small overlaps. Each original is also photographed in one exposure and is included in reduced form at the back of the book.

Photographs included in the original manuscript have been reproduced xerographically in this copy. Higher quality 6" x 9" black and white photographic prints are available for any photographs or illustrations appearing in this copy for an additional charge. Contact UMI directly to order.

U·M·I

University Microfilms International
A Bell & Howell Information Company
300 North Zeeb Road, Ann Arbor, MI 48106-1346 USA
313/761-4700 800/521-0600



Order Number 9110536

**Design of an expert system for failed fuel identification and
surveillance in EBR-II**

Mikaili, Ramin, Ph.D.

Iowa State University, 1990

U·M·I

**300 N. Zeeb Rd.
Ann Arbor, MI 48106**



**Design of an expert system for failed fuel identification
and surveillance in EBR-II**

by

Ramin Mikaili

A Dissertation Submitted to the
Graduate Faculty in Partial Fulfillment of the
Requirements for the Degree of
DOCTOR OF PHILOSOPHY

Department: Mechanical Engineering
Major: Nuclear Engineering

Approved:

Signature was redacted for privacy.

In Charge of Major Work

Signature was redacted for privacy.

For the Major Department

Signature was redacted for privacy.

For the Graduate College

Iowa State University
Ames, Iowa
1990

TABLE OF CONTENTS

LIST OF ABBREVIATIONS	viii
CHAPTER 1. INTRODUCTION	1
Plant Layout of EBR-II	1
Introduction to Expert Systems	5
Definition of Important Terms	10
Run Beyond Clad Breach Program	12
Scope of the Project	13
CHAPTER 2. TAG GAS METHOD FOR FAILED FUEL IDENTIFICATION	17
Xenon Tag Method	17
Ratio of Fission Gas to Tag Gas for Diagnosis	20
Ratio of ^{131}Xe to ^{134}Xe Used for Diagnosis	21
Vector Technique Used for Identification of Simultaneous Tags	22
Barycentric-Coordinate Technique	28
Description of the Technique in Two Dimensions	28
The Barycentric Technique in N Dimensions	32
Evaluation of TG Analysis	34

CHAPTER 3. USE OF DELAYED NEUTRON SIGNALS FOR SELECTION AND SURVEILLANCE OF FAILED FUEL ELE- MENTS IN FAST REACTORS	36
Delayed Neutron Detection System	37
Analytical Method Used in GIRAFFE	39
Derivation of the Equation Used for Calculating DN Activity	40
Background Count Considerations	44
Statistical Method Used for Determining Transit and Holdup Time	45
Determination of the Surface Area of the Defect Site	46
Evaluation of GIRAFFE	51
CHAPTER 4. DESCRIPTION OF FISSION GAS ANALYSIS	54
Fission Gas Detection System	55
Development of the Analytical Model for Fission Gas Analysis	57
Fission Gas Transport Equations Corrected for Cover Gas Purging	57
Cumulative ^{133}Xe Release	61
Release-to-Birth Ratio	62
Determination of the Degassing Constant	65
Determination of the Cover Gas Loss Rate	69
Evaluation of Fission Gas Analysis	70
CHAPTER 5. CHARACTERISTICS OF FISSION GAS STOR- AGE AND RELEASE	72
Radiation Effects on Metal and Oxide Fuel Elements	74
Radiation Effects on Metal Fuel	75
Radiation Effects on Mixed-Oxide Fuel	85

Description of the Diagnostic Tools Provided by FG Analysis	86
FG Analysis of Breached Elements (May 1986 to April 1990)	89
Analysis of Breached Elements in 1986	92
Analysis of Breached Elements in 1987	97
Analysis of Breached Elements in 1988	101
Analysis of Breached Elements in 1989 and 1990	102
CHAPTER 6. DERIVATION OF RULES FROM INDUCTIVE	
LEARNING	105
Basic Description of 1st Class Fusion	105
The Inductive Inference Engine	110
Derivation of Rules for FG Analysis	116
CHAPTER 7. DESIGN OF THE EXPERT SYSTEM AND SUG-	
GESTIONS FOR FUTURE DIRECTION	127
CHAPTER 8. ACKNOWLEDGMENTS	131
BIBLIOGRAPHY	133
APPENDIX PLOTS OF FG ANALYSIS FROM MAY OF 1986	
TO APRIL OF 1990	136

LIST OF FIGURES

Figure 1.1:	Principal EBR-II facilities. Shown from left to right are the sodium boiler, the reactor and its containment building, and the power plant building	3
Figure 1.2:	Cutaway view of EBR-II reactor and primary cooling system	4
Figure 2.1:	Planar display of six tag nodes and three simultaneous breaches.	24
Figure 2.2:	Transformation from Cartesian coordinates to barycentric-coordinates system.	30
Figure 3.1:	DND configuration for on-line characterization of DN signals	38
Figure 3.2:	Plot of five pairs of measured and predicted DN activities and the best-fit line.	47
Figure 5.1:	The effect of irradiation on 0 – <i>Pu</i> metal fuel	76
Figure 5.2:	The effect of irradiation on 8 – <i>Pu</i> metal fuel	77
Figure 5.3:	The effect of irradiation on 20 – <i>Pu</i> metal fuel	78
Figure 5.4:	A typical design of a MK-II fuel element	79
Figure 5.5:	A typical weld breach in a metal fuel element	80
Figure 5.6:	Metal fuel gas and DN emitters release characteristics	82
Figure 5.7:	A typical pre-thinned fuel column breach in a metal fuel element	83

Figure 5.8:	A typical dimple breach in a MK-II metal fuel element	84
Figure 5.9:	The corrected and not corrected-for-purging activity of ^{133}Xe	87
Figure 5.10:	The corrected and not corrected-for-purging activity of ^{87}Kr	88
Figure 5.11:	An arbitrary surface response of release to birth ratio and decay constant for seven FG isotopes with time lapse of irradiation	90
Figure 6.1:	One-level decision tree	112
Figure 6.2:	Two-level decision tree	112
Figure 6.3:	Decision tree with class names	113
Figure 6.4:	Partial decision tree	115
Figure 6.5:	Binary attribute discrimination	116
Figure 6.6:	A listing of the definitions, values, and final results	118
Figure 6.7:	The listing of examples	120
Figure 6.8:	The rule tree for FG analysis	121
Figure 6.9:	Query session report of breach 1	123
Figure 6.10:	Query session report of breach 9	124
Figure 6.11:	Query session report of breach 22	125
Figure 6.12:	Query session report of breach 34	126
Figure 7.1:	Schematic of the design of the expert system	129

LIST OF TABLES

Table 2.1:	Geometric and physical properties of C_3 solution vector . . .	31
Table 5.1:	Listing of breaches in 1986	93
Table 5.2:	Listing of breaches in 1987	98
Table 5.3:	Listing of breaches in 1988	102
Table 5.4:	Listing of breaches in 1989 and 1990	103
Table 6.1:	Examples and Classes	111

LIST OF ABBREVIATIONS

AI:	artificial intelligence
CGCS:	cover gas cleanup system
DAS:	data acquisition system
DN:	delayed neutron
EBR-II:	experimental breeder reactor-II
ES:	expert system
FCMI:	fuel clad mechanical interaction
FERD:	fuel-element rupture detector
FG:	fission gas
FPS:	fission product source
GIRAFFE:	general isotope release analysis for failed element
GLASS:	germanium lithium argon scanning system
IFR:	integral fast reactor
KB:	knowledge base
LMR:	liquid metal reactor
RBCB:	run beyond clad breach
TG:	tag gas

CHAPTER 1. INTRODUCTION

In recent years, a great deal of attention has been given to the generation of electrical power from nuclear power plants in the U.S. Perhaps this is motivated by the catastrophic effects on the ecology of burning fossil fuel for energy production. So far, the efforts have mainly been put into research and development of new nuclear reactor designs. In the new designs, the shortcomings of the old designs are recognized and corrected by exploring latest technologies.

By performing the safety analysis of typical nuclear power plants in operation today, it has been found that the largest contributing factor in most accidents is human error. The automation of control of new nuclear power plants is then a step in the right direction. In an effort to automate the plant operation in normal or abnormal situations, the field of artificial intelligence (AI) has been explored extensively.

In this project we have been taking part in this effort by developing an ES for diagnosing failed fuel elements in EBR-II. Before the scope of this project is outlined, it is perhaps useful to familiarize the reader with EBR-II, to define ES, and to describe the generic basis for developing an ES.

Plant Layout of EBR-II

“Now in its third decade of operation, EBR-II continues to serve the na-

tion as a facility for testing fuels, materials, and instruments of interest to the breeder reactor community. In addition, it has assumed an important role in plant systems testing. Designed and build with the technologies of the 1950s and 1960s, EBR-II stands as a tribute to those scientists and engineers whose imagination, competence, and initiative have transformed a visionary concept into operational reality” [1].

The plant layout of EBR-II is depicted in Figure 1.1, and in Figure 1.2, a cut-away view with the primary cooling system is shown. A brief description of its operation is given in the following discussion. The EBR-II plant consists of three principal facilities that house the reactor, steam generation system, and power plant. Heat generated in the core is removed by sodium coolant which is pumped through the core, into a primary-to-secondary heat exchanger, and discharged directly to the sodium filled primary tank. The heated secondary coolant is pumped from the heat exchanger to the sodium-boiler building where steam is produced and superheated. The superheated steam, in turn, is used to drive a turbine-generator located in the power plant building. Condensate along with makeup water is returned to the sodium-boiler building for steam generation. After losing its heat to the steam generation system, secondary coolant is pumped back to the heat exchanger in the reactor tank to complete the cycle. In effect, the reactor is a 62.5MW source of heat which is used to provide steam for electrical power generation.

A feature original with the design of EBR-II is the pool-type concept, based on the complete submersion under molten sodium of the reactor core, reflector, blanket, neutron shield, primary pumps, primary piping, heat exchanger, and in-vessel fuel handling equipment. The primary role of EBR-II is now focused on development

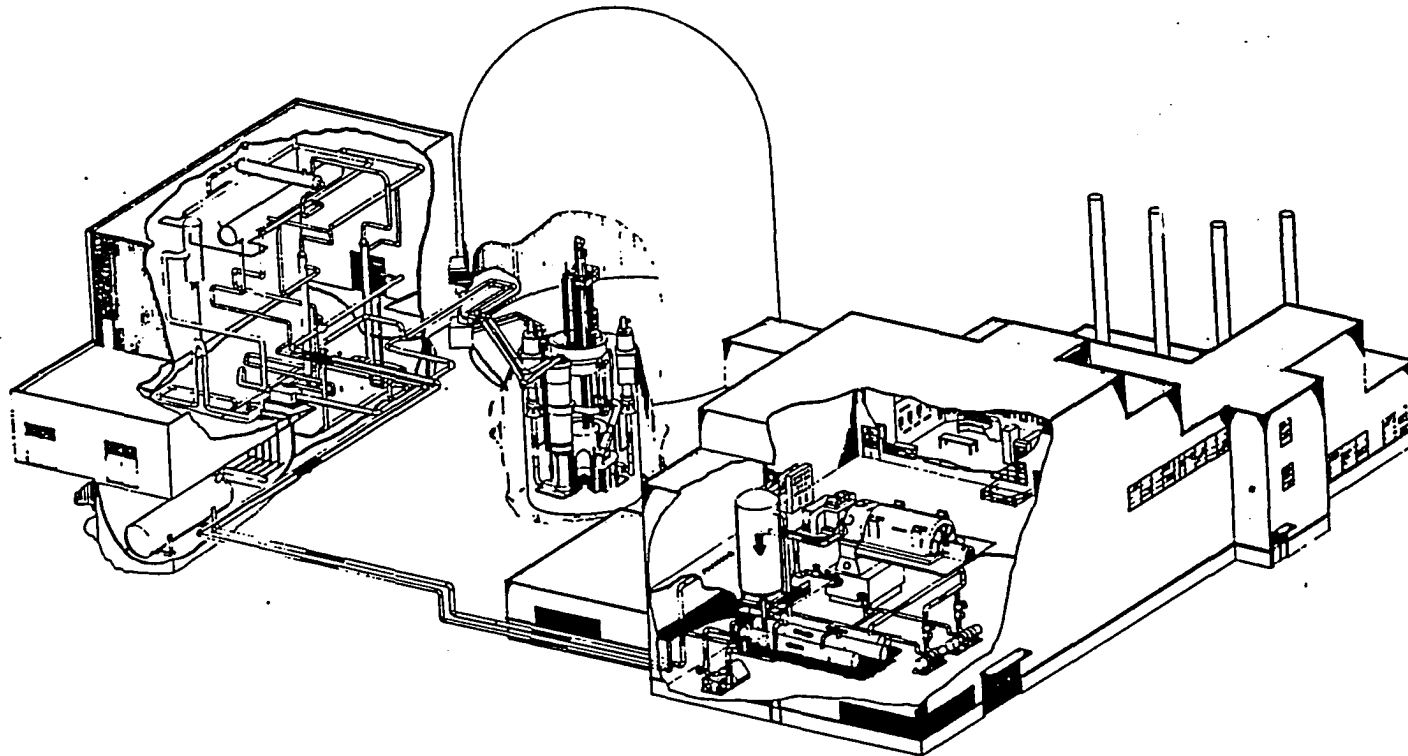


Figure 1.1: Principal EBR-II facilities. Shown from left to right are the sodium boiler, the reactor and its containment building, and the power plant building

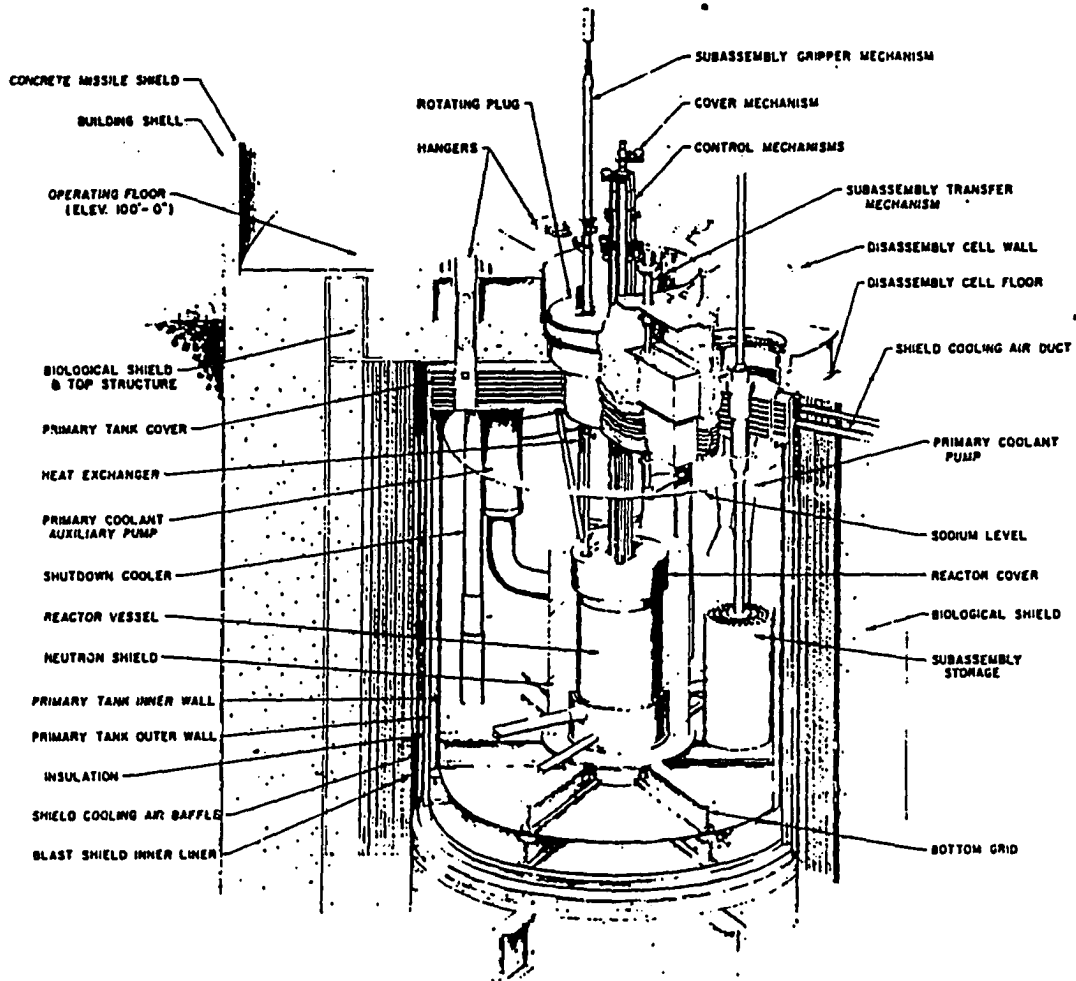


Figure 1.2: Cutaway view of EBR-II reactor and primary cooling system

and testing of metallic and oxide fuel for the Integral Fast Reactor (IFR) concept at Argonne National Laboratory. The IFR concept is one of the primary candidates for the new generation of nuclear power plants in the U.S. EBR-II is being used for plant dynamics testing to demonstrate passive (inherent) safety features and passive control capabilities of a metal fueled, liquid metal cooled fast reactor. Ultimately, the knowledge gained in EBR-II will be incorporated in the final development of the IFR concept. The newest area of work at EBR-II is in the development and testing of computer-based diagnostic techniques. The concepts developed in this work may be extended so that the methods can be used not only in the liquid metal fast breeder reactors, but also in light water reactors which are commercially in use today in the U.S. for power generation.

Introduction to Expert Systems

AI is the part of computer science concerned with designing intelligent computer systems, that is, systems that exhibit the characteristics we associate with intelligence in human behavior (e.g., understanding language, learning, reasoning, solving problems) [2].

With all the research done to this day, the AI field still has not yet accomplished its stated task of creating programs that exhibit reasoning and learning processes similar to humans. However, it must be noted that the shortcomings of the AI field are mostly blamed on the lack of understanding of how the human brain actually works. To this day, AI researchers have had to guess on how a human brain works. It has been stated [3],

“Although the AI field has been an active one for more than 25 years,

AI researchers still have no idea how to create a truly intelligent computer. No existing programs can recall facts, solve problems, reason, learn, or process language with anything approximating human facility. This lack of success has occurred not because computers are inferior to human brains but because we do not yet know how human intelligence is organized.”

On the other hand, it is ironic that the psychology field has actually used some AI concepts to develop psychological theories, as is also stated in Anderson [3].

“... observing how we could analyze the intelligent behavior of a machine has largely liberated us from our inhibitions and misconceptions about analyzing our own intelligence.”

Nevertheless, one can not deny the successes of research in the AI field. As a matter of fact, in the beginning of the 1970s, it was believed that the capability to produce a program which has human-like intelligence compatibilities was imminent [4], but difficulties were encountered in generalizing these successes into flexible, intelligent programs. Even with the 1970s computers, which had larger memory and much increased computer speed than those of the 1960s, it was soon found that AI programs exhausted computer memory, or that the execution time became too long. This led the AI field to produce more efficient methods for solving AI problems, which in turn led to the introduction of the first commercial product, the ES. A new era in AI history began, augmented by the development of MYCIN, one of the first ES. MYCIN was developed at Stanford University to help physicians diagnose illnesses [4]. Mostly due to the success of MYCIN, the possibilities of developing ES in many

other fields of technology have been or are being explored. Development of ES is one of the fields of AI being extensively explored today.

The most commonly used definition of an ES, “a computer program which mimics human experts,” is accurate but imprecise. It overlooks the fact that most human experts cannot clearly explain their train of thought in solving some problems. Therefore, in order to complete the above definition, the ES can precisely be said to be, “a computer program based on a well defined body of knowledge related to a specific problem area, which mimics human experts.”

The major insight gained from early work in problem-solving was the importance of domain-specific knowledge [5]. An engineer, for example, in diagnosing a malfunction in an auxiliary cooling system of a nuclear power plant, is not successful if she solely uses her innate problem-solving skills; she is effective because she employs her theoretical and empirical knowledge about the cooling system. In other words, expert knowledge is a combination of theoretical understanding of the problem with a collection of heuristic problem-solving rules that experience has shown to be effective in the domain. Thus, ES are constructed by obtaining this knowledge from a human expert and coding it into a form that a computer may apply to similar problems.

Although some ES are developed by the domain experts themselves, it is often more feasible to do this as a collaborative effort between domain experts and a separate AI specialist. The domain experts provide the necessary knowledge of the problem domain through a general discussion of their problem-solving methods and by demonstrating those skills on a carefully chosen set of sample problems. The AI specialists (who are frequently referred to as *knowledge engineers*) are responsible for implementing this knowledge in a program that is both effective and seemingly

intelligent in its behavior [5].

The knowledge engineer is sometimes aided by ES tools called shells. Shells are computer programs, developed for storing the knowledge of the domain experts in the form of rules; this allows the domain expert to refine the KB through a process of giving it example problems to solve. The KB developed by the domain expert can then be queried by the user through the shell. Also, similar to domain experts gaining expertise by experience, shells must allow modification of the KB as new information is obtained. The processes of storing and refining the KB by the domain expert and querying the KB by the user has to be facilitated in a user-friendly fashion, since, in developing the shell, it must be assumed that neither the user nor the domain expert has the required knowledge in computer programming. Therefore, it is easily recognized that the use of a successful shell is restricted to a given domain of knowledge.

The knowledge acquired from domain experts will be organized as a collection of rules (rules of thumb or heuristic rules) which allow the ES to draw conclusions from given data or premises, and thereby offer intelligent advice or make intelligent decisions. The procedure of drawing conclusions from the knowledge is conducted by the "inference mechanism" of the ES [6]. In short, be it developed by a domain expert or a knowledge engineer, ES are mainly composed of a KB and an inference mechanism (or inference engine). The most common type of knowledge used by the domain experts can be formalized as heuristic rules [3].

In most ES developed for diagnostic problems, it is required that a combination of heuristics and algorithms be stored as KB. Algorithms are procedures designed to result in the correct solution of problems and are used for solving problems in con-

ventional programs. For example, the procedure for multiplication is an algorithm. By following the same procedure, one would obtain the correct product of any two numbers. A comparison of algorithms and heuristic is as follows: algorithms provide brute force methods of solving problems which, if followed exactly, will result in the correct answer; whereas heuristics are short cuts for solving problems but do not always result in the correct solution (sometimes it does not rain on a cloudy day). Then, why is there a need for using heuristics? The answer lies in the fact that there is not an algorithm for every problem. For example, there is not a systematic way of predicting rain which always gives the correct forecast. Also, for some problems, the knowledge used (accumulated from experience and theoretical background) is so complex that formalizing an algorithm is very difficult, at times impossible, and sometimes results in an unacceptably long time for computation. Thus, an ES developed for diagnostic purposes must allow both for storing algorithms of analytical models and for using heuristic rules in the KB.

The inference engine is used to reach conclusions and to control the reasoning process [6]. In simpler words, it is the part of the ES which thinks through the knowledge it has acquired. Inference mechanisms are of either a deterministic or a probabilistic type. When one deals with a knowledge area where assertions are certain, deterministic inference engines are used. On the other hand, probabilistic inference engines deal with the type of knowledge for which an assertion is associated with an assigned probability. The majority of knowledge areas are probabilistic, but for many of these areas, the uncertainty is statistically insignificant, so a deterministic inference engine is most commonly used [6]. Probabilistic or deterministic inference engines use either forward- or backward-chaining methods.

Forward-chaining is the term used to describe the process of working forward from the evidence to the conclusions, whereas, backward-chaining is working from hypothesis to evidence. The latter starts with an object and requests information to confirm or deny it. Thus, it is sometimes called object-driven because the system begins with an object and tries to verify it. The distinction between forward and backward chaining is logically related to the distinction between mathematical proofs by deduction or induction. In most ES developed for diagnostic purposes, the backward-chaining inference mechanism is used.

Finally, the “human window”, through which ES interacts with the user, should not be overlooked. Most tools for developing ES provide excellent graphics capabilities and window systems. Since ES are competing with the domain experts’ human interactive capabilities, full exploration of this aspect is crucial.

Definition of Important Terms

The terms, DN, FG, and breach types are explained in the following discussion:

- After the discovery of nuclear fission it was considered that some fission fragments having a large excess of neutrons over stable isotopic nuclei should emit prompt neutrons either at the instant of fission or very soon after. However, some fission fragments undergo several steps of β -decay and finally reach a state where de-excitation by neutron emission is possible. The fission products which undergo β -emission and their decay daughters that finally reach a stable state by neutron emission are respectively called DN precursors.

- The gaseous fission products, FG, are insoluble in the fuel matrix, thus they tend to form bubbles. The rate at which bubbles are formed is generally very high. After birth, bubbles either grow and contribute to fuel swelling or they migrate to free surfaces where the gas is released into the volume bounded by the cladding [7]. The radioactivity of the FG released to the cover gas (which is caused by the breaching of clad) is measured and used for performing the FG analysis.
- The term “clad breach” is a generic term used to indicate fuel clad failure. In general the axial forces which cause clad breach in the fuel column are of two types [8]: the stress caused by accumulation of FG in fuel and the stress induced by swelling of the fuel. By FG analysis, we hope to distinguish between three types of breach: creep-rupture, FCMI, and birth defect. The breach of either creep-rupture or FCMI type is caused by swelling of the clad and accumulation of FG in the fuel. However, in FCMI, the gap between the fuel and clad is closed; thus, the fuel and clad interact mechanically and perhaps chemically. On the other hand, in creep-rupture, there is still a gap between the fuel and clad when breach occurs. Finally, the birth defect is caused by errors in welding. This breach is considered benign, since welding is applied only in the upper region of fuel elements and fuel elements in EBR-II are partially immersed into the sodium pool. Therefore, there is a small probability of sodium/fuel interaction in weld breaches.

Run Beyond Clad Breach Program

A program has been underway at EBR-II since 1977 to evaluate the post-cladding-breach performance of metal and mixed-oxide fuel elements. This activity is called the RBCB program. Interest in this program derives from the fact that oxide fuel in contact with sodium reacts chemically to form a lower-density reaction product. Since it was assumed from an economics basis that fuel elements in LMR would have to operate beyond the point of initial breach of cladding, questions arose in the areas of reaction kinetics and thermodynamics, event detection, and primary system contamination. The RBCB program was designed from its inception to address these questions. In 1981 a contract was signed between the U.S. Department of Energy and the Power Reactor and Nuclear Fuel Development Corporation of Japan for joint support of the RBCB program. Argonne is also undertaking work in RBCB testing of IFR metal fuel in EBR-II [9].

In 1975 preparations were begun for irradiation of experimental elements in EBR-II to beyond the point of initial breach of cladding. This type of irradiation evolved rapidly into the present RBCB program. The major problem encountered in preparing the facility for such testing was leakage of cover gas up into the reactor building. A noble gas, argon, is used as the cover gas above the sodium coolant in EBR-II. Thus, leakage of argon cover gas alone is of no concern for operation of EBR-II. However, running the reactor with one or more breached elements that were releasing fission products to the cover gas would be a major problem. It was found possible to make only modest reductions in the leak rate by refurbishment of seals. Thus, a CGCS was designed, built, and installed to purify the cover gas by means of a cryogenic still working on a liquid nitrogen cycle. This system has proven to be a

highly effective means of controlling gaseous fission products in the cover gas [9].

Even though the release of high radioactivity to the cover gas was controlled by the CGCS, to maintain a safe RBCB program there is a need for effectively identifying the breached element and keeping surveillance of it thereafter. To accomplish this, three analytical models have been developed, each providing many diagnostic tools. However, the complexity of these models has made inference from their results a tedious and at times impossible task for the reactor operator. Here, the purpose of this research is to design an ES that can be used for diagnosing fuel failures during RBCB operation.

Scope of the Project

In the design of the ES for identification and surveillance of failed fuel elements, the analytical models used by the domain experts as diagnostic tools (i.e., interpreting TG and DN) must be incorporated in the KB. In addition to these analytical models, FG analysis is also developed and used as a part of the KB of the ES. The analytical models and the diagnostic tools used in the ES are the following:

1. TG analysis:

- Identifying the subassembly that contains the failed fuel element

2. DN analysis:

- Verifying the identification of the location of the breached element
- Determining the extent of the breached element

- Indicating the potential for release of fuel to the coolant (by size of the breach)
- Annunciating the possible onset of a subassembly flow-blockage event

3. FG analysis:

- Indicating the occurrence of a new breach
- Indicating the number of failed fuel elements in-core
- Indicating the type of breach (fuel-column or plenum)
- Indicating the type of breached element (mixed-oxide or metal)
- Indicating the mechanism of the breach in a mixed-oxide element (FCMI or creep-rupture)
- Facilitating diagnostics in a multi-breach mode

These analytical models and the diagnostic tools are described in Chapters 2, 3, and 4.

The TG and DN analyses have been used for many years in EBR-II; therefore, a considerable amount of expertise has already been acquired from using these methods. However, there has been very little experience in FG analysis. To gain expertise in FG analysis, data required as input in the FG analytical model were accumulated from May of 1986 to April of 1990. The FG analysis was performed and the results were studied.

The results of the five years period were then used for extracting rules that can be used as part of the KB of the ES. These rules were generated using the inductive learning techniques. The ES shell, 1st Class Fusion, a product of 1st Class Expert

System, Inc., was used to derive the rule tree. This shell requires a set of examples, with the associated conclusion, as input. Before entering the examples, the important diagnostic factors and the associated value for each factor must be declared. Each diagnostic event is formalized as an example. In each example, a value for each factor and the associated conclusion must be included.

In these examples, the TG information was obtained from the monthly status reports (called "leak reports") produced at EBR-II. The data, including the DN signals, the activities of the FG isotopes, and the CGCS purge rates (used as input for the FG analysis) were acquired from the data acquisition system (DAS) at EBR-II. The FG analysis was then performed and the results were plotted and analyzed to produce the examples which were needed to produce the rules, using the inductive learning technique. In Chapter 5, the analysis of the FG activity for the past five years is provided. In Chapter 6, the method of inductive learning and the associated rule tree development is described. The rules generated from this past experience (inductive learning) are reviewed and analyzed.

Another facility provided by 1st Class Fusion for generating the rules was then used to incorporate the heuristic rules. These are heuristic rules used by the domain experts and are not generated by inductive learning. Also, methods are set forth for learning from future experience. Specifically, an algorithm is provided which modifies the KB of the ES to accommodate for new expertise acquired. This is accomplished by introducing meta-rules. The meta-rules are used to decide whether the new event is within the domain of the expertise of the KB. In case a new event is encountered, the meta-rules would direct the ES to acquire this new expertise, thus, modifying the existing rules in the KB. In other words, the meta-rule regenerates the rules by using

inductive learning whenever a new event is encountered.

In Chapter 7, the use of meta-rules and pattern recognition techniques are explored, since, ultimately, the learning of this expert system must be automated. Finally, we conclude by outlining the overall architecture of the ES.

CHAPTER 2. TAG GAS METHOD FOR FAILED FUEL IDENTIFICATION

A method developed at the earlier stages of failed fuel diagnostics at EBR-II was the TG method. Gas tagging consists of the addition of small amounts of gas that has a unique isotopic composition to fuel pins of each assembly. When a fuel element fails during subsequent irradiation, the unique composition of TG added to the fuel elements allows identification of the subassembly. This is done by a mass spectrometric analysis of the reactor cover gas into which the gas from the failed fuel is incorporated [10]. The TG method used currently for identification of fuel failure in EBR-II is an analytical method involving barycentric coordinates as described later here. This method has evolved from other methods when their shortcomings were realized. The current TG method and its predecessors are described in this chapter.

Xenon Tag Method

The method of xenon tagging entails mixing xenon with varying ratios of different stable xenon isotopes with the usual gas filling of fuel elements, so that the tags added to the fuel elements are distinguishable. By doing so, the ratio of any two stable isotopes then becomes a unique tag identifying a fuel element. The method of xenon tagging was first invented by Henault and others [11] at Argonne National

Laboratory to be used for diagnostics in EBR-II [10].

The xenon tag is added to fuel elements in two ways. A syringe is filled with several *ml* of tag and one *ml* is injected into each of several fuel elements by means of a long needle reaching to the bottom of the helium-filled gas plenum; or, alternatively, the entire element is evacuated and then back-filled with a predetermined mixture of helium and tag [11]. In EBR-II, approximately one *ml* of a unique mixture of the stable xenon isotopes, ^{124}Xe , ^{126}Xe , ^{128}Xe , and ^{129}Xe are loaded into unirradiated elements, using one of the above methods. All of the xenon isotopes are obtained by isotopic enrichment of natural xenon, except for ^{128}Xe which is obtained by thermal neutron irradiation of iodine [10]. The volume of TG added to the fuel elements varies from 0.5 to 1.5 *ml*, and volumes of tag available in the cover gas for analysis have also varied widely from 0.006 to 0.83 *ml*. A lower limit of release of approximately 0.04 *ml* of tag into the cover gas was cited in Reference [10] as permitting identification.

Up to 1975, implementation of this method posed no complications, since expected TG release to the cover gas was not greatly dissimilar to what had been loaded, considering that the irradiation time of the xenon isotopes to that point was short. However due to (n, γ) reactions with ^{124}Xe , the ratio ($^{128}\text{Xe}/^{124}\text{Xe}$) increases as fuel burnup becomes significantly large. This was anticipated, but since the burnup was low (i.e., < 5 at.%) there was not a need for correcting for changes in the estimated amount of tags. In January of 1975, failure of the first highly burned-up element was seen, where 20% burnout of ^{124}Xe had occurred. Also, at this burnup there is a substantial production of ^{128}Xe . The combined result was a 270% increase of the ratio ($^{128}\text{Xe}/^{124}\text{Xe}$) [10]. To correct for this, empirical correlations for buildup of ^{128}Xe and burnout of ^{124}Xe were developed by So et al. [12].

The empirical correlations now used in EBR-II are [10]:

For ^{124}Xe burnout in all elements,

$$V_{124} = \frac{F_{124}V_{tag}}{0.018D + 1},$$

where

V_{124} = ml of ^{124}Xe

V_{tag} = tag volume, ml

F_{124} = fraction of TG that is ^{124}Xe

D = total fluence ($n/cm^2 \times 10^{-22}$).

For ^{128}Xe buildup in mixed-oxide elements

$$V_{128} = F_{128}V_{tag} + 2.13 \times 10^{-6}HB^2,$$

where

V_{128} = ml of ^{128}Xe

V_{tag} = tag volume, ml

F_{128} = fraction of TG that is ^{128}Xe

H = weight of heavy metal, g

B = burnup, at.%.

Correlations have also been developed for exposure changes in the ^{126}Xe and ^{129}Xe content of xenon tags, although, their changes are of secondary importance, compared to those of ^{124}Xe and ^{128}Xe [13].

Ratio of Fission Gas to Tag Gas for Diagnosis

A related difficulty arose at higher fuel burnup, as fission-produced xenon became more prominent and caused tag compositions that were initially different to become similar. This led to ranking of suspects on the basis of their relative fractional releases of FG and xenon tag [14].

Assuming perfectly mixed FG and TG in plenums of all types of elements, the following relations were used to search for the failed fuel element using the relative fractional releases of FG and xenon tag [10]:

$$\frac{V_{fp}}{V_{tp}} = \frac{V_{fc}}{V_{tc}},$$

where,

V_{fp} = volume of FG in plenum,

V_{tp} = volume of TG in plenum,

V_{fc} = volume of FG in cover gas, and,

V_{tc} = volume of TG in cover gas.

The value of V_{fp} is obtained from gas release correlations [15] for elements irradiated in EBR-II, V_{tp} is known from tag records, and V_{fc} and V_{tc} are directly measured by radiometric analysis and mass spectrometry of cover-gas samples. This method, of course, added an extra degree of confidence for diagnosis.

Ratio of ^{131}Xe to ^{134}Xe Used for Diagnosis

To identify the type of failed fuel element, the ratio of stable ^{131}Xe to stable ^{134}Xe can be measured. This will give an indication of whether a fission product release was from a uranium-metal driver-fuel element or an experimental element containing plutonium [16]. Lambert and others [10], demonstrated that even though the $^{131}\text{Xe}/^{134}\text{Xe}$ ratio changes with burnup, the tags released from different types of intact elements after irradiation in the EBR-II are distinguishable.

The data analyzed for this method were obtained by studying failed fuel elements containing a wide range of fissioning nuclides, namely, from pure ^{235}U fissioning in the driver-fuel elements to almost pure ^{239}Pu fissioning in a few mixed-oxide elements containing 25wt% PuO_2 and in natural UO_2 [10].

By plotting the ratio of ^{131}Xe to ^{134}Xe versus average fuel burnup in *at.%*, Lambert [10] showed that the data fall into three distinct areas: a central band that includes measured ratios from almost all fully enriched elements containing 20 to 25wt% plutonium, an area below this band that contains ratios found only in uranium-metal driver-fuel elements, and an area above the band that contains ratios from more nearly pure plutonium-fissioning elements. The two lines confining the central band are found to be parallel and to have a negative slope, in other words, the ratios decrease with increasing burnup, as is expected.

This method is found to be useful in determining whether or not a release has been from a uranium source; thus, it can be used to eliminate many suspect sub-assemblies. For example, ratios of the metal element type (i.e., driver-fuel element) fall in the lower area. When this method was used for the first time in March of

1975 at EBR-II, there was a release from an element in an untagged subassembly. The use of this method allowed eliminations of many suspects; thus, identifying the subassembly where the failed element was located [10].

Vector Technique Used for Identification of Simultaneous Tags

Another problem arose when the occurrence frequency of the breaches increased, namely simultaneous tag releases were seen. This happens when a failure occurs while more than a negligible amount of TG is present in the coolant from one or more previous leakers. During 1975 the occurrence of a simultaneous tag release was detected for the first time. Although the amount of the tag from the earlier leaker was small, the identification of the new breached element was affected [10]. This led to the development of the code MIXTAG by So and Stauffer [17]. This code takes into account both the change of the tag during exposure by use of the empirical formulae described previously and the secondary effects of natural xenon contamination of the argon cover gas and FG from "tramp" uranium [10].

In EBR-II, it is found that there is an irreducible trace of fissionable material in the core external to the fuel cladding. This material produces fission products at a rate equivalent to that which would be expected from the exposure of around $2\frac{1}{2}mg$ of ^{235}U . The term "tramp" uranium stems from the assumption that this material is actually contamination on the surface of the fuel cladding, and the term "tramp" activity, analogously, refers to the activity due to the fissioning of the "tramp" uranium and its by-products [18]. In the experiments conducted in EBR-II, during a six to seven years period, the level of tramp activity has remained remarkably constant. This implies that the tramp uranium can not be incidental contamination; since, if

this were the case then the tramp level might reasonably be expected to fluctuate, depending on the cleanliness with which the most recent batch of fuel was fabricated [18]. However, no other explanations are provided in the literature on what might be the source or what mechanism causes the constant release of tramp uranium.

The vector technique, employed in MIXTAG, is described in Reference [19]. The material presented in the remainder of this section is mostly obtained from Gross and Passerello [19], unless cited otherwise. Gross and Passerello use a two-dimensional tag ratio plane for the sake of simplicity of demonstration. In this plane, the x - and y -coordinates are different ratios of tag isotopes, and their range covers all mole ratios of tag isotopes added to the fuel elements. By doing so, each subassembly is represented by a node on this plane and is identified by the mole ratio of the tag added. The tag nodes used for this example are plotted on the plane and denoted by N_1, N_2, N_3 , etc., in Figure 2.1. After the first breach occurs, the mole ratio of the detected tag defines a point (in our example called B_1) in the figure. The breached subassembly is identified by calculating the shortest distance between the point B_1 and the subassembly tag nodes. The position of the nodes in Figure 2.1 are chosen arbitrarily for the purpose of this demonstration.

In this illustration, the shortest distance from B_1 identifies node N_4 . Suppose now a second breach occurs while the tag ratio of the first breach is still being detected. Call the point representing the mole ratio of the second breach B_2 . The procedure for finding the node representing the subassembly which contains the secondly breached element is now as follows:

1. Form $N - 1$ vectors from node N_4 (the first leaker) to each of the remaining

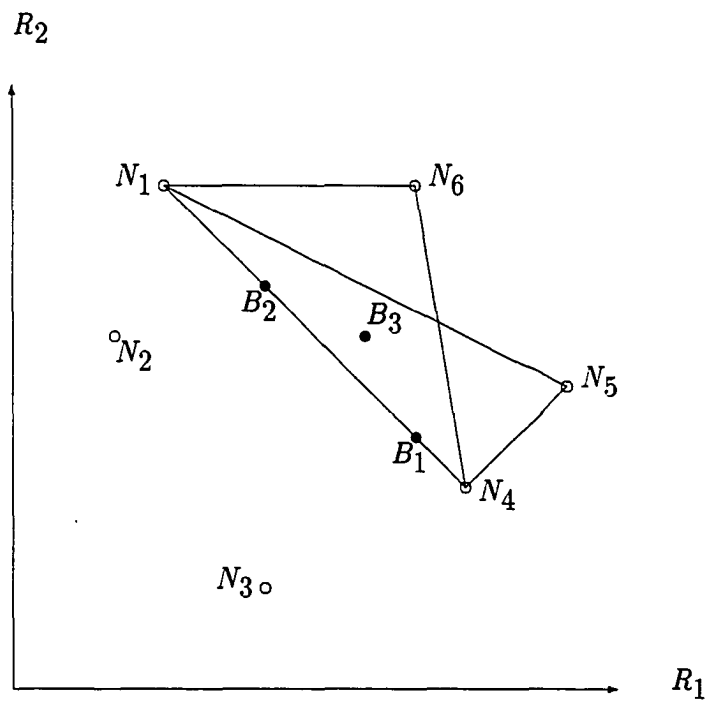


Figure 2.1: Planar display of six tag nodes and three simultaneous breaches.

suspect nodes, where N is the total number of nodes in the system (let us call these the suspect vectors).

2. Draw a vector from node N_4 to B_2 .
3. Find all the perpendicular distances between B_2 and suspect vectors.
4. The shortest perpendicular distance corresponds to the tag node most likely representing the second leaker.

Following this procedure, N_1 is found to be the second leaker in this example.

This procedure is developed based on the logical, and also experimentally discovered principle that the locus of points representing a mixture of two tags is the tie-line connecting the two tag nodes (i.e., in our example N_4 and N_1). In other words, the distance found in the third step is very close to zero as can be seen in Figure 2.1. In this figure, six tag nodes are assumed. The tie-line is displayed by a solid line connecting the nodes N_1 and N_4 . In the case where a third immediate breach occurs, namely, when the tag released by the previous two breaches are still detectable, the procedure for identifying the suspects becomes less precise. The point B_3 in Figure 2.1 depicts the position of the third breach. Since, the point B_3 does not lie on or near the (N_1, N_4) tie-line, a new element has breached. To find the third node corresponding to the assembly which contains the third breach element, $N - 2$ triangles are drawn using the tie-line as the base and the remaining nodes as vertices (i.e., N_2, N_3, N_5 , and N_6 in Figure 2.1). The suspects are then the nodes that are the vertices of the triangles containing B_3 . This demonstrates the limitation of the vector method: B_3 is in two triangles. Thus, there are two suspects, N_5 and

N_6 . No further action can be taken to eliminate one of these suspects by only using this analysis in two dimensions.

The use of a three-dimensional vector technique would diminish the probability of having more than one suspect when three simultaneous breaches occur. In three dimensions, four tag isotopes define three tag ratios which are used as the coordinates. The three-dimensional space now can be used for the tag nodes so that the triangles formed are not coplanar. For instance, in our example, the position of nodes N_5 and N_6 can be chosen so that the two triangles whose vertices are N_5 and N_6 are not coplanar. The diagnosis can then be easily performed by calculating the perpendicular distance between B_3 and the triangles whose vertices are the suspects. The triangle corresponding to the shortest distance contains the third breach as one of its vertices.

Also, the three-dimensional vector technique allows for identifying the fourth breach analogous to finding the third breach in two-dimensional analysis. In this case, $N - 3$ tetrahedrons are formed by using the first three tag nodes as the common base and each of the remaining tag nodes in the system as the fourth vertex.

Again, by use of vector techniques, diagnosis is performed by determining which suspect tetrahedrons enclose the fourth measured node, B_4 . And similar to the two-dimensional analysis, where for the identification of the third breach nondeterminism can arise, for three-dimensional analysis identifying the fourth breach can become imprecise. Similarly, a four-dimensional vector technique based on five tagging isotopes permits precise identification of up to five simultaneous breaches. It must also be noted that the background tag detected can be accounted for by representing their ratios as nodes. MIXTAG had been successfully used in EBR-II to identify new

leakers in the presence of up to two background tags in a core of 50 to 55 tagged assemblies [17]. However, due to two limitations this method can not be used in larger cores, such as light water reactors or large fast reactors, or in reactors operating in the RBCB mode. The first limitation is that, in order to identify the new leaker, the previous leakers must have already been identified; and in EBR-II the tag sample can be analyzed no more frequently than every two hours [20]. In the case when two breaches have occurred within a two-hour period, performing this analysis is misleading. The second limitation is that the number of operations needed to perform the vector technique becomes very large.

To eliminate the first limitation, a combination of suspect nodes can be assumed (e.g. node N_1 is the first leaker and the remaining nodes are the other leakers or no leakers); by performing the vector analysis the suspect combinations are eliminated and the leakers are found. This procedure was followed in the Fast Flux Test Facility by Omberg and Schenter [21]. Even though this procedure alleviates the first limitation, it increases the number of operations factorially, and thus enhances the second limitation.

For identifying a leaker among the 50 tag nodes in EBR-II, 10 to 15 seconds of computer time is required on the IBM-370/195, depending on whether the leaker is the first, second, third, or the fourth leaker of a leaker set. However, if four simultaneous breaches occur and none of them were previously identified, 2.3×10^5 tetrahedron calculations are required. This translates to requirement of > 10 hours of central processing unit time per run on an IBM-370/195. In general, the number of operations increases with the binomial coefficient $N!/(N - N_L)!N_L!$ where N is the number of tags and N_L is the number of leakers.

Barycentric-Coordinate Technique

The barycentric-coordinate technique was developed to overcome the limitations previously described. This technique employs an efficient algebraic procedure that gives essentially the same result as obtained by the vector technique, but in a fraction of the computing time. This technique, developed by Gross and Passerello, is currently in use in EBR-II. The reference for the material presented in this section is Gross and Passerello [19]; to be efficient, the citations for this reference will not be repeated in the remainder of this section. If the reader desires a more elaborate description of the barycentric-coordinate technique, he/she can refer to Gross and Passerello. In short,

“this technique utilizes procedures from finite element mathematics to express the tag-node coordinate in the form of linear weight functions using a system of what are known in topology as barycentric coordinates”[19].

Description of the Technique in Two Dimensions

For the sake of simplifying this demonstration, a two-dimensional tag system with three tag nodes is used. The node triangle shown in Figure 2.2, will be used to define a barycentric-coordinate system. Three weight functions (c_1, c_2 , and c_3) must be defined to describe the coordinates of any point B that falls on the Cartesian plane. Let us assume the point B is at (x, y) in the Cartesian coordinates. We can relate this position linearly to the new coordinates by the following equations:

$$x = c_1 x_1 + c_2 x_2 + c_3 x_3$$

$$y = c_1y_1 + c_2y_2 + c_3y_3$$

By imposing the condition,

$$c_1 + c_2 + c_3 = 1,$$

the matrix

$$\begin{pmatrix} x_1 & x_2 & x_3 \\ y_1 & y_2 & y_3 \\ 1 & 1 & 1 \end{pmatrix} C_3 = \begin{pmatrix} x \\ y \\ z \end{pmatrix},$$

where

$$C_3 = \begin{pmatrix} c_1 \\ c_2 \\ c_3 \end{pmatrix},$$

can be formed.

The normalization of the weights is desirable, since now the value of c_i is unity and the others zero at the point (x_i, y_i) . The matrix equation developed can now be solved to obtain the values of the vector C_3 . In Table 2.1, the physical and geometric interpretations of all of the possible values that the elements of the vector C_3 can have are given.

The diagnosis using this technique, where there are more than three tag nodes and multiple simultaneous breaches, can easily be accomplished. Assuming there are N nodes for each leaker then there will be $N!/(N-3)!3!$ triangles to be analyzed. The vector C_3 can then be calculated for all of these triangles.

By inspection, the C_3 vectors which have an element(s) with a negative value can be eliminated, since analysis of these would result in nondeterminism; see Table

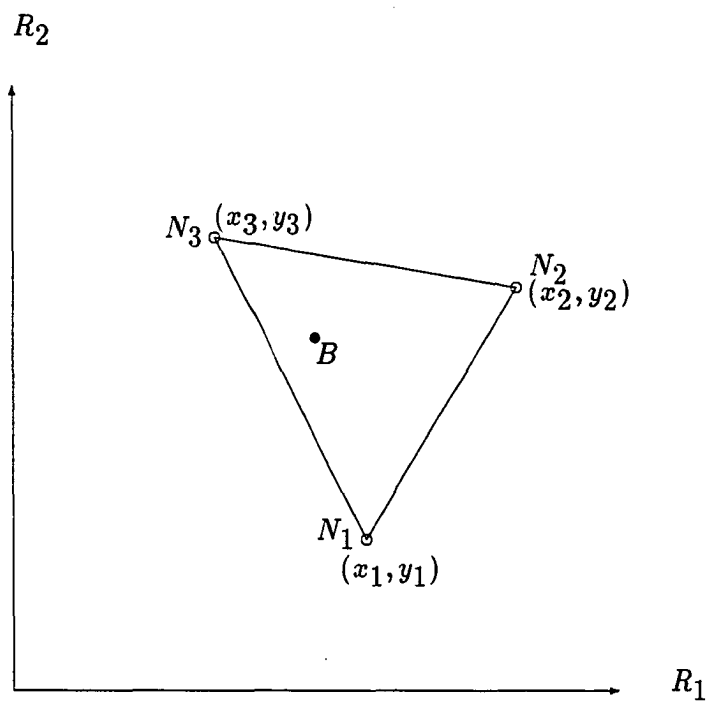


Figure 2.2: Transformation from Cartesian coordinates to barycentric-coordinates system.

Table 2.1: Geometric and physical properties of C_3 solution vector

Outcome of C_3 Determination	Physical Interpretation	Geometric Interpretation
$c_i = 1$ $c_j = 0$ $c_k = 0$	Assembly i leaking	Measured node coincides with tag node i
$c_i = 0$ and $0 < c_j < 1$ and $0 < c_k < 1$	Assemblies j and k leaking simultaneously	Measured node falls on connecting nodes j and k
$0 < c_i < 1$ and $0 < c_j < 1$ and $0 < c_k < 1$	Assemblies i , j , and k leaking simultaneously	Measured node confined to triangle whose sides connect nodes i , j , and k
$c_i < 0$ or $c_j < 0$ or $c_k < 0$	Assemblies i , j , and/or k could be leaking, but at least one other assembly must be leaking elsewhere	Measured node lies outside triangle whose side nodes i , j , and k

2.1. After eliminating all C_3 vectors with at least one negative element for each breach node, a list of suspect triangles can be formed. The common suspect triangle or triangles to all lists contain the nodes corresponding to subassemblies where the breach has occurred. Finally, by considering where the detected breach node lies, the leaking subassembly or subassemblies are found. In other word, the analysis reduces to analysis of only one triangle and the properties of Table 2.1 can be used.

The analytical technique described above, even though theoretically always valid, would not be successful if some practical precautions were not taken. Error induced by the analytical technique is due to the experimental uncertainties associated with, (a) the resolution of the mass spectrometer detection equipment used to measure the isotopic ratios, (b) the blending of the gases when the tags are first created, and (c) depending on the gases used, uncertainties in the noble gas isotopic compositions due to neutronics effects. Therefore, the multiple failure analysis technique, telling

us whether the measured node falls on the line or not, is not sufficient; it must also be capable of determining how far from the line the point lies. This would also be crucial when one must decide whether or not the point lies in a triangle (refer to Table 2.1).

This shortcoming can be remedied by enforcing a cylindrical and a spherical uncertainty space respectively around the lines that connect two tag nodes and the nodes themselves. The dimensions of these cylinders and spheres are determined by the uncertainties of the measuring equipment. Also, realizing that the components of the matrix C_3 have a direct geometric interpretation, a visual understanding of the position of the breach nodes relative to the tag nodes barycentric coordinates can be achieved: for a triangle whose vertices are tag nodes i , j , and k , the value of $|c_i|$ is equal to $(\Delta Bjk/\Delta ijk)$ and when B lies in the triangle c_i is positive and when it lies outside of ijk it is negative.

The Barycentric Technique in N Dimensions

When new breach tags are detected very soon after the collection of others, elimination of all possible modes of failure (i.e., triangles in a two-dimensional analysis) may become impossible. This is because the breach nodes on a two-dimensional plane would lie near each other, thus causing an increase in the number of common mode failures. When this occurs in practice, the breach tag detection may have to be repeated until a unique identification is obtained. "Thus, for a reactor with a two-dimensional system in which many nodes lie on a common plane, an automatic on-line mass spectrometer with a cycling time shorter than the effective mean cleanup time for noble gases in the primary system would be essential"[19].

However, with less effort, use of a higher-dimensional tag system would alleviate this problem, since the probabilities of coplanarity of triangles become much lower. Therefore, identification of the leakers can be accomplished with only one sample, even though detection of consecutive tag samples would add confidence to the results of the initial analysis or detect shifts that might indicate the occurrence of new releases.

The barycentric technique is easily extended from a two-dimensional plane to an N -dimensional hyperspace. The resulting matrix equation is in the form:

$$\begin{pmatrix} a_{1,1} & a_{1,2} & \cdots & a_{1,N+1} \\ a_{2,1} & a_{2,2} & \cdots & a_{2,N+1} \\ \vdots & \vdots & & \vdots \\ a_{N,1} & a_{N,2} & \cdots & a_{N,N+1} \\ 1 & 1 & \cdots & 1 \end{pmatrix} C_{N+1} = \begin{pmatrix} a_1 \\ a_2 \\ \vdots \\ a_N \\ 1 \end{pmatrix},$$

where

$$C_{N+1} = \begin{pmatrix} c_1 \\ c_2 \\ \vdots \\ c_{N+1} \end{pmatrix}.$$

The element $a_{i,j}$ is the location of the tag node j , in i^{th} dimension.

Gross outlines the diagnosis as follows. In general, if J of the $N + 1$ assemblies are leaking, the J corresponding components of C_{N+1} will be between 0 and 1, and the remaining components will be zero. Moreover, for components that are nonzeros, c_i uniquely defines the fraction of TG that has escaped from assembly i .

Finally, if the measured node falls outside the hyperpolyhedron whose vertices are the $N + 1$ tag nodes, one or more of the c 's will be negative. In this case it means that at least one assembly other than, or possibly in addition to, the $N + 1$ suspects must be releasing TG somewhere else in the system. Gross concludes by emphasizing the importance of accuracy in specification of assembly tag compositions and treatment of background-tag isotopes.

Evaluation of TG Analysis

Currently, the barycentric coordinate technique in three dimensions is used at EBR-II [20]. This analytical method has proven to be successful; however, there are still some practical disadvantages [20]:

1. TG mass spectrometry is not automated.
2. The maximum frequency of TG analysis is once every two hours.
3. When a breach occurs, sometimes the TG is not released due to the blockage caused by fuel-sodium reaction product at the site of the defect.
4. The recently incorporated CGCS, reduces the amount of FG in the cover gas but also it reduces the amount of TG; thus, it makes the mass spectrometry more difficult.
5. The cost of having a unique tag for each subassembly is very high specially for reactors with large cores.

6. TG might be released from the breached element gradually during a long period of time.

Added to these practical disadvantages, when multiple simultaneous breaches occur (and none of them has been identified previously), even with all efforts made to improve the time efficiency of the analytical method, the computer time needed for diagnosis is too long.

CHAPTER 3. USE OF DELAYED NEUTRON SIGNALS FOR SELECTION AND SURVEILLANCE OF FAILED FUEL ELEMENTS IN FAST REACTORS

Until 1978, the occurrences of fuel failure in EBR-II were well separated, due to the low burnup of fuel elements. Also, a great deal of gas release, i.e., tag and FG, was detected when a clad breach occurred. This facilitated identification of breached elements by solely using the xenon-tag analysis. However, problems arose when higher burnup of fuel elements was reached, as was mentioned in the previous chapter. After 1978, when clad breach of highly burned-up advanced fuel elements such as carbide or nitride elements occurred, very little FG and TG release was seen but significant DN signals were produced [22]. Also, for the RBCB operation, not only the location but also the extent of the breach must be determined. This led to the development of a new technique, namely, DN signal analysis.

The DN signal analysis technique, as developed, complements the TG analysis by providing tools: verifying the location of the breach by inspecting the transit time (the traveling time of DN precursors from failed fuel to the DN detectors) so that an estimated distance to the location of the breached element can be identified, and determining the extent of the breach by providing an estimate of the actual area of fuel beneath the cladding defect. In this chapter, the DN detection system used for

measuring the activity due to the emission of DN is described and the development of the analytical model used for determining the surface area of the defected site is outlined. The analytical model is comprised of the equation used for calculating the activity due to the emission of DN and the statistical model. The statistical model facilitates the diagnostic tools mentioned above.

Delayed Neutron Detection System

A design schematic of the triple-station DN characterization system, or 3-DND system, obtained from Reference [23], is depicted in Figure 3.1. The 3-DND will ultimately be used in the place of the currently used apparatus called fuel-element rupture detector (FERD) system for DN signal detection in EBR-II. The 3-DND system consists of three DNDs, a general isotope release analysis for failed element (GIRAFFE) micro-processor, and the output displays of GIRAFFE. The FERD system is also comprised of GIRAFFE and the output displays of GIRAFFE; however, in the FERD system only one DND is used. The new design for the DN detection system was needed for the reasons to be explained. However, the development of the analytical model and its deficiencies must be explained first.

A sodium sample is taken from the intermediate heat exchanger outlet to the 3-DND detectors located external to the reactor vessel. The count rate from DN emission by the precursors in a unit volume of sodium coolant seen by the detectors is measured. The sodium coolant sample is then returned to the primary loop. Signals from the DN detectors are analyzed by GIRAFFE. The analytical method used for developing GIRAFFE is described in the next section. This analytical method was developed and validated using data obtained from RBCB tests in EBR-II [22].

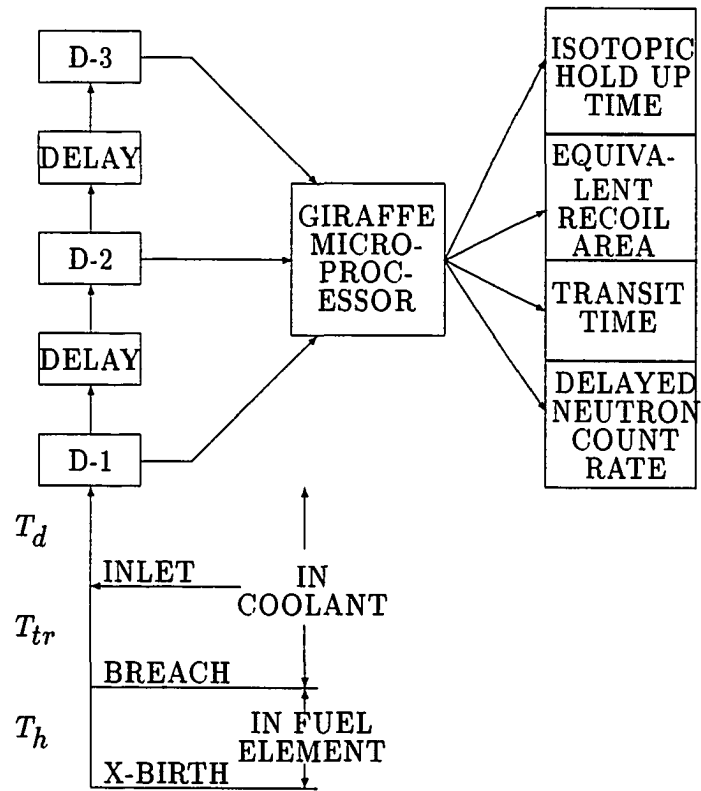


Figure 3.1: DND configuration for on-line characterization of DN signals

As is shown in Figure 3.1, the DN precursors reach the first DND after $T_h + T_{tr} + t_f$ time, where T_h is the isotopic holdup time in the fuel pin after birth, T_{tr} is the transit time in the primary coolant, and t_f is the time spent in the 3-DND or the FERD loop before detection. An experiment, using fission product source (FPS) capsules, was performed and the results were reported by Gross and Polley [24]. The objectives were to evaluate the response characteristics of DNDs at EBR-II under a broad range of transient power and transient temperature conditions, and to verify that FPS capsules are “pure recoil sources”; that is, the fission product release rate is directly proportional to the product of the fission rate and surface area under both steady-state and transient temperature conditions. The purpose of the second objective was to use FPS capsules, verified to be “pure recoil” sources, to calculate the values of T_h and T_{tr} . An accurate determination of these parameters is crucial in setting up a fission product monitoring system for EBR-II and other reactors. This is described in detail, in Section 4.2.3.

After performing the experiments, Gross and Polley concluded that (a) DNDs in EBR-II are very sensitive and have excellent counting statistics; (b) they are highly linear with respect to power variations and are unaffected by variations in DND temperature; and (c) they can accurately follow transient release rate variations over a broad frequency range.

Analytical Method Used in GIRAFFE

The DN precursors are released from the fuel elements through many mechanisms. In the development of the earlier models used for DN analysis, it was assumed that the recoil emission is the only way the DN precursors and their parent isotopes

escape from the breached fuel pins. Because of this assumption, the original models were not successful when used for diagnosing the failure of certain types of fuel elements. For example, it was found that DN signals produced by oxide fuel elements were often several times larger than the values calculated by the methods developed based on the assumption that the release of DN emitters is only by recoil from the geometrical area of the fuel exposed to the coolant [22].

The new model, which is used to develop GIRAFFE, treats nonrecoil fission sources as well as recoil sources. Also, other considerations are employed so that this new model can be applied to general cases. Namely, the following factors were taken into account: (a) the intermediate decay of the precursors of DN emitters in the fuel and the coolant; (b) the enhancement of the total DN signal from nonrecoil effects; (c) the isotopic holdup in the fuel and the effect of this holdup on the relative proportions of short- versus long-lived isotopes; and (d) the compound decay of tramp DN emitters within the FERD loop. The material for this description is obtained from Gross and Strain [22].

Derivation of the Equation Used for Calculating DN Activity

The first step for developing the analytical equation which is used to calculate the total activity of DN emitters at the FERD detectors is to form differential equations for calculating the number of parent and daughter isotopes in the fuel matrix. These differential equations are then modified so that the release time for DN precursors and their parent isotopes from the fuel matrix can be also taken into account. The release from the fuel matrix is assumed to be governed by an Arrhenius rate equation as a function of time; thus, the parameter λ_e , which is defined as the effective escape-rate

coefficient is introduced. This parameter is the reciprocal of the previously defined T_h (i.e., $\lambda_e = 1/T_h$).

The modified differential equations are then solved for equilibrium condition (i.e., at times longer than $1/(\lambda_e + \lambda_{decay})$). Without any doubt, it can be assumed that parent and daughter isotopes have reached equilibrium before they are released from the fuel matrix, since the time that fuel elements spend in the reactor before clad breach occurs is always orders of magnitude longer than the time governing the equilibrium condition. Therefore, by assuming steady state, or mathematically by setting dN/dt equal to zero, where dN is the change in the number of isotopes in the differential time dt , the time-independent equations which give the number of parent and daughter isotopes from birth to when they are released from the fuel matrix, are found to be,

$$N_{FP}^i = \frac{S_P^i}{\lambda_P^i + \lambda_e}$$

and

$$N_{DF}^i = \frac{\left(\frac{\lambda_P^i S_P^i}{\lambda_P^i + \lambda_e} + S_D^i \right)}{(\lambda_D^i + \lambda_e)},$$

where

N_{FP}^i = number of atoms of parent isotope i in fuel at steady state

N_{DF}^i = number of atoms of daughter isotope i in fuel at steady state

S_P^i, S_D^i = fission production rates for isotopes of species i , *atoms/s*

λ_P^i, λ_D^i = decay constants for isotopes of species i , s^{-1} .

The second step entails calculating the concentration of parent and daughter isotopes initially at the defect site in the sodium coolant. To find the number of

isotopes in the sodium coolant, it is convenient to work on a unit volume basis.

This assumption is made that even though the isotopes initially injected into the coolant do not remain together for the entire trip, the principal effects in EBR-II are thought to be large-eddy mixing in the upper plenum and flow stream splitting and recombining. However, one must also realize that while these effects can create significant dispersion in the measured signals, mean values obtained by averaging large numbers of data should follow the behavior governed by the equations developed based on the assumptions made earlier.

If $N_{P,Na}^i$ and $N_{D,Na}^i$ are, respectively, defined as the initial concentration of parent and daughter isotopes at the defect site in $atom/cm^3$ of sodium that are released into the differential volume of coolant flowing past the defect site, then the equations for the parent and daughter concentrations are:

$$N_{P,Na}^i = \frac{\lambda_e}{(\lambda_D^i + \lambda_e)} \frac{S_P^i}{F},$$

and

$$N_{D,Na}^i = \frac{\lambda_e N_{D,D}^i}{F}$$

where, F = primary coolant flow rate in cm^3/s .

In the third step, the equations used for calculating the activity of the daughter isotope i at the FERD detector are derived. The number of atoms of parent isotope i released into the coolant at the time t can be calculated by,

$$N_{P,Na}^i(t) = \frac{\lambda_e}{(\lambda_P^i + \lambda_e)} \frac{S_P^i}{F} \exp(-\lambda_P^i t),$$

the governing differential equation used for population of the daughter isotope i is,

$$\frac{dN_{D,Na}^i}{dt} = N_{P,Na}^i \lambda_P^i - \lambda_D^i N_{D,Na}^i,$$

and the initial condition (i.e., at $t = 0$) for the number of daughter isotopes is,

$$N_{D,Na}^i(0) = \frac{\lambda_e}{(\lambda_D^i + \lambda_e)} \frac{\left(\frac{\lambda_P^i}{\lambda_P^i + \lambda_e} S_P^i + S_D^i \right)}{F}.$$

At this point it is appropriate to separate the total flow-delay time t into two components by making the substitution, $t = T_{tr} + t_f$, for the reasons which will become apparent later on.

The governing differential equation for the daughter isotope can be solved numerically by applying the initial condition and using the time dependent equation for the parent isotope. The resulting equations give the number of atoms of isotope i as a function of T_{tr} , t_f , and λ_e . To find the activity from the concentration of the daughter isotope, the following relation is used,

$$A(T_{tr}, t_f, \lambda_e)^i = \lambda_D^i N_{D,Na}^i(T_{tr}, t_f, \lambda_e).$$

Thus, the equation for finding the activity of the daughter isotope i is determined to be

$$A(T_{tr}, t_f)^i = \frac{\lambda_D^i \lambda_e}{F} \times \left(\lambda_P^i S_P^i \frac{\exp(-\lambda_P^i(T_{tr} + t_f)) + \exp(-\lambda_D^i(T_{tr} + t_f))}{(\lambda_D^i - \lambda_P^i)(\lambda_P^i + \lambda_e)} \right) + \frac{\left(\frac{\lambda_P^i}{\lambda_P^i + \lambda_e} S_P^i + S_D^i \right)}{\lambda_D^i + \lambda_e} \times \left(\exp(-\lambda_D^i(T_{tr} + t_f)) \right). \quad (3.1)$$

The final step of this effort is then to derive the equation for finding the total DN activity at the detector in cps/cm^3 of sodium. This is accomplished by using the relation,

$$A(T_{tr}, t_f, \lambda_e) = \sum_{i=1}^9 A(T_{tr}, t_f, \lambda_e)^i P n^i,$$

where Pn^i is the probability of neutron emission for isotope i .

Background Count Considerations

The activity of the DN emitters calculated above must be corrected for DN emitters produced by the fissioning of tramp uranium. The equation for calculating the tramp emitted DN signal as a function of flow rate of sodium coolant within the FERD loop is derived making the following assumptions.

1. The tramp uranium acts like a recoil source, ejecting both parent and daughter isotopes with zero holdup.
2. The location of the tramp source is in the reactor core.
3. Decay equations for the tramp produced parent and daughter DN emitters behave in the same manner as those released from the fuel defect.

The procedure for deriving the equation for the activity of the tramp produced DN emitters is then analogous to the one explained in the previous section, except that, due to the first assumption made, there is no need to include an effective escape-rate coefficient λ_e .

An experiment was performed and results were reported in Gross and Strain [22] to validate the method used for calculating activity due to the tramp produced DN emitters. Decay equations were applied for the DN emitters and their parents traveling from the core to the FERD inlet using a transit time of 15.0s and zero holdup time. The activities of the tramp DN emitters were then calculated for various FERD flow rates. To check the calculated values, the DN activity was measured while knowing that there were no breached elements present in the core (to be certain that

there are no nonrecoil sources present in-core). After superimposing the measured and calculated values on a plot of tramp background signal versus FERD flow, it was found that the agreement between the experimentally observed and predicted tramp signals was very good, which served to justify the earlier assumptions.

Statistical Method Used for Determining Transit and Holdup Time

It was stated in Section 3.2.1 that the activity of the DN emitters at the FERD detectors is dependent on three variables: T_{tr} the transit time from the core to the FERD-loop inlet, T_h (or λ_e) the parameter used to account for the time the DN emitters spend in the fuel, and t_f the flow delay time within the FERD-loop, which is directly dependent on the controlled parameter, FERD-loop flow rate. To use the analytical equation developed, one must determine λ_e and T_{tr} , since the parameter t_f is a controlled parameter and its value is decided by the FERD-loop flow rate setting. An optimization algorithm was developed that minimizes a nonlinear error function to determine these parameters. It is of the form:

$$E(T_{tr}, \lambda_e) = \sum_{k=1}^J \left\{ W_k(T_{tr}, \lambda_e) - \{ A_{mk} - A_{pk}(T_{tr}, \lambda_e) \} \right\}^2,$$

where

k = the number of flow steps,

A_{mk} = measured DN activity, corrected for the tramp background,

A_{pk} = predicated activity,

W_k = weight function assigned to A_{pk} ,

J = total number of FERD flow steps.

To calculate T_{tr} (when there is no breached element present in EBR-II), a known purely recoil fission-product source is used to obtain the measured value of the DN activity (i.e., A_{mk}) at different FERD loop flow rates. The values of A_{pk} are calculated by using the analytical equation. At this point the optimization algorithm is used to calculate T_{tr} , since for a purely recoil source $\lambda_e = \infty$. The values found for T_{tr} are then used to determine the value of λ_e in experiments where the source of the DN signal is not known. An accurate determination of T_{tr} is crucial, since tests have shown that its value depends on the relative core location of the defective element.

Determination of the Surface Area of the Defect Site

A statistical model is developed for determining the actual surface area of the defect in a breached fuel element. Also with this model, other useful information relating to the overall efficiency of the DN detection system and the background due to gamma decay can also be obtained. Figure 3.2 is presented for illustrating this statistical model. In this figure, the values for A_{mk} and A_{pk} at different FERD-loop flow rates, obtained from techniques described in the previous section, are plotted on a measured versus predicted activity plot. Then a best-fit regression line is drawn. Characteristics of this line, and the success of the regression method used in fitting the data points, are the diagnostic tools made available to accomplish the tasks mentioned above.

The value of the point γ (i.e., the point where the best-fit line intercepts the Y-axis) is an important piece of information. The numerical value of this point has a pertinent physical meaning, which is as a measure of the photoneutron component

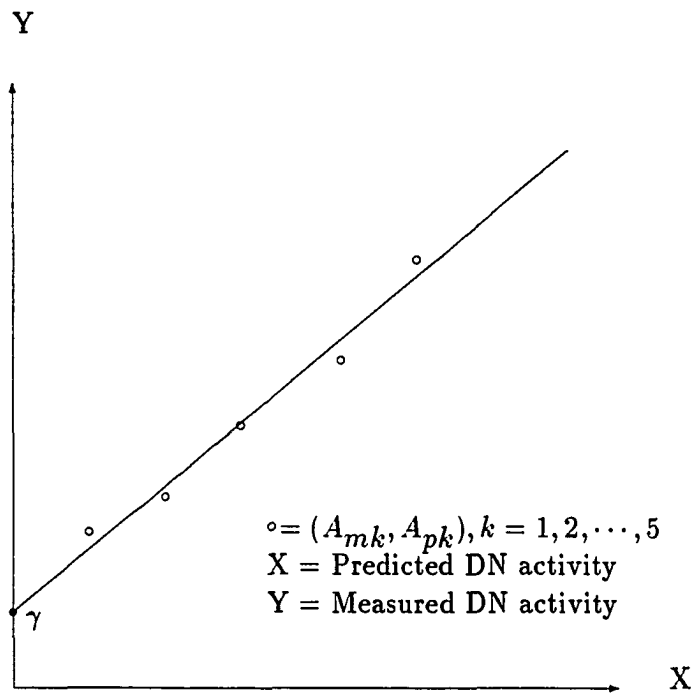


Figure 3.2: Plot of five pairs of measured and predicted DN activities and the best-fit line.

due to the gamma activity in the coolant, primarily from the decay of ^{24}Na . Prior to this realization, the gamma background signal had to be directly measured. Now, by merely extrapolating the best-fit line, the value of the gamma background signal can easily be obtained.

As is demonstrated in Figure 3.2, there are some vertical deviations of data plotted from the best-fit line. Of course, in the case where the activity measurement equipment and the analytical model for predicting the activity are perfect, it is expected that the plotted data will fall exactly on the best-fit line; in other words, the values of vertical deviations (called the residuals in *counts/s*) are zero. However, in reality, this is not the case. Nevertheless, the calculated residuals can be used to learn more about the deficiency of both the analytical model and the radiation detection equipment. For example, by studying the residuals, over- or under-predicting at low FERD-loop flow rates can be determined, thus, pinpointing the local deficiency of the analytical model. On the other hand, a spurious drift in the counting system characteristics or a slightly changing source strength (i.e., FPS) can be spotted; thus, anomalies in the detection systems can be found.

The final and most useful characteristic of the best-fit line is the slope, since it is used for calculating the surface area of the defect. This dimensionless parameter, which we denote as C , can theoretically be written as:

$$C = \frac{V_{Na}\alpha\epsilon\rho V}{F},$$

where

V_{Na} = volume of sodium in cm^3 that is seen by the DN detectors

α = fission rate in the source, in $\frac{\text{fiss}}{\text{s}\times\text{g}}$ of fissionable material

ϵ = efficiency of the detector arrangement (dimensionless)

ρ = density of the fuel in g/cm^3

V = volume of fuel from which recoil fission products are emitted in cm^3

F = flow rate of primary sodium in cm^3/s .

By use of the regression method, a relatively accurate measurement of C can be obtained. Of course, the accuracy depends on the number of data points available, but Gross and Strain claim that ($\sigma_C/C < 6\%$) can generally be achieved. This equation can be manipulated so that the volume of fuel from which recoil fission products are emitted can be computed. For this, it is necessary that the other parameters be known with a relatively high accuracy. However, due to the geometric complexity of the detection system, it is very difficult to calculate the efficiency of the detector arrangement in the FERD system. To alleviate this problem, the C computed from a test where FPS is the only source of DN emitters in the core is used to compare with the C computed during RBCB operation.

Let us first develop the method set forth and then justify the use of it. By selecting the flow rate of coolant in the FERD loop and keeping the geometry of the detection system the same in the FPS test and during RBCB operation, it is apparent that in comparing the values of C_{FPS} and F_{RBCB} the parameters V_{Na} , ϵ , and F can be dropped. Also, by altering the scaling of the x-axis in Figure 3.2, the value of C_{FPS} can be set equal to one. This is done, by adjusting the values of A_{pk} which in turn is adjusted by altering the values of S_D and S_P (i.e., as previously defined, the fission production rates of parent and daughter isotopes). These production rates are proportional to the fission rate. The physical interpretation of the proportionality constant is the probability of birth of parent and daughter isotopes when fission occurs (i.e., derived from nuclear decay data). In short, in order to set the value of C_{FPS}

to one, the proportionality constant is adjusted. The values of the proportionality constant, which resulted in $C_{FPS} = 1$, are then used for calculating S_D and S_P when C_{RBCB} is being determined. Also, it must be noted that this proportionality constant must be calculated for each fuel type, since its value depends on the fuel material.

Therefore, the following relation stands,

$$C_{RBCB} = \frac{\alpha_{RBCB} \times \rho_{RBCB} \times V_{RBCB}}{\alpha_{FPS} \times \rho_{FPS} \times V_{FPS}},$$

where

α = total fission rate in the fuel ($\frac{fiss}{g \times s}$),

ρ = density of fissionable material (g/cm^3) and,

V = equivalent recoil volume (cm^3).

In deriving this relation, C_{FPS} is normalized to unity and the parameters, V_{Na} , ϵ , and F , chosen for the FPS test, are equal to the ones used for RBCB operation. As can be seen, this new relation is independent of the efficiency of the detection system, ϵ .

To justify the use of data obtained from FPS tests, it must be noted that the FPS has been used in many calibration tests with the FERD; thus, a large body of base data has been accumulated. However, the most important feature of FPS test results is that the total surface area of the fuel material is known.

To be able to find the exposed surface area rather than the recoil volume, the value V is set to be equal to $S_{rc} \times W$, where, W is the experimentally determined recoil distance in the source material, and S_{rc} is defined as the "equivalent recoil area". It should be pointed out, however, that only in the case of a recoil emitter does S_{rc} represent an actual physical area. For nonrecoil sources (i.e., failed fuel elements

while in RBCB operation) S_{rc} provides a measure of the square centimeters of the source material that would produce a given FERD response if direct recoil were the only mechanism for release. Since it is well known that both recoil and nonrecoil mechanisms exist, this model can be extended to find the actual physical area in all cases. The equation for finding the S_{rc} is:

$$(S_{rc})_{RBCB} = C \times \frac{\alpha_{FPS} \times \rho_{FPS} \times W_{FPS}}{\alpha_{RBCB} \times \rho_{RBCB} \times W_{RBCB}} \times (S_{rc})_{FPS}.$$

Evaluation of GIRAFFE

During RBCB operation, it is crucial to determine the progress of the breach in a failed fuel element, since there is a regulatory and safety concern about the possibility of a flow-blockage being formed in the cooling system if the breached element is allowed to remain in the core for too long a period of time. From experience in EBR-II, it is found that the leaker diagnosis by only TG analysis is not sufficient, especially when operation continues well past the point of the initial breach. Even when enough TG and FG data are available, no correlation can be made with breach size. Therefore, the only means of finding the extent of the breach has been placed on DN signal analysis.

The analytical techniques, explained in this chapter, have been incorporated into the FORTRAN computer code GIRAFFE. Results obtained from using GIRAFFE as a diagnostic tool are reported in Gross and Strain [22]. The conclusions reached by Gross and Strain from the experimental results are reported in the remainder of the chapter.

GIRAFFE has been used to determine the value of the transit time (i.e., T_{tr}) and the results have indicated that there is a dependence between the computed

value of T_{tr} and the relative core location of the DN source. The quantities of T_h , calculated by GIRAFFE, were found to be affected by the form (i.e., geometry and composition) of the fuel exposed to the coolant as well as the condition of the breach site. Also, GIRAFFE was successfully used for determining the signal attributable to gamma activity in the coolant.

As was stated previously, the most important task of GIRAFFE is determination of the defect site surface area. Determining this surface area by only measuring the magnitude of the DN signal can result in an enormous error, since by doing so it is assumed that the only mechanism by which DN emitter are released is recoil. Exposed fuel tests performed with known defect sizes indicate that the DN signal produced may exceed the signal expected from direct recoil by as much as a factor of 234 [22].

We will conclude by reflecting the limitations of using GIRAFFE stated by Gross and Strain [22]. In developing this model, it is assumed that only one source, in addition to tramp and gamma background, is in the core, so if two sources are present with significantly different transit times and/or isotopic hold times this model does not produce an accurate estimate of either parameter. However, from the statistical information made available by GIRAFFE (i.e., by inspecting the residuals calculated from plotting the measured versus predicted activity and drawing the best-fit regression line), the presence of more than one leaker can be indicated. When tag signals are not well-characterized, this becomes the only means of determining the number of leakers in the core.

The Arrhenius behavior assumed for modeling the nonrecoil mechanism was derived empirically. Further research is needed to better understand the interplay of

the complex physical mechanisms that are responsible for transport of fission products and their progeny from the fuel matrix to the coolant under the various conditions that attend sustained operation with exposed fuel in a fast reactor [22].

The techniques developed here, both experimental and analytical, are limited to steady-state analyses. GIRAFFE does not account for the time dependency of the source term which is needed when a power change or an abrupt change in defect size occurs. To this effect, the currently used FERD system will be replaced by 3-DND. In Figure 3.1, it is shown that three detectors are connected in series and displaced in time along the sample stream flow path, thus producing a time delay of $\sim 5\%$ of the total transit time to the first detector. This delay time is sufficient to provide DN decay rate (and hence age) information that can be processed in parallel with gross detector count rates [25]. In the near future (January of 1991), the 3-DND system is scheduled to be calibrated. Thus, for this project, only the diagnostic tools (i.e., existence of a DN emitter, the magnitude of the DN signal, and surface-area diagnostics during steady state DN conditions) provided by the FERD system are available.

CHAPTER 4. DESCRIPTION OF FISSION GAS ANALYSIS

So far, the diagnostic tools provided by the TG and DN signal analyses for identification and surveillance of failed fuel elements have been described. Added to these analyses, measured FG activity has been employed for enhancing the tools already available and to provide new ones.

The FG originates in the fuel pins. The primary cover gas is contaminated with fission product gases (i.e., Xe- and Kr-isotopes), since major fuel element failures (cracks, ruptures) cause fission product gases to penetrate through the sodium into the cover gas as bubbles.

Up to the 1980s, it had been common practice to use the measured activity of FG in the cover gas for annunciating fuel failure and only very qualitative information about the type of breached fuel involved (oxide or metal) and its burnup (high or low) had been successfully extracted from gas release characteristics [18].

An analytical model has been developed which uses the measured activity of different FG in the cover gas. It provides not only the annunciation of fuel failure but also other diagnostic tools which can be employed for [26]:

1. estimation of the number of failed pins in the core,
2. differentiation of fuel-column failures from upper-weld failures,

3. indication of the severity or character of a breach,
4. anticipation of DN signal increase, and
5. acquisition of information on the possible breach mechanism.

In this chapter, the FG detection system in EBR-II, the analytical model developed which facilitates the diagnostic tools stated above, and determination of the degassing and the cover gas loss rate constants are described. The degassing and cover gas leakage rate constants are used in the analytical model for taking into account, respectively, the holdup time (defined as the confinement time that the FG spends in the sodium coolant before it is released into the cover gas) and the loss of cover gas from the containment. An accurate measurement of these constants is pertinent for successfully implementing the FG analysis. Finally, this chapter is concluded by evaluating the use of FG analysis as a diagnostic tool during RBCB operation.

Fission Gas Detection System

The brief description of the Germanium Lithium Argon Scanning System (GLASS) which has been used for monitoring the activity due to FG in the argon cover gas at EBR-II since 1972 is obtained from Brunson [18].

The high-resolution lithium-drifted germanium detector is connected to a gas sample chamber of ~ 25 ml volume through which the gas sample stream flows. The detector and sample chamber are shielded by lead. Other equipments positioned above the lead shield, are the high-voltage bias supply for the detector and a linear pulse amplifier. GLASS also has a multichannel analyzer and microcomputer located

away from the core. A 250 *ft* long cable is required for connecting the detection and the signal processing systems; as a result, a considerable amount of electrical noise is introduced. However, the resolution of the system has been $< 4\text{keV}$ as compared to 2.3keV under optimum conditions, for the 1.332MeV line of a ^{60}Co source.

When considerable fission product release has occurred, the cover gas activity increases by 3 or 4 orders of magnitude; therefore, in designing GLASS, it was recognized that the system must have a wide dynamic range to yield good data. This is done by decreasing the sensitivity of the system when the activity becomes large. The sensitivity is reduced in two steps: the effective volume of the sample chamber is decreased, and the sample gas is diluted. The spectral information is collected in a 2048-channel section of the analyzer memory on a 30 minutes cycle. The microcomputer is used for estimating the net count rate for each of several specific isotopes by merely subtracting from the summed counts under a peak, the summed counts from an equal segment of a representative Compton background at an energy just above the peak [27]. The microcomputer transmits the corrected data to the DAS, which handles essentially all plant data for EBR-II.

Similar to DNDs, it is difficult to convincingly calculate the geometric efficiency of the GLASS detector, since the detection arrangement is dictated so that a large source volume must be placed near a detector of a similar volume. Hence, the absolute concentrations of different isotopes are obtained by normalization to an independently measured concentration of ^{135}Xe . Of course, the normalization technique is successful when the time spent for detecting the activities of the different isotopes is relatively short, so that only negligible decay of isotopes occur during this period.

Development of the Analytical Model for Fission Gas Analysis

Similar to the TG analysis, in FG analysis, the frequent use of CGCS, which reduces the activity of the cover gas to the allowable level, makes any on-line diagnosis of correlation between FG activity from a breached pin and the condition of the breach difficult and at times impossible to perform. The tasks put forth for the FG analysis are performed by an analytical model which is primarily developed to calculate the FG activity while correcting for actions of CGCS (i.e., cover gas purging). Reference [26] is the source for the material presented in this section.

Fission Gas Transport Equations Corrected for Cover Gas Purging

The following assumptions are made to develop the differential equations for simulating the dynamics of the migration of FG upward through a layer of sodium into the cover gas:

1. There is ideal mixing in the sodium and the argon cover gas;
2. Disengagement of FG from the sodium to the argon is dependent on the concentration of FG in the sodium phase; and
3. Fission-product decay is fully described by considering only parent, metastable daughter, and daughter isotopes

The FG transport is mainly based on the assumptions that FG is released from a breached cladding site to flowing sodium in the core, and turbulent mixing with sodium breaks down FG bubbles to sizes small enough that their transport is similar to that of atoms. The concept of FG analysis is applied to interpret FG release

dynamics for seven isotopes: ^{133}Xe , ^{135}Xe , ^{135m}Xe , ^{138}Xe , ^{85m}Kr , ^{87}Kr , and ^{88}Kr .

The following set of coupled differential equations are developed for calculating the number of Xe and Kr isotopes:

$$\frac{d[2]CG}{dt} = [2]Na\lambda_d - [2]CG(\lambda_2 + \lambda_L + \lambda_p)$$

$$\frac{d[3]CG}{dt} = [3]Na\lambda_d + f_{23}[2]CG\lambda_2 - [3]CG(\lambda_3 + \lambda_L + \lambda_p),$$

where

[2] = number of metastable ^{85m}Kr , ^{88}Kr , ^{87}Kr and ^{135m}Xe ;

[3] = number of ^{133}Xe , ^{135}Xe , and ^{138}Xe atoms,

λ_i = decay constant of Xe , Kr , in s^{-1} ,

λ_d = disengagement-rate constant, in s^{-1} ,

λ_L = cover-gas-leak-rate constant, in s^{-1} ,

λ_p = cover-gas-purge-rate constant, in s^{-1} ,

[] $_{Na}$ = sodium phase,

[] $_{CG}$ = argon-cover-gas phase, and

f_{23} = branching fraction.

In these equations, cold trapping of iodine and bromine parents and holdup time in the sodium itself of FG, leakage of cover-gas, and effects of CGCS operation on FG are taken into account respectively by the constants, λ_d , λ_L and λ_p . The values of $([2]Na\lambda_d)$ and $([3]Na\lambda_d + f_{23}[2]CG\lambda_2)$ are the isotope-production terms, denoted as P_j . By assuming a linear approximation for an appropriate time interval and when purging is done, the values for P_j values can be calculated by:

$$P_j = \frac{dC}{dt} + C_j(\lambda_i + \lambda_L + \lambda_p),$$

where

dt = time interval between t_j and t_{j+1} , in s ,

dC = activity difference of FG i at the time interval dt , i.e., $C_{j+1} - C_j$,

C_j = measured value of activity at t_j , nCi/mL ,

λ_i = decay constant of FG isotope i , in s^{-1} .

The equation for no CGCS operation, can similarly be derived by excluding the term λ_p :

$$\frac{dC^*}{dt} = P_j - C^*(\lambda_i + \lambda_L)$$

where

dC^* = activity difference of FG i at the time interval dt for no purging, i.e., $C_{j+1}^* - C_j^*$.

Thus, in short, the algorithm for finding the activity of the FG isotopes corrected for CGCS operation is:

1. measure the initial activity for when CGCS is operating (i.e., C_0 at t_0),
2. set the values of $C_0^* = C_0$,
3. repeat step 4 through 8 until j , the number of time steps, is equal to the last time step,
4. determine the average value of the cover-gas-purge-rate constant λ_p during the period, t_j to t_{j+1} ,
5. calculate the source terms P_j by using the measured activity of the FG isotopes C_j and C_{j+1} ,

6. calculate the corrected activity C_{j+1}^* by using the values of P_j calculated in the previous step,
7. if the value of C_{j+1}^* is smaller than C_{j+1} then set $C_{j+1}^* = C_{j+1}$, and
8. increment j (i.e., $j = j + 1$).

Step seven of the above algorithm is needed, since when the time steps are inappropriately chosen while CGCS is operating, the corrected activity calculated is sometimes larger than the measured activity, because of the error in the numerical calculations. An upper and lower limit for the time step can be determined by setting $C_{j+1}^* \geq C_{j+1}$. The equations, corrected and not corrected for CGCS operation, are used to derive the relation for choosing the appropriate time step where the upper and lower limits are:

$$\frac{1}{\lambda_i + \lambda_L} \geq dt \geq \frac{1}{\lambda_i + \lambda_L + \lambda_p}.$$

By using the above relation, the values of the appropriate time steps were calculated for the seven FG isotopes and the extreme conditions were found to be, ($90hr \geq dt$ for ^{133}Xe) and ($20min \geq dt$ for ^{138}Xe).

To validate this method, Nomura and others [26] used measured activities for RBCB tests while the CGCS was operating and calculated the values of the corrected activity for the seven isotopes. The results indicated that there is little effect of argon purging on the shorter half-life isotopes; however, the longer the isotopic half-life becomes, the more significant becomes the change of calculated activity compared to raw activity, as was expected. They concluded that the method for subtracting the effect of CGCS operation has been well confirmed, since all calculated data on RBCB experiments show reasonable results.

The corrected activity of the FG isotopes can be used to calculate their time derivatives. This would provide plots of instantaneous release rates at each moment in time. Knowing the time of the occurrence of instantaneous release allows for detecting small gas releases, since the pre-existing activities, especially for long lived ^{133}Xe and ^{135}Xe can be ignored.

Cumulative ^{133}Xe Release

The accumulated amount of the FG released into the cover gas can provide information such as determination of the number of breached pins and the breach mechanism. This method requires calculating the quantity of released gas in an appropriate time interval. The net source rate is then calculated by subtracting the background rate from the production term, P_j , and multiplying the result by the length of the time interval and the cover gas volume. Then, to calculate the cumulative activity released with time, the accumulated activity calculated for the previous time steps is added.

The limitations on this method are: (a) only the longest lived isotope (i.e., ^{133}Xe) can be considered, since, by doing so, it makes it possible to compare directly with the calculated stored-gas activity in a pin without correcting for isotope decay within the appropriate time interval, and (b) only the gas releases where a large fraction of the stored gas is expelled in a time comparable to or smaller than the half life of ^{133}Xe ($\sim 5.3d$) are considered. However, the FG analyzer at EBR-II will be modified so that it can automatically correct for decay effects in the cumulative-release inventory, making possible the application to very small breaches that may intermittently release their gas over a long period of operation.

The number of failed pins in-core at any time can be determined from the cumulative ^{133}Xe by dividing the cumulative FG activity by the theoretically calculated ^{133}Xe activity stored originally in the pin, which in turn is calculated by using the information from a fuel failure location system such as gas tagging. However, it is suggested that the calculation of the number of breached pins can be obtained without knowing the location of the breach, since the theoretically calculated ^{133}Xe activity stored originally in the pin, is not affected by the kind of fissile element. This is because cumulative fission yields for ^{133}Xe for the main fissile species (^{235}U , ^{238}U , and ^{239}Pu) are almost equivalent. In other words, the calculation of the number of failed elements is also useful under an unidentified stage of breached-fuel operation, assuming fuels in the core have similar fissile contents with similar specific fission rates.

Release-to-Birth Ratio

The different mechanisms through which the FG is released from the breached pins (i.e., stored-gas, diffusional, and direct recoil) are briefly described here.

1. Stored-gas release is a pressure-driven release of internally stored-gas to the coolant. It is generally assumed that the stored-gas has achieved radioactive equilibrium in most cases (i.e., the gas has the same isotopic composition in every release).
2. Diffusional release occurs when FG comes from the fuel interior itself; hence, its rate is governed by the concentration gradient of isotopes through the fuel.

3. Direct recoil releases fission product atoms through recoil of the fuel surface at the moment of fission.

The mechanism for the release of FG at any time can be identified by the release-to-birth ratio technique. Namely, by using the least squares method, the best-fit value of the slope of $\log(R_i/B_i)$ versus $\log\lambda_i$ in a given time interval indicates the type of gas release. Based on simplified condition, equations for calculating the (R_i/B_i) ratio for the three modes of gas release are [28, 29]:

1. Stored-Gas Release;

$$\frac{R_i}{B_i} = \lambda_e \left(\frac{1 - \exp(-\lambda_i t)}{\lambda_i} \right)$$

2. Diffusional Release;

$$\frac{R_i}{B_i} = 3 \left(\frac{D_i}{\lambda_i a^2} \right)^{1/2}$$

3. Direct Recoil Release;

$$\frac{R_i}{B_i} = \frac{k S L_i d}{4 W_j}$$

The parameters used for the above equations are defined as:

λ_e = Effective escape-rate coefficient, s^{-1} ,

t = Irradiation time, s ,

D_i = Diffusion coefficient, $\frac{cm^2}{s}$,

a = Radius of the equivalent sphere of fuel, cm ,

k = Enhancement factor, dimensionless,

S = Geometric defect area, cm^2 ,

L_i = Recoil range of FG species, i , cm ,

d = Effective escape-rate coefficient, s^{-1} , and

W_j = Mass of fissile isotope j in RBCB pin, g .

By solving the above equations for steady-state conditions, the values of the change in $\log(R_i/B_i)$ with respect to $\log(\lambda_i)$ for stored-gas, diffusional, and direct recoil releases are respectively found to be -1, -1/2, and a small negative value.

The equations used for release and birth rates (i.e., R_i and B_i , respectively) in terms of the corrected activity, C^* are:

$$R_i = 37V \left(\frac{1}{\lambda_i} \frac{dC_i^*}{dt} + C_i^* \frac{\lambda_i + \lambda_L}{\lambda_i} \right) \left(\frac{\lambda_i + \lambda_d}{\lambda_d} \right)$$

for ^{85m}Kr , ^{87}Kr , ^{88}Kr , ^{135m}Xe , and ^{138}Xe

$$R_i = 37V \left(\frac{1}{\lambda_i} \frac{dC_i^*}{dt} + C_i^* \frac{\lambda_i + \lambda_L}{\lambda_i} - C_2^* \frac{f\lambda_{i-1}}{\lambda_i} \right) \left(\frac{\lambda_i + \lambda_d}{\lambda_d} \right)$$

for ^{133}Xe and ^{135}Xe ,

$$B_i = Y_{ij} F_j W_j$$

for the birth rate, where

f = branching factor,

V = cover gas space, cm^3 ,

Y_{ij} = cumulative fission yield of isotope i , fraction, and

F_j = specific fission rate for fissile isotope j .

For simplifying the analytical model, in defining release rates in terms of changes in measured cover-gas activities, the complex processes of iodine and bromine precursors, trapping by the cold trap, and decay of solid precursors are avoided. The

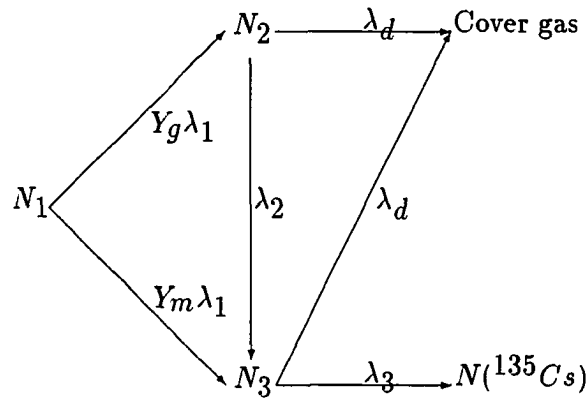
above equations are then used to calculate the behavior of (R_i/B_i) with time during gas release from RBCB operations.

Determination of the Degassing Constant

In the previous section the analytical method for FG analysis was described and also it was stated that an accurate approximation of the degassing constant used in this model is pertinent. The degassing constant accounts for the delay in release of FG from liquid sodium to the cover gas. In order to do this, an experimental facility, Toshiba fission product loop [30], has been used and an analytical model has been developed. In this section, the method which uses the experimental results from fission product loop to calculate the degassing constant is described. The main source for this description is Mitsutsuka et al. [31].

Two different xenon isotopes having considerably different half lives(i.e., ^{135}Xe and ^{135m}Xe) were chosen for comparing their release rate to the cover gas. These two isotopes are produced by decay of ^{135}I ; ^{135m}Xe with a 15 min and ^{135}Xe with 9.2hr half-life, respectively. Iodine isotopes dissolve in liquid sodium quite well at high sodium temperature and, accordingly, the xenon isotopes are homogeneously distributed in the liquid sodium.

In the schematic shown below, the combined effect of the decay and degassing constants on the concentration of the xenon isotopes in the cover gas is illustrated:



N_1 , N_2 , and N_3 are the number of atoms of the species, ^{135}I , ^{135m}Xe , and ^{135}Xe , respectively; and, λ_1 , λ_2 , and λ_3 are the decay constants of ^{135}I , ^{135m}Xe , and ^{135}Xe , respectively. The branching ratios of ^{135}I decay to ^{135m}Xe and ^{135}Xe are respectively denoted by Y_m and Y_g . Finally, the degassing constant is denoted by λ_d . Thus, the release rate of xenon isotope i from liquid sodium to the cover gas can be written as $R_i = \lambda_d \times N_i$.

The governing differential equations for the number of iodine and xenon isotopes are:

$$\begin{aligned}\frac{dN_1}{dt} &= -\lambda_1 N_1 \\ \frac{dN_2}{dt} &= Y_m \lambda_1 N_1 - N_2(\lambda_2 + \lambda_d) \\ \frac{dN_3}{dt} &= Y_g \lambda_1 N_1 + \lambda_2 N_2 - N_3(\lambda_3 + \lambda_d).\end{aligned}$$

The solution of these differential equations is obtained in the general form and simplified by recognizing: (a) a transient equilibrium is established between N_1 and N_2 , since λ_2 is larger than λ_1 , and (b) the decay constant λ_3 is smaller than λ_1 , so equilibrium is not anticipated; however, the sum of λ_d and λ_3 is larger than λ_1 ; thus, equilibrium condition can also be assumed between ^{135}Xe and ^{135}I (this will

be justified later in this section). Thus, the simplified solutions of the governing differential equations for calculating N_2 and N_3 are derived to be:

$$N_2 = \frac{Y_m \lambda_1 N_1^0}{(\lambda_2 + \lambda_d - \lambda_1)} e^{-\lambda_1 t}$$

$$N_3 = \frac{\lambda_1 N_1^0 e^{-\lambda_1 t}}{(\lambda_3 + \lambda_d - \lambda_1)} \left(Y_g \frac{Y_m \lambda_2}{(\lambda_2 + \lambda_d - \lambda_1)} \right),$$

where, N_i^0 is the number of atoms of isotope i initially at $t = 0$.

The release rate ratio of ^{135}Xe and ^{135m}Xe , $R_{3,2}$ (i.e., $R_{3,2} = \frac{\lambda_d N_3}{\lambda_d N_2}$) can then be calculated by,

$$R_{3,2} = \frac{Y_g(\lambda_2 + \lambda_d - \lambda_1) + Y_m \lambda_2}{Y_m(\lambda_3 + \lambda_d - \lambda_1)}.$$

Finally, this equation is rewritten, so that the degassing constant λ_d can be solved for, by knowing the value for $R_{3,2}$ which is measured experimentally. By plotting the release ratio $R_{3,2}$ versus time for different values of λ_d , it can be seen that as values of λ_d are increased, the time at which ^{135m}Xe and ^{135}Xe reach equilibrium decreases.

The equation for calculating λ_d is:

$$\lambda_d = \frac{Y_g(\lambda_2 - \lambda_1) + Y_m \lambda_2 - Y_m(\lambda_3 - \lambda_1)R_{3,2}}{(Y_m R_{3,2} - Y_g)}.$$

The release rate of isotope i , R_i is obtained by measuring the radioactivity of isotope i , A_i , in the flowing cover gas and by using the equation:

$$R_i = \frac{A_i V_1 (\lambda_i + f/V_1) (\lambda_i + f/V_2) e^{\lambda_i \Delta t}}{\lambda_i f},$$

where f is the cover gas flow rate, V_1 and V_2 are respectively the effective gas volume of the expansion tank (where argon gas is exposed to sodium coolant which is obtained

from the primary coolant) and the counting tank of the fission product loop, and Δt is the transport delay time from the expansion tank and the counting tank. The effect of f , the cover gas flow rate, on the release rates obtained for ^{135m}Xe and ^{135}Xe was found to be minimal if chosen in the range of $200 \sim 600 \text{ ml/min}$. Thus, the calculation of release rate is considered to be valid for the above cover gas flow rate range.

To calculate λ_d , the $R_{3,2}$ release ratio is obtained by knowing the R_3 and R_2 release rates. An experiment was performed and results were reported in Reference [31]. In this experiment the sodium temperature was varied to study its effect on the value of λ_d . While holding the experimental conditions constant, after two hours or more, the ratios became constant at each sodium temperature and showed values of 9.9 to 7.6. Degassing constant values of $1.2 \times 10^{-3} \text{ s}^{-1}$ and $2.6 \times 10^{-3} \text{ s}^{-1}$ were found for sodium temperature of 240°C and 390°C , respectively.

In developing the equation for calculating λ_d , we assumed that the sum, $\lambda_d + \lambda_3$, is larger than λ_1 , so that an equilibrium condition can also be assumed between ^{135}Xe and ^{135}I . The values reported for λ_d are at least two orders of magnitude larger than the decay constant of ^{135}I , λ_1 ; thus, justifying the assumption made earlier.

Mitsutsuka et al. [31] concluded their report by stating, "This method was found to be effective for determining the FG degassing constant, which has a corresponding half-life somewhere between several to 40 min and will be useful for the study of FG transport phenomena in liquid metal fast breeder reactors."

Determination of the Cover Gas Loss Rate

The material for the description of the two approaches which have been used for measuring the cover gas loss rate in EBR-II is taken from work reported by T. D. Claar [32] and R. G. Nobles [33]. In the first approach, the rate of decay of some gaseous isotopes normally present in the cover gas after a reactor shutdown has been used. A constant rate of gas leakage leads to a decrease in the measured activity of a radioactive isotope i according to a decay constant, λ_{eff} , that is larger than its radioactive decay constant λ_i . In other words, $\lambda_{eff} = \lambda_{loss} + \lambda_i$. The term λ_{loss} accounts for the total loss rate of cover gas discharged up the stack, and for cover gas samples taken out for TG analysis, and for leakage losses to the building. However, the flow rate of discharge through the stack and for the xenon tag recovery system can be measured.

This method was implemented by plotting the *log* of activity of the chosen FG isotope versus time after shutdown. Determination of the slope which corresponds to the value of λ_{eff} will lead to calculating the λ_L . By knowing the value for λ_i and other leakage rates, the value of the argon gas leakage rate was found to be $\sim 500\text{ml}/\text{min}$.

As continuing efforts reduce the leak rate, the leakage contribution to the effective decay constant will become small compared to the radioactive decay constant of the isotope chosen for the analysis. Thus, when lower leak rates are anticipated, isotopes with longer half-life are used.

It was observed that the error in fitting the data, i.e., log of the isotope activity, to a straight line was rather large. It was thought that this would be remedied by using another method which uses the ratio of the measured activity of the FG

isotopes. This complex iterative method resulted in a similar expression for the cover gas leakage rate; thus, the specifics of its development are not described here.

The second method used for calculating the cover gas leakage rate is based on first principles, namely, mass balance of the argon gas in the core. The basic equation is:

$$LR = SR - UR - AC,$$

where

LR = leak rate,

SR = supply rate,

UR = use rate, and

AC = accumulation rate.

The leakage rates calculated under different conditions, were found to be in reasonable agreement with the leak rates calculated using the method previously described.

Evaluation of Fission Gas Analysis

The diagnostic tools provided by the FG analysis for breached pin diagnosis were validated with an RBCB test in EBR-II [26]. In this test, the DN analysis techniques were performed in parallel with the FG analysis ones. Typical FG release characteristics were obtained by such diagnosis for three different types of breach on mixed-oxide elements; creep-rupture, FCMI, and plenum birth defect and the important observations were [26]:

1. All breached elements released stored-gas for some time interval.

2. Transition of release mechanism from stored-type to diffusional and lastly recoil type depends on the breach type.
3. Recoil release of FG appears to precede the first DN signal; similarly, this recoil FG release has invariably come after release of stored-gas from the pin and some diffusional release through the breach site.
4. FG release of a recoil type continues during stable and quasistable DN signal release.

In conclusion, Nomura and others [26] state: "Further development of these diagnosis techniques may allow them to be applied in an on-line system at a LMR as a reliable tool for operators."

CHAPTER 5. CHARACTERISTICS OF FISSION GAS STORAGE AND RELEASE

The history of FG analysis in EBR-II only pertains to two different occasions where the performance of mixed-oxide fuel was of interest. Nomura [26] outlined some FG characteristics for mixed-oxide fuel breaches from this study and developed a basis for an ES. The results were discussed in the previous chapter.

In developing a generic ES for diagnosing failure of mixed-oxide fuel, it was recognized that a more comprehensive study must be conducted. But most importantly, since the ES designed here will ultimately be used in the IFR concept (a reactor concept that includes usage of metal fuel).

Since there was no experience accumulated in the FG analysis for metal fuel elements, it was first necessary to become familiar with the results of this type of analysis. To accomplish this, the FG data from May of 1986 to April of 1990 were analyzed, with the hope of extending the study to analysis of data from the periods of time prior to May of 1986. The expertise gained from the analysis of FG data for this period was invaluable but as will be seen, by no means can it be claimed that it was comprehensive.

The data for this analysis were obtained from the DAS at EBR-II. In DAS, data are archived using different time intervals, ranging from one minute to one hour. The

main consideration in selecting the time interval for recovering the archived data was the amount of data obtained versus the accuracy of the calculation. It is desirable to use one-minute data in the numerical techniques for FG analysis, since the shortest half-life of the FG isotope studied is in the order of a few minutes. However, the task of copying one-minute data for an approximately five-years period would have required an unreasonable amount of time, and a large number of magnetic tapes for storing the data. Therefore, ten-minute averaged data were used which caused very little compromise in the accuracy of the calculations and at the same time were quite manageable. The only noticeable drawback was in retrieving the DN signal. Associated with some breaches, very sharp DN spikes are seen, particularly in metal fuel. When ten-minute averaged data are used, the DN spike is not noticeable, since by averaging the data over ten-minute intervals, spikes that have only a few second width are missing or decreased in amplitude.

In this chapter, to provide a better understanding of FG release from different metal and mixed-oxide fuels, a general description of radiation effects on different fuel types used in EBR-II is given. Also, a description of the diagnostic tools provided by the FG analysis is provided. Finally, by using the plots which depict the results of the FG analysis, we will study the behavior of FG release from breaches that have occurred in the past five years. The expertise gained from this analysis is then used to generate the rules used in the KB of the ES.

The material for the analysis of FG was gathered from numerous consultation sessions with W. N. Beck, J. D. B. Lambert, K. C. Gross, J. H. Bottcher, and R. V. Strain. This group has been directly involved in the design and performance of fuel elements (during normal, or RBCB operation) for many years at Argonne. W. N.

Beck is considered to be one of the pioneers in the metal fuel design program at EBR-II. The other members of this group have been the primary investigators in the RBCB program at EBR-II, emphasizing on the Japanese-RBCB program (concentrating on mixed-oxide fuel). Also, W. N. Beck, and K. C. Gross have directly been involved in the fuel failure diagnostics; thus, they are considered to be the domain experts in the development of this ES.

Radiation Effects on Metal and Oxide Fuel Elements

To better understand the results of FG analysis, a basic knowledge of radiation effects on metal and mixed-oxide fuel elements and FG release mechanism is required. In different types of metal fuel, it is seen that in general the radiation effects vary with the amount of plutonium enrichment and also with the irradiation time (burnup of the fuel). So far, in EBR-II, three types of alloys have been used, namely, with 0, 8, and 19 percent by weight plutonium. The burnup can also be categorized into three groups, less than 8, between 8 and 12, and higher than 12 atomic percent. In the case of mixed-oxide fuel, the variation in storage and release of FG is generally attributed to the burnup.

It must be noted that this generalization is rather broad. However, we will use this model for the development of this ES, since there are no alternatives. This shortcoming is due to the fact that, in approximately a third of the breaches detected in the past five years by FG analysis, the subassemblies containing breached elements were not positively identified by TG analysis at the time of breach; or, if they were, it was not clear which element in the subassembly had breached (since, some experimental subassemblies included more than one type of fuel element). Therefore, it is

impossible to incorporate any more detailed information on the effects caused by the differences in the alloy type and burnup in the analysis of FG data (for the past five years), even though we believe there is a strong correlation between the two.

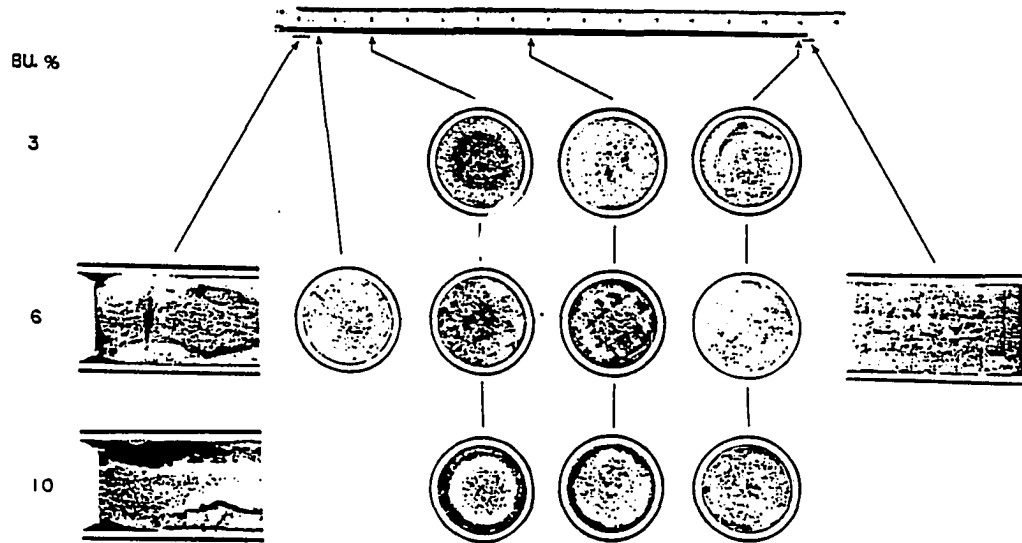
Before studying the effects of radiation, an important factor in FG release related to a difference in the design of metal and mixed-oxide fuel elements must be addressed. In metal fuel elements the gap between the fuel and cladding is filled with sodium, whereas, in mixed-oxide fuel the gap is filled with gas. As a result, mixed-oxide fuel elements, which have lower thermal conductivity values, operate at higher internal pressure than the metal fuel elements.

Also, in the discussion that follows, it is assumed that the FG has reached isotopic equilibrium. This is a safe assumption, since most natural breaches occur at burnup levels which require times that are orders of magnitude longer than the time required for reaching isotopic equilibrium.

In the remainder of this section, the storage and the release of FG (taking into account the type of fuel, burnup, and the breach location) are discussed.

Radiation Effects on Metal Fuel

The effects of irradiation on the storage of FG in zero, medium, and high plutonium content metal fuel are depicted in Figures 5.1, 5.2, and 5.3, respectively. At the initiation of irradiation the fuel is 100% dense, as is seen in the pictures in the top row of the figures provided. The peak of the neutron flux is located at the regions of the fuel whose pictures are provided in the columns in the middle. The general effects that are commonly seen in the three types of metal fuel are that, as irradiation progresses, the fuel expands due to the formation of bubbles. The gap between the



fuel and cladding allows for a 33% radial expansion of the fuel which is sufficient to permit inter-connection of gas bubbles. This in turn allows release of FG to the plenum region of the fuel element. As a result, the fuel becomes weak and the main loading on the cladding is caused by the gas accumulated in the plenum.

However, the distinction made in storage of gas between the three different fuel types is attributed to the segregation of the fuel content seen in medium or high enriched fuel at higher burnup, where the denser fuel migrates to the outer layer of the fuel. This is called the "banding effect." Depending on the radial temperature gradient and the enrichment of plutonium, the fuel content segregation can vary. Generally, this effect becomes pronounced in highly enriched ternary U-Pu-Zr metal elements at high radial temperature gradients. Along the bands of segregation, cracks, and voids, the transportation of FG to the outside of the fuel region is enhanced.

A typical schematic of a metal fuel element is depicted in Figure 5.4. In general,

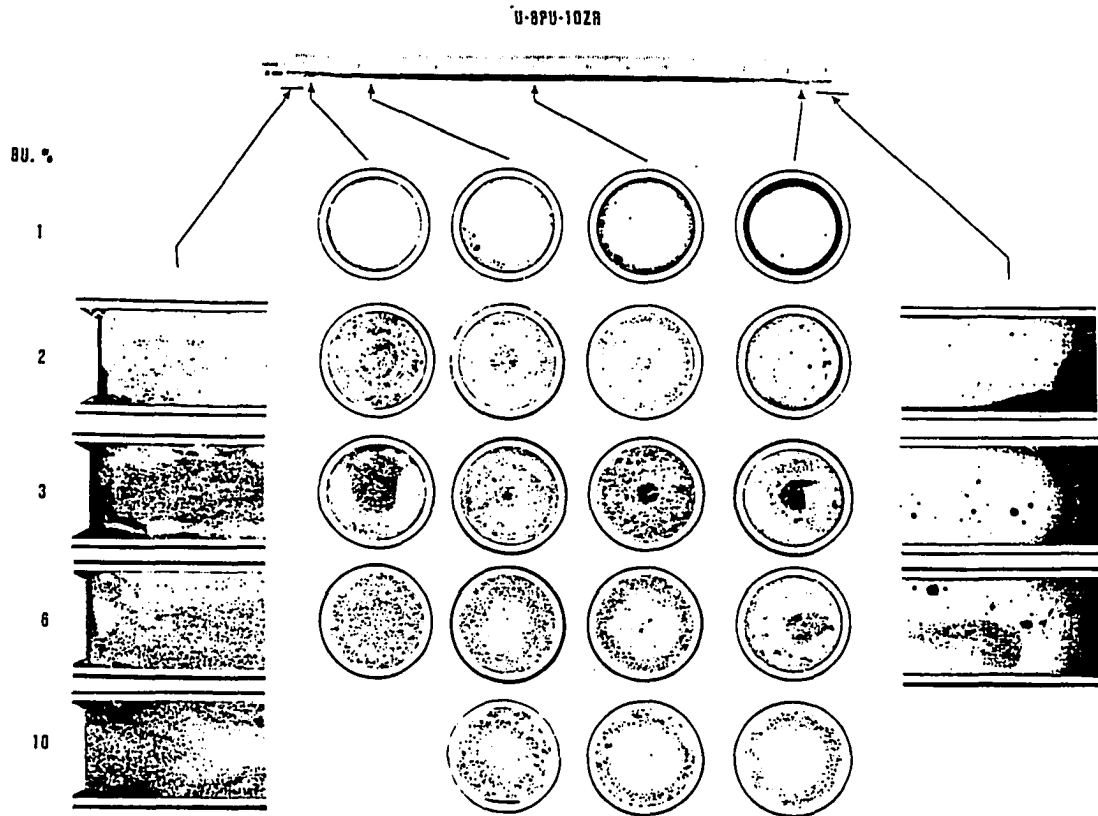


Figure 5.2: The effect of irradiation on 8 - Pu metal fuel

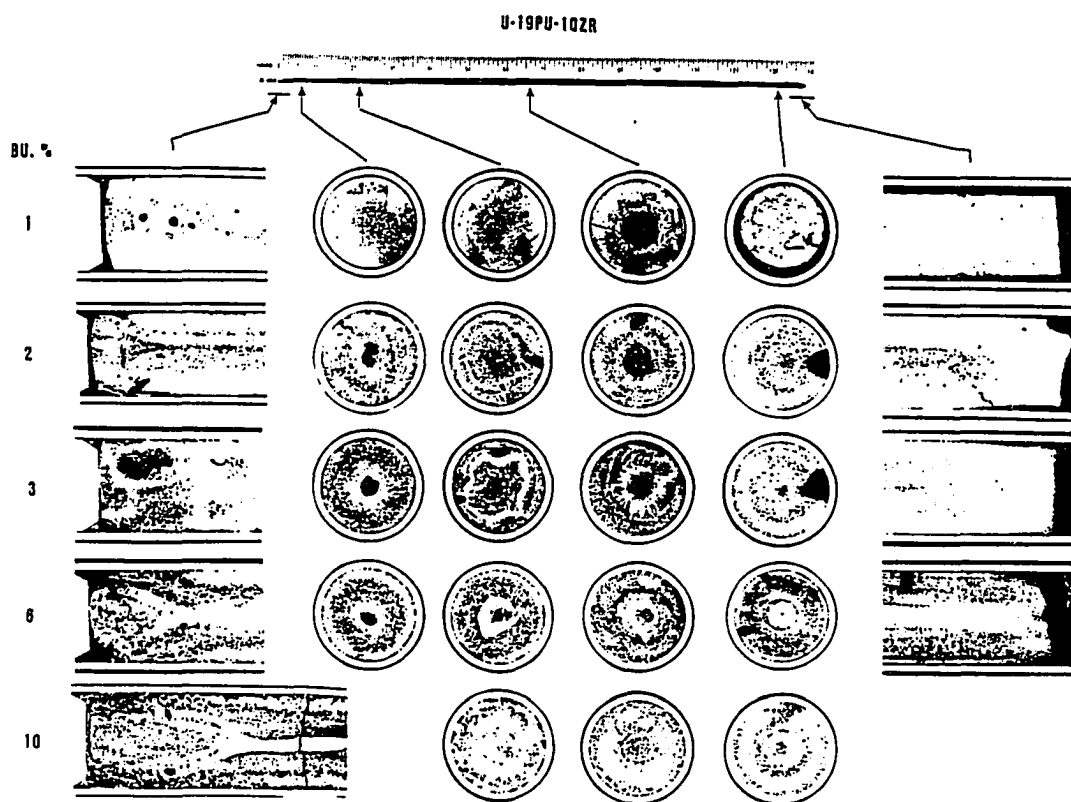


Figure 5.3: The effect of irradiation on 20 - *Pu* metal fuel

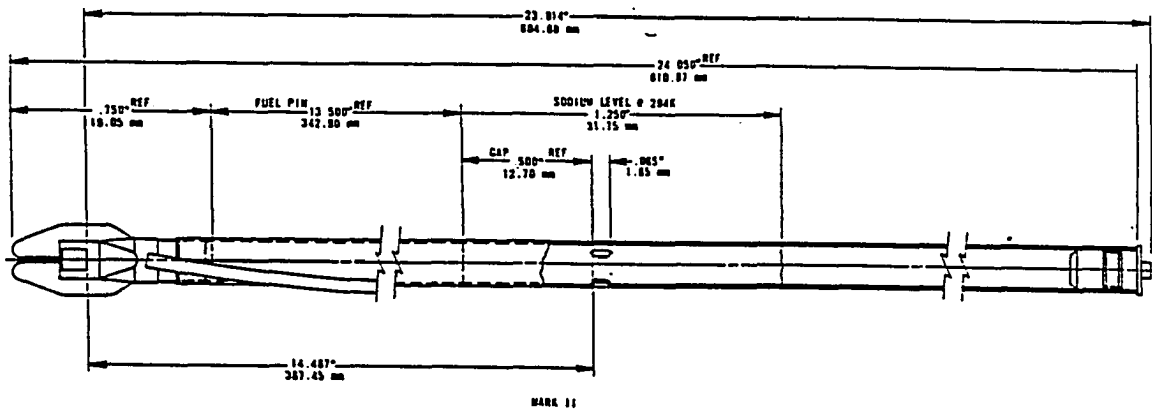


Figure 5.4: A typical design of a MK-II fuel element

the clad failures observed to date occur in three general areas, weld (plenum), dimple, and along the fuel column. In the case of a weld breach, the longer half-life FG isotopes are released and very little of the short half-life gas is expected to escape. This assumes that isotopic equilibrium of FG isotopes is reached. A typical breach due to weld failure is depicted in Figure 5.5. The breach size is the overriding factor in determining the release rate and volume of FG.

In the fuel column breach of metal elements, it is expected that the FG isotopes will be released from both the plenum and the fuel itself. However, it is expected that gas from the fuel region will be released first. The plenum gas (mostly long half-life FG) diffuses to the breached area, being driven by the pressure differential that exists between the plenum and the fuel column after the breach occurrence. This is even more pronounced if the location of the breach along the fuel column is close to the plenum. This is due to the fact that the irradiated fuel structure, as

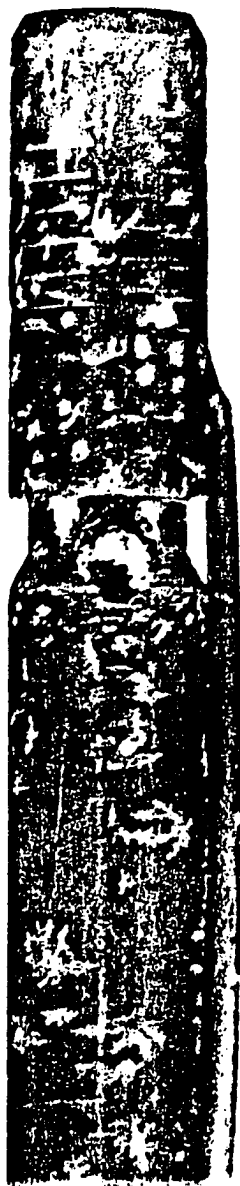


Figure 5.5: A typical weld breach in a metal fuel element

described previously, facilitates the release of the FG from the fuel into the plenum. However, if the fuel restricts the release of FG either to the plenum or to the breach site then a "bottle neck" effect is seen. Depending on the location of the breach with respect to the swollen fuel, the plenum gas release is affected. These characteristics are summarized in Figure 5.6.

A typical fuel column breach is shown in Figure 5.7. When the fuel column breach occurs, it is expected that most of the FG isotopes will be released by recoil from the surface of the exposed fuel. The DN signal emitted following metal fuel column breaches is caused by the release of cesium which is accumulated below the plenum gas and above the fuel region, as is illustrated in Figure 5.6. If any indication is given by the DNDs, the release of sodium and cesium causes only a sharp spike.

In the design of the MK-II metal fuel, dimples were included. This feature is displayed in Figure 5.4. Three dimples were manufactured by pressing the cladding immediately above the fuel region. The reason for including this feature was to confine the fuel inside the element. However, clad failures occurred at the dimple areas and so dimples were excluded from the successive metal fuel designs (i.e., MK-III and MK-IV).

In the dimple breach, the gas stored in the plenum (long half-life FG) has to compete with the gas generated in the fuel region (mixture of long and short half-life FG) for escaping to the coolant. If the fuel has interconnected porosity (thus the pressurization of the plenum region), it is expected that the FG from the plenum is most likely to prevail in escaping. Although in this type of dimple breach most of the gas is released from the plenum region, it differs from a weld breach. This difference is caused by the fact that the plenum gas must diffuse through the sodium

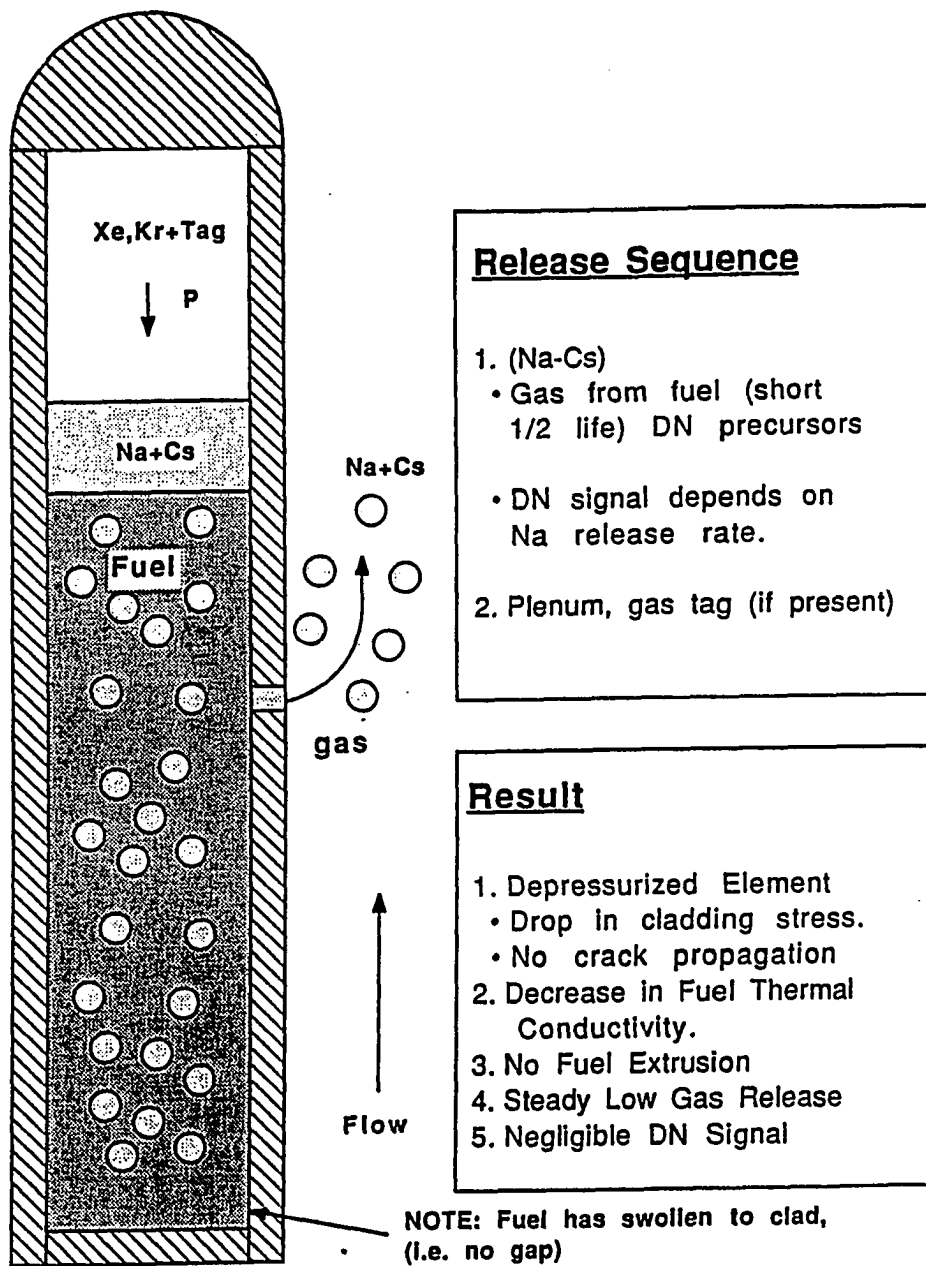


Figure 5.6: Metal fuel gas and DN emitters release characteristics



Figure 5.7: A typical pre-thinned fuel column breach in a metal fuel element

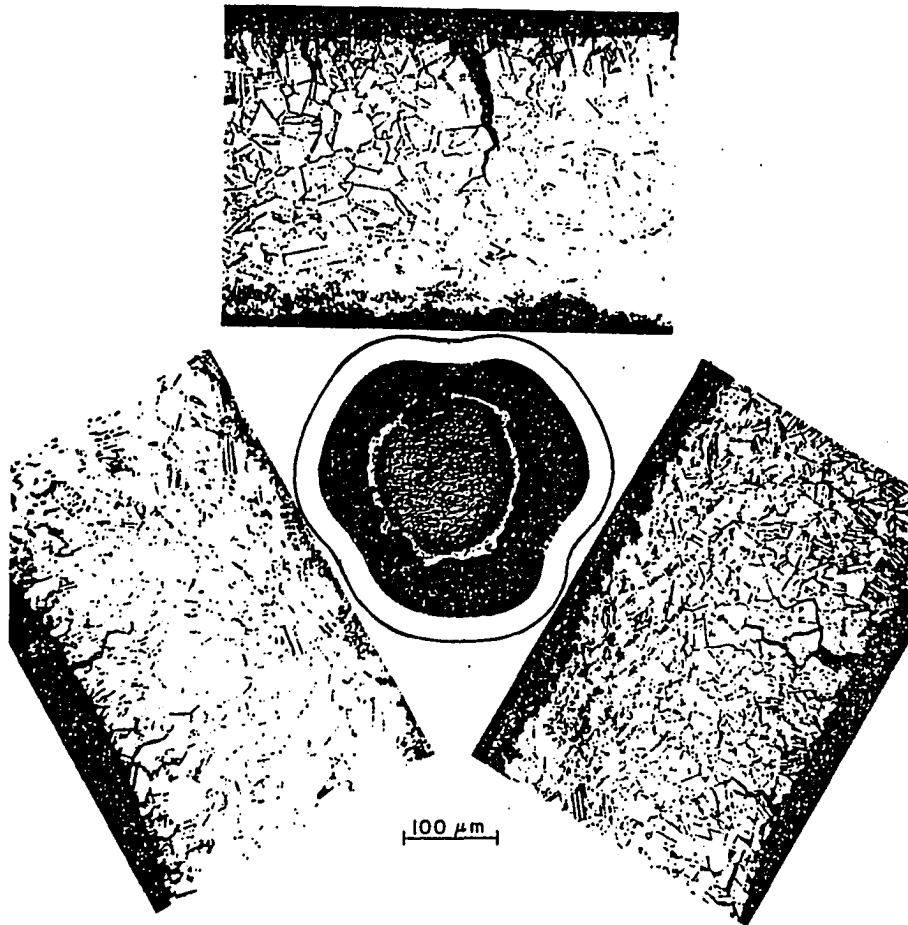


Figure 5.8: A typical dimple breach in a MK-II metal fuel element

contained in the element to reach the breach area, whereas, in a weld breach, there is no resistance mechanism to the gas release except the breach size. If the dimple breach occurs prior to the interconnection of porosity in the fuel, the breach appears to be similar to a fuel column breach. This type of breach is displayed in Figure 5.8.

Radiation Effects on Mixed-Oxide Fuel

The dimple and weld breaches in metal fuel elements are considered to be caused by manufacturing anomalies. The mixed-oxide elements do not include dimples as part of the design; also, natural plenum breaches have not yet been observed. However, the plenum breach in mixed-oxide fuel has been simulated by manufacturing the fuel element with a hole in the plenum region. The characteristics of this breach (which is not necessarily similar to a natural plenum breach) will be seen in the analysis of data in the next section. It is expected that plenum breaches in mixed-oxide fuels for the most part will behave similarly to those in metal fuel, with a difference in the rate of gas release after the initial burst of gas. It is expected that an irradiated mixed-oxide element readily releases gas at higher rates while still maintaining fuel strength even at higher burnup levels. This provides a better mechanism of transport of FG to the plenum region in mixed-oxide fuel.

In a fuel column mixed-oxide breach, we would expect that a great quantity of stored FG will be released initially. This stored gas would primarily consist of the FG isotopes with longer half-life, since it is assumed that the FG has reached isotopic equilibrium. After the initial burst of gas, the mixed-oxide fuel element is depressurized, and sodium can enter the fuel pin. In this case, a sodium uranate product is formed at the fuel clad interface and is ultimately released to the coolant. Sodium uranate results from the chemical interaction of sodium with fuel at the fuel clad interface. This causes an unusual rise in the level of the short half-life gas in the cover gas, since the FG is now generated in the coolant. After a period of time the gaps allowing sodium uranate release close and a steady release of both short and long half-life gas via diffusion from the fuel element itself is expected.

The volumetric expansion of the reaction product produces additional stresses on the cladding, causing the breach to enlarge, and exposing greater quantities of fuel to the coolant. Therefore, in mixed-oxide fuel column breaches, we expect to observe an indication of the breach by finding an increase in the FG activity at first, followed by an increase in DN signal after a period of time.

In mixed-oxide fuel elements, the breach is theoretically believed to be initiated by either the internal-over-pressurization of the element (creep-rupture) or FCMI. The distinction between FCMI and creep-rupture is clearly outlined in theory; however, it can not be as obviously identified from the data analyzed in the past five years. Therefore, we will avoid distinguishing between these two types of fuel column breaches in the mixed-oxide fuel until more evidence of these phenomena have been detected.

Another phenomenon, observed in both metal and mixed-oxide fuel elements during the diffusion in fuel column breaches, is sudden release of excessive short or long half-life FG. For the lack of better term, we call this "burping of FG."

Finally, background on the characteristics of the storage of FG in fuel and release of FG from the fuel element is presented, so that the analysis of the FG data provided in a later sections would become clearer. This field is very extensive and we only scratch the surface.

Description of the Diagnostic Tools Provided by FG Analysis

The three diagnostic tools which are provided by the FG analysis are: (1) the corrected-for-purging activity of seven FG isotopes, (2) the cumulative ^{133}Xe , and (3) the slope of release to birth ratio of seven FG isotopes versus their decay con-

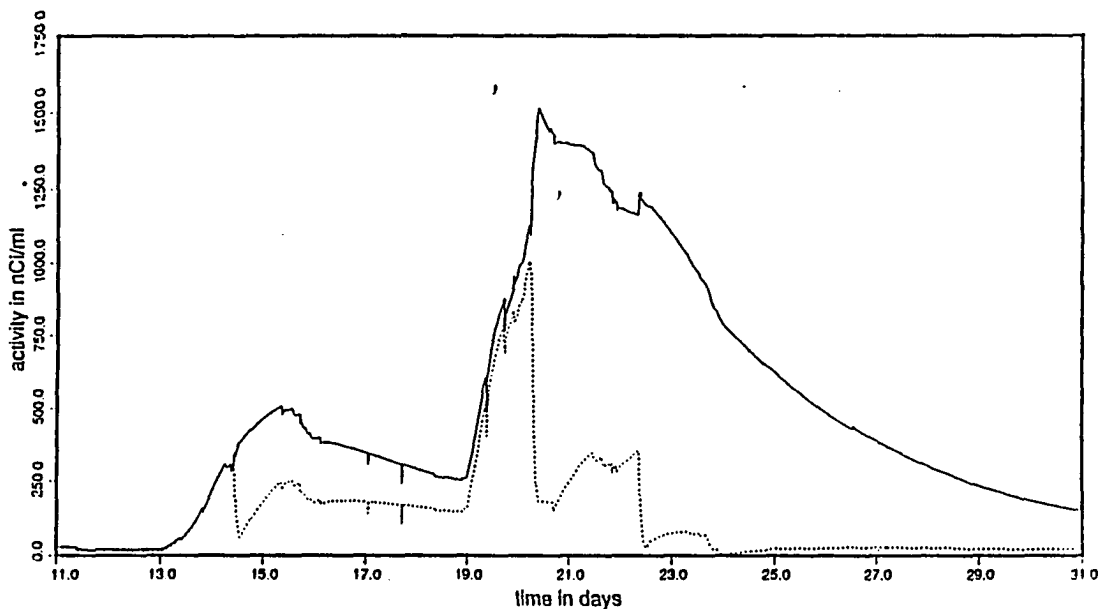


Figure 5.9: The corrected and not corrected-for-purging activity of ^{133}Xe

stant at a given time. The analytical methods which are used for developing these diagnostic tools were described in Chapter four.

The activity of FG isotopes, when corrected for purging, shows a higher value, as is expected. Also, it is expected that the longer the isotopic half-life becomes, the more significant the change of corrected activity from raw activity becomes, since the effect of purging is negligible compared to loss due to radioactive decay in isotopes with a shorter half-life. Therefore, the effect of purging of cover gas on the activity of ^{133}Xe can clearly be observed. Also, the raw and corrected activities for ^{133}Xe and ^{135m}Xe (which are representatives of the longer and shorter half-life FG isotopes, respectively) are depicted in Figures 5.9 and 5.10.

The activity detected by the GLASS at EBR-II is often used for initiating cleanup of cover gas. However, once the CGCS has been operated the true value of the activity of the FG in the cover gas is lost. Thus, one could not use it as a diagnostic tool. By

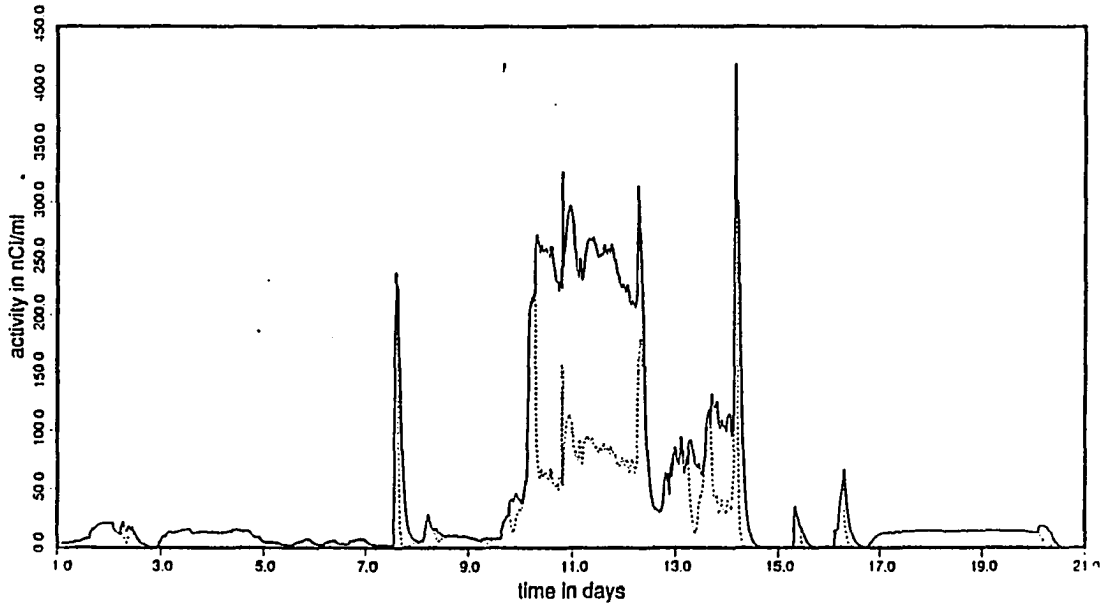


Figure 5.10: The corrected and not corrected-for-purging activity of ^{87}Kr

providing the corrected-for-purging activity, this piece of information can be used as a diagnostic tool, since by knowing the true activity of FG released, one can distinguish between the mixed-oxide and metal breaches.

The second diagnostic tool, cumulative ^{133}Xe activity, can be used as an indicator of a new breach. The equilibrium activity of stored gas of ^{133}Xe is estimated to be $500\text{Ci}/\text{pin}$. Also, a distinct change in the slope of the cumulative activity is seen when stored gas is released in a new breach. However, in analytical methods used for calculating the cumulative activity, there is no mechanism which takes the decay of FG activity into account long after the initial release of the stored gas. This, unfortunately, invalidates the use of cumulative activity in multi-breach situations. In calculating the cumulative activity for the past five years, we have set this value to zero when the ^{133}Xe activity reaches background level. This will not remedy the problem of over-accumulation; however, it allows resetting the value when the

effects of breached elements which have been left in-core for long periods of time have disappeared, or when there are not any breached elements present.

The third and most powerful diagnostic tool provided by the FG analysis is the slope of release to birth ratio of the seven FG isotopes versus their decay constant at a given time. A typical three-dimensional plot of the release to birth ratio versus decay constant at a given time is depicted in Figure 5.11. Using the least square method, the best fit line is obtained whose slope is used as a diagnostic tool. In this surface plot, the effects of a mixed-oxide fuel column breach on the release to birth ratio of the seven FG isotopes are seen. In the remainder of this discussion, for the sake of simplicity, the absolute value of the slope is used. For example, if the slope is -0.1 we will refer to it as 0.1 .

The plot of the slope with time indicates the type of breach (fuel column or plenum) and also indicates the characteristics of the progress of a breach. Coupled with the DN analysis, it is a powerful tool for indicating the severity of the breach. This information is available, since, the slope can be used as a tool for comparing the release of the seven FG isotopes relative to each other. In simpler words, when a slope of greater than 0.5 is seen, we have an indication that more of the longer half-life isotopes have been released than the shorter half-life ones, and when a slope is less than 0.5 the opposite is indicated. When the slope is approximately 0.5 we have an indication of diffusional release from the fuel element itself.

FG Analysis of Breached Elements (May 1986 to April 1990)

For analyzing the FG behavior, FORTRAN programs were developed using the models described in the previous chapter and the results were plotted. The plots

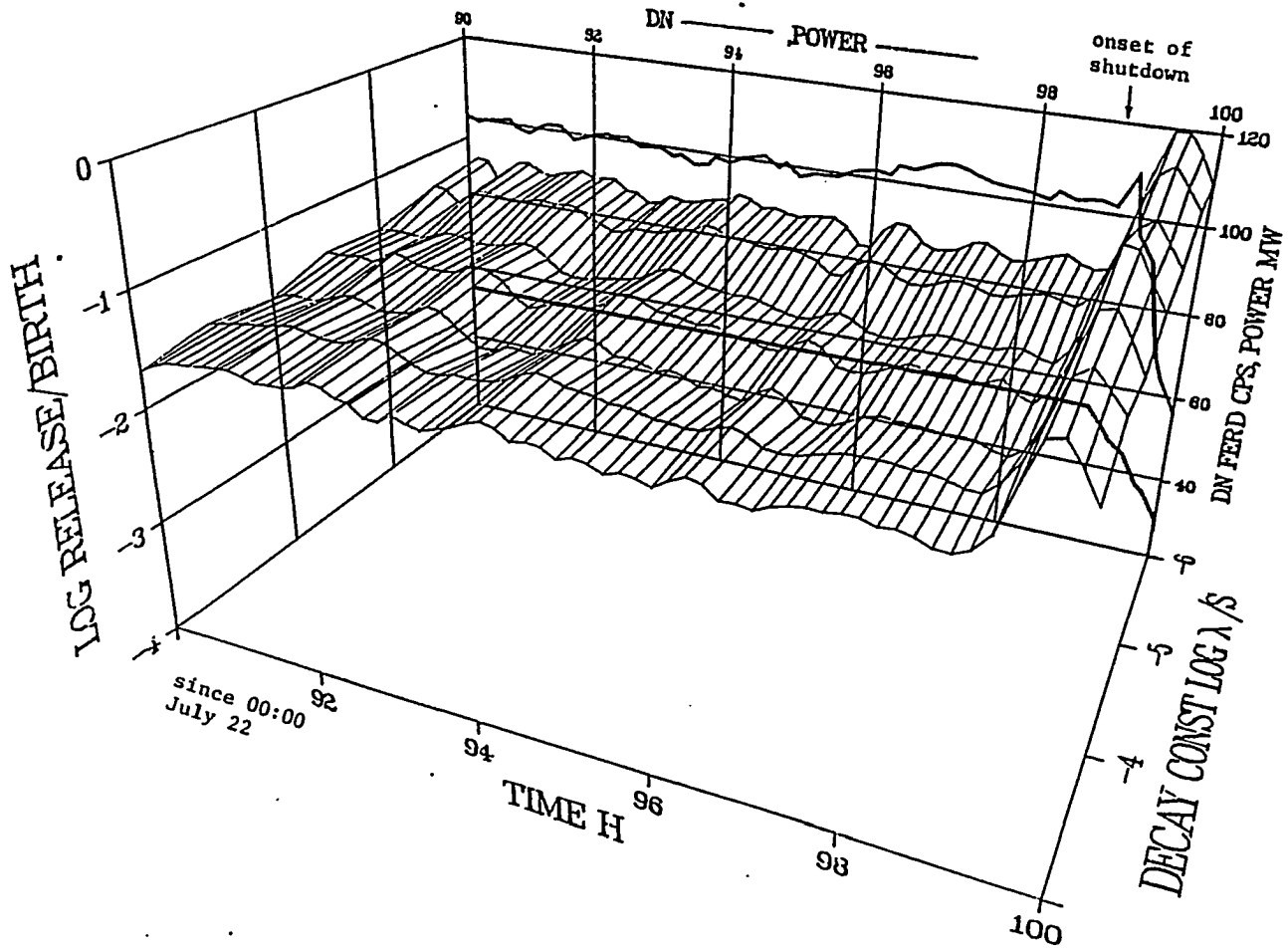


Figure 5.11: An arbitrary surface response of release to birth ratio and decay constant for seven FG isotopes with time lapse of irradiation

included were the reactor power, DN signal corrected for purging activity of ^{135m}Xe , ^{87}Kr , ^{133}Xe , the cumulative activity of ^{133}Xe , and the slope of the release to birth ratio of the seven FG isotopes considered versus the decay constant.

For identifying a breach all plots had to be studied simultaneously and it seemed logical to display the plots in parallel. The seven The FG isotopes can be categorized according to their half-lives into three groups. The FG isotopes ^{133}Xe , ^{87}Kr , and ^{135m}Xe with half-lives of 5.3 days, 1.3 hours, and 15.3 minutes respectively are chosen to show the behavior of FG isotopes with long, medium, and short half-lives. Otherwise, due to the number of plots that had to be displayed in one place, preparation of this display would have not been manageable.

As will be seen in the plots provided, the value of the slope is not provided while the reactor is not at power. The reason is that the value of release to birth rate of the FG is meaningless when the fission rate value is very small.

One of the main difficulties encountered in analyzing the FG data was that many breaches were not identified by TG analysis, due to operation of CGCS for removal of the FG from the cover gas. Along with the FG, the TG is also lost. It has been common practice to tag only some experimental subassemblies. In particular, during the past five years some experimental metal fuel elements that breached were not tagged. However, after the subassemblies are removed (sometimes many reactor runs later), breached elements in the subassembly were identified by post-irradiation examinations. Mostly, untagged metal fuel elements that breached remained in-core for many runs, since breached metal elements release negligible amount of DN signal and reactor operators are required to take action only when a high level of the DN signal is detected. In Tables, 5.1, 5.2, 5.3, and 5.4, which contain the listing of

breached elements, the suspected leakers (not detected by TG at the time of breach) are indicated by attaching a question mark to their subassembly name. Also, the star attached to the subassembly names indicates that the subassembly was placed in-core with an already breached element.

The results of the FG analysis are plotted on a monthly basis for the entire five years. A complete set of these plots is provided in the Appendix. Only the important events that allowed for deriving some of the heuristic rules for the development of the ES are discussed and redundant discussions are avoided.

Analysis of Breached Elements in 1986

In Table 5.1 a listing of the breaches that occurred during 1986 is given. In May, reactor run 139A began after a long reactor shutdown with no breached elements present in-core, as was indicated by the appearance of the background level of DN signal at approximately 200cps, absence of FG, and the existence of tramp background in the slope plot. When there are no breached elements in-core, there is very little release of FG from the tramp uranium which is dispersed uniformly in the coolant, causing a uniform distribution of points between 0 and 0.4, as is observed in the plot of slope. At the end of run 139A, on May 20th, a mixed-oxide element breach along the fuel column region occurred which caused a spike in the DN signal which in turn caused the shutdown of the reactor. When a breach causes the shutdown or when a breach occurs in a short reactor run (less than 5 days) the characteristics of the FG release are not observed, since the fission rate drops immediately and the release of FG is not stabilized after the initial burst of gas.

After the shutdown of the reactor, the internal pressure of the element dropped

Table 5.1: Listing of breaches in 1986

	Date	Leaker	Fuel Type	Burnup	Breach Type
1	05-20	XY-7C	oxide	mid.	fuel col.
2	05-25	XY-7C	oxide	mid.	fuel col.
3	05-29	XY-7C	oxide	mid.	fuel col.
4	06-01	XY-21A	metal 0Pu	high	fuel col.
5	06-10	XY-7C	oxide	mid.	fuel col.
6	07-08	X385A	oxide	low	fuel col.
7	07-27	X426	oxide	high	fuel col.
8	07-28	XY-19A*	oxide	high	fuel col.
9	08-04	XY-19A	oxide	high	fuel col.
10	10-22	X399A	metal 0Pu	med.	fuel col.
11	10-24	X399A?	metal 0Pu	med.	dimple
12	10-27	X399A?	metal 0Pu	med.	dimple
13	11-17	X381B	oxide	high	fuel col.
14	11-23	XY-23*	oxide	med.	fuel col.
15	12-10	X396	oxide	med	fuel col.

and as a result, sodium was allowed to enter into the element. The sodium remained in the element during the shutdown period and as of result sodium uranate was formed. The operating limit on the DN signal was then raised to allow further irradiation of the experimental subassembly XY-7C. When the reactor was brought up to power, the sodium uranate by-products were released to the coolant, causing a rise in the DN signal to a higher level than the one initially observed at the birth of the breach. This is observed at the startup of the second segment of run 139A.

A few days after the occurrence of the second breach in XY-7C, FG was released by diffusion from two elements, indicated by the slope of approximately 0.5. Another commonly encountered phenomenon, which occurs at the startup of a run with a breached element in-core, is that the slope value is initially one and grad-

ually decreases. This is explained by the fact that a fraction of the long half-life isotopes released from the breached element in the previous reactor run still exists in the cover gas, even though FG was not generated during shutdown. Thus, when the reactor is started up again, which results in generation of short half-life gas, the value of the slope gradually decreases. This behavior is observed at the startup of the second segment of run 139A on May 22nd. On May 25th and 29th, two other mixed-oxide elements breached in XY-7C with similar characteristics. The slope plot shows erratic behavior when elements are breached; and after a short period of time, diffusional release is observed with occasional indication of burps. Coinciding with occurrence of the breach, a step increase in the cumulative activity is observed.

On June 4th, a metal element breached. This breach was identified from the tag information and by examining the element after removal from the core. However, there was no indication of this breach from the FG activity or DN signal. The reason was that FG released from a metal fuel is approximately two orders of magnitude lower than from mixed-oxide fuel. In simpler words, the FG released from the breach in the metal element was swamped by the FG released by the three previously breached mixed-oxide elements. Finally, the breach of a fourth element in XY-7C caused the termination of run 139A. The subassembly XY-7C was then removed from the core while XY-21A remained in-core.

To verify the statement, "mixed-oxide elements release more gas than the metal elements," the gas released from the mixed-oxide elements during June 1st to June 5th is compared with the gas released from the metal fuel during June 21nd to 26nd. In both cases, there was diffusional gas release. Another interesting observation from this comparison is that the calculated values for the slope during diffusional release

are higher in the later period than in the earlier one. This is caused by the large quantity of long half-life gas released in run 139A contributing to the gas released from the metal element.

On July 8th, unique characteristics were observed from the breach in subassembly X385A. The mixed-oxide element released gas a few days prior to the release of the DN emitter. Also, gas was released in two steps and in the second step more of the shorter half-life gas was released. From observing this behavior, occurrence of a creep-rupture breach was indicated. However, for the lack of more evidence from the post irradiation examination of the element and lack of experience in the behavior of this type of breach, we refrained from reaching such a conclusion.

Subassembly X385A was removed before startup of run 139E. In run 140A a typical mixed-oxide element breached. Very little ^{133}Xe was released due to the immediate reactor shutdown and the fact that the breach site was located along the fuel column. The characteristic of a new breach was not seen in the plot of slope due to the short duration of run 139E. The subassembly X426 was removed from the core at the end of run 140A. At the startup of run 140B, subassembly XY-19A, which had already contained a breached element, was placed in-core.

On Aug. 4th, another element in XY-19A breached, causing a step increase in the DN signal. The burping effect was very pronounced from this breach. This can be attributed to the high burnup level of the elements in this subassembly. At the end of run 140B, a large release of gas was observed. This gas was associated with the second breached element in XY-19A. The gas stored in the central void of this element was confined by hardened fuel surrounding this central void. A sudden decrease in the temperature of coolant outside the fuel caused a large radial temperature gradient

across the central void region, resulting in the formation of a crack which allowed a sudden release of gas from the void.

The subassembly XY-19A was kept in-core for run 141A. At startup of 141A a DN spike is observed which is not associated with occurrence of a new breach. However, it is associated with the sudden release of DN emitters from the breached elements in XY-19A. During the reactor shutdown the coolant pumps are not operating which causes the sodium in the breached fuel element to stay dormant. At the startup for the successive run the sodium in the breached element, which contains excessive sodium uranate by-products, is pumped into the core resulting in detection of a DN spike by the DNDs.

During the month of October, three metal elements breached in subassembly X399, one being a fuel column breach and two a dimple breach. The stored gas release from a metal fuel column breach was much smaller than the release from the fuel column breach of a mixed-oxide element in XY-19A. However, the release from the metal breach was noticeable since the existing mixed-oxide breached elements had diffusively released gas for a long period of time. In comparing the behavior of dimple breached elements with the fuel column, it was observed that more of long half-life gas is released in the former type of breach as is indicated in the plots of slope and ^{133}Xe activity. Run 141A was terminated due to the breach of a mixed-oxide element in X381B. After the termination of run 141A all sources of FG were removed from the core and subassembly XY-23, which contained a breached element, was placed in-core.

In run 141B, it is seen that the power level is suddenly dropped and raised to the original value. This power change was accompanied by a change in DN signal. The

change in power caused an increase in the pressure difference across the breach surface, favoring a sudden release of DN emitters. This pressure difference was induced by a sudden change of temperature in the coolant as compared to the temperature of sodium trapped in the breached fuel element. Since XY-23 contained a fuel column breached element, escape of shorter half-life gas is seen to accompany the DN emitters. This is also indicated by a sudden decrease of slope. XY-23 was removed after termination of run 141B. In run 141C, an over-power test was conducted to study the performance of elements in X396. Due to the power spike occurring at the end of 141C, an element in X396 breached, releasing an excessive amount of ^{133}Xe . This activity decreased to levels lower than 200nCi/ml , and the value of cumulative ^{133}Xe was set to zero. To this point, the value of the cumulative activity in the cover gas for the entire 1986 period, during which 15 clad failures occurred, was calculated. It can be confirmed that the total number of failed fuel elements was 15, since approximately 500Ci is associated with the release of ^{133}Xe from each failed element; thus, for 15 failed element 7500Ci must be accumulated. This is the cumulative ^{133}Xe calculated at the end of 1986.

Analysis of Breached Elements in 1987

A listing of the failed elements and the time of failure is given in Table 5.2, where those breaches not identified by the TG analysis are identified with a question mark. Most of the sources of FG that were not identified by TG analysis were the elements in subassemblies X420A and X421A. The only information available for identifying the failed elements in these subassembly was the total number of breached elements in each of these subassembly, and the type of breach. This was extracted from the

Table 5.2: Listing of breaches in 1987

	Date	Leaker	Fuel Type	Burnup	Breach Type
16	01-14	X420A?	metal	?	weld
17	01-19	X420A?	metal	?	weld
18	02-06	X381B	oxide	high	fuel col.
19	03-10	MK-II	metal 0Pu	mid.	dimple
20	04-05	MK-II	metal 0Pu	mid.	dimple
21	06-27	X420A?	metal	?	fuel col.
22	07-03	X420A?	metal	?	fuel col.
23	08-13	X420A?	metal	?	weld
24	08-28	XY-27	metal 8Pu	low.	weld
25	09-02	X421A?	metal	?	weld
26	09-05	X421A?	metal	?	weld
27	10-11	X421A?	metal 19Pu	high	fuel col.
28	11-08	X429	metal 0Pu	low	weld
29	12-07	X421A?	metal	?	fuel col.

post-irradiation examination of elements in these subassemblies. Fortunately, from the FG analysis, it was possible to distinguish between a weld and fuel column breach in metal elements. Therefore, we were able to associate a breach with an element in this subassembly by keeping in mind the total number of breached elements in each subassembly and the type of breach. However, we were not able to indicate the burnup level or the alloy type of these elements, since the sequence of the occurrence of the breaches was not known and also in each of these subassemblies, elements with different types of alloy were used.

During the first 8 days of January, background levels in the DN signal and the short half-life FG were observed. Normally, the background level is characterized by uniform distribution of points below 0.3 in the plot of slope. However, due to levels of

activity of ^{133}Xe higher than the background (caused by the last breach occurring in 1986), unique characteristics were observed in the plot of slope. Nevertheless, when the activity of ^{133}Xe reached the background level, only tramp characteristics were observed.

On January 14th and 19th, two elements failed due to faulty welding. Associated with these breaches, no release of DN emitters and short half-life gas is observed. However, a considerable amount of long half-life gas was released, as was expected. The plot of slope shows identical characteristics to the activity of long half-life gas, since this was the only contributing factor in the calculation of slope.

On February 7th, a mixed-oxide element breached in subassembly X381B. Due to the high burnup level of this element, excessive amounts of DN emitters were released into the core which ultimately caused the termination of run 142B. Subassembly X381A was removed from the core after the termination of run 142B. During most of run 143A, the reactor did not contain any breached elements. On March 10th, a MK-II driver fuel breached in the dimple region. Very little short half-life gas was released from this breach, however, considerable long half-life gas was released to the cover gas. The long half-life gas was released for a longer duration with a smaller initial burst than the one observed from a weld failure. Another MK-II dimple failure occurred on April 5th, which showed identical characteristics. Important characteristics of the weld and dimple breaches are, no DN signal increase and negligible increase in activity of short half-life gas.

On May 6th, gas release is seen even though the reactor is shutdown. This gas release is caused by removing or moving subassemblies containing breached elements. Initially, the background levels in the DN signal and FG are observed in run 144A.

The level of the DN signal and short half-life gas is observed to vary with the level of reactor power. After ten days of irradiation, relatively small amounts of long half-life gas was released from either one or a combination of the breached elements in subassemblies, X420A, X421A, and 2 MK-II elements. We believe that this gas was released from the elements that breached due to weld failure, since in this type of breach the breach size is relatively small, thus allowing release of gas for a relatively longer duration of time.

On June 27th, the characteristics of a fuel column breach on metal fuel were observed. This event was repeated on July 3rd. Both breached elements were believed to be in subassembly X420A, since no other metal elements could have been suspected to have breached along the fuel column during run 144A. The amount of gas released is considerably smaller than the gas released from the mixed-oxide fuel. Also, contrary to the behavior of mixed-oxide fuel column breach, there is no indication of the release of DN emitter.

At this point, a clear picture of the FG characteristics of weld and fuel column breaches on metal fuel was observed and a comparison was conducted. In a weld breach, emission of short half-life gas is not seen, whereas in fuel column breaches noticeable amounts are detected. Also, in weld breaches, the amount of long half-life gas released is considerably more than the gas released from a fuel column breach.

The FG behavior of the next four breached elements were similar to the fuel column and weld breaches, previously described. On October 11th, a unique breach along the fuel column occurred in a 19% Pu metal element. The gas release characteristics indicate that the gas is cycling in large cavities which are formed in 19% Pu, highly burned up metal elements; thus, releases occurred with a frequency of

approximately 12 hours. In one of the cycles, gas accumulated in a large void was released and caused a spike that showed characteristics of occurrence of a new breach.

In run 146A, on Nov. 8th, a metal fuel breached in the plenum region. The effects of the breach have been distorted due to changing of the reactor thermal power.

At the end of November, a sudden increase in the activity of ^{135m}Xe was observed. This was caused by the release of pockets of gas that form on the inner surface of the cladding of the fuel column breached elements.

On December 7th, a fuel column breach occurred in a metal element placed in subassembly X421A. The effects of inter-connection of voids and ultimately formation of cavities, which causes depressurization of the element and release of stored gas, are shown, where a considerable amount of FG was released approximately 20 days after the element initially breached.

Analysis of Breached Elements in 1988

A listing of the breached elements is given in Table 5.3. The subassemblies X420B and X421A contained elements that were not tagged and the procedure described previously was followed to identify the breached element.

Subassemblies XY-27 and X429 were removed from the core after the termination of run 146B and X420A was removed in April prior to startup of run 148A. An FPS was placed in-core for run 148A, and the characteristics of gas release by direct recoil are displayed in the plot of slope. After run 148A was terminated, the FPS was removed from the core.

Other breaches in 1988 were similar to the ones described previously, except for

Table 5.3: Listing of breaches in 1988

	Date	Leaker	Fuel Type	Burnup	Breach Type
30	07-18	X421A?	metal	?	weld
31	08-01	X421A?	metal	?	weld
32	08-18	X482	metal 19Pu	high	fuel col.
33	09-15	X420B?	metal	?	weld
34	10-01	X420B?	metal	?	weld
35	10-18	X420B?	metal	?	weld
36	12-27	X482	metal 19Pu	high	fuel col.

the fuel column breach which occurred in the element in subassembly X482. The element in this subassembly contained 19%Pu; therefore, the same characteristic "percolating effect" as in the breach that occurred in X421A on October 11, 1987 was expected to be seen. Perhaps, this effect was not seen due to the presence of other breached elements in-core (i.e., X421A, and X420B).

Analysis of Breached Elements in 1989 and 1990

The breached elements occurring in 1989 and 1990 are listed in Table 5.4. Only the breached element in subassembly X420B, was not positively identified at the time of breach in 1989. A typical fuel column metal element breach was seen on January 26, 1989. Subassemblies X420B and X482 were then removed from the core after run 150B. Two breaches were detected during April of 1989 that showed typical characteristics of a metal weld failure and fuel column mixed-oxide breach. The gas released from the element in XC-1A did not appear in the plot, since its quantity was orders of magnitude smaller than the gas released from the element in X460

Table 5.4: Listing of breaches in 1989 and 1990

	Date	Leaker	Fuel Type	Burnup	Breach Type
37	01-26-89	X420B?	metal	?	fuel col.
38	03-06-89	XC-1A	metal 0Pu	low	weld
39	03-15-89	X460	oxide	high	fuel col.
40	10-31-89	X468 *	oxide	unirr.	plenum
41	11-21-89	X482A	metal 0Pu	high	fuel col.
42	01-26-90	X470 *	oxide	unirr.	plenum

(mixed-oxide).

During, April through October of 1989, the analysis of the FG data is not provided since the reactor was not at power. On Nov. 21, 1989, in X482A a metal element breached along the fuel column, which was indicated by a spike in the DN signal. The spike in the DN signal is rarely observed in a breach of metal elements; however, the DN spike displayed as a result of the breach in X482A can be attributed to the high burnup value and the alloy type (19%Pu).

After the termination of run 152C the subassembly X482A was removed from the core. For run 153A, four unirradiated mixed-oxide elements, manufactured with each containing a hole in the plenum region of the elements, were placed in-core in subassembly X470A. In this case, the characteristics of the storage and release of gas in mixed-oxide fuel is observed, since as gas is released from the fuel, it is able to escape to the core. The gas released during the month of February of 1990 was associated with diffusional release from X482A. This analysis of the event was based on the fact that the elements in X470 were not irradiated for a long enough period of time to be able to release gas. Eventually these elements reached burnup levels

that allowed for generation of gas void. The gas release from the void region of the mixed-oxide elements in X470, were observed in three occasions. These releases were caused by cracks that were formed in the fuel pins which in turn caused internal depressurization of the element. After the fuel structure was depressurized, there was no further release of stored gas; thus, the fuel cracks had sealed. The gas then built up in the central void again. This observation allowed us to learn the mechanism by which the FG is stored in the plenum region of the mixed-oxide element.

This concludes the discussion on the important fuel pin breach events that have occurred for the past five years. We used the knowledge gained from the analysis of this data to extract the heuristic rules and the rules generated by inductive learning that will be discussed in the next chapter.

CHAPTER 6. DERIVATION OF RULES FROM INDUCTIVE LEARNING

In this chapter, the development of the rule tree generated for FG analysis is discussed. The results of FG analysis, described in the previous chapter, were used to generate the rules by using inductive learning. Heuristic rules were also incorporated into the system. The description of how 1st Class Fusion [34] (the knowledge engineering product) is used and the techniques used for developing rules for FG analysis are given.

Basic Description of 1st Class Fusion

The material for this description is extracted from Reference [35]. The system is interfaced with the user by means of six screen "layers." The first screen, the file screen, is used to allow the user to retrieve an old KB, create a new one, print or export an existing KB shell out to DOS, quit, or view what Fusion calls a roadmap, which is described later.

The second screen of Fusion is called the definitions screen. In this screen, each column represents factors to be considered in solving the problem at hand, and the last column represents the results that can be determined from this KB. The definitions screen forces the user to think about what factors are important and what

results are possible, and it allows these factors and values to be added, deleted, and changed. Fusion also allows the user to associate a text, which typically contains descriptive information and embedded commands, for example, to run external programs or display help files. Fusion limits factor and value names to 11 characters, with no embedded spaces or punctuation.

The examples screen is where the factors and values are combined to give results. These examples are later used by Fusion to build a rule, which is in turn is used during consultation to determine a result. The options available to the user in the examples screen include adding, deleting, changing, moving, and replicating examples, each of which occupies one line. The last option, replication, is commonly used when a number of similar examples, that differ only slightly, are encountered. The maximum number of examples allowed in a KB is 255, but may be fewer depending on the memory of the system used. In adding an example, the factors are arranged horizontally on the screen. When a factor is highlighted, the possible values for that factor are arranged across the top of the screen and may be selected. Numerical data can be entered as values for some factors. Numeric quantities are treated either as upper bounds, lower bounds, or domains. In the first two cases, the maximum or minimum values are extracted, whereas in the third case regions are defined by considering the values entered in the examples. As an alternative to entering a specific value, a "don't care" value can be entered, meaning that the value of this factor is useless in deriving the result for this example. As each example is entered, Fusion tests for conflicts where the examples are contradictory. If a conflict is found the user is warned and the examples are highlighted.

In the next screen, methods screen, Fusion allows selection of a method for

deriving the rules. The major methods are: Optimize, Left-right, Exhaustive, Match, and Customize. When Optimize is chosen, the rules are generated so that factors that don't affect the selection of a result are eliminated and the number of questions that have to be asked to arrive at a result is minimized.

If it is desired to establish a particular sequence of questions, the Left-right method can be chosen. This option would be used mostly in cases where answers to some questions are difficult to obtain or costly to answer. This method used in conjunction with the Optimize method and the Definitions screen's ability, allows moving of the factors around to correspond to the sequence of questions that is desired to be asked. The Exhaustive method builds a rule in which all the factors appear on every path through the rule. It applies the factors in the same order they are on the Definitions screen. Examples are optional with this method.

The Match method does not build a rule. Instead, it causes a search when the advisor runs which matches the user's responses against the examples in the KB. The Match method is appropriate for problems with little pattern to them (and therefore not amenable to rules). It is also useful when the example data describe or diagnose conditions by positive example but there are no available counter-examples that describe when none of the results in the result column apply; thus, the KB would sometimes give an incorrect result.

Finally, the Customize method permits building and editing of the rules directly on the Rule screen (the screen described next). This method has two main uses: (1) rules can be built from scratch when data are in the form of rules or logic charts rather than examples, and (2) rules produced by any of the above methods can be edited.

The rule screen represents the definitions and examples entered previously as a tree of choices. Each node of this tree corresponds to a factor to be considered by Fusion in the course of a consultation. Results are found at the end of the tree. Each path in the tree corresponds to an example entered in the previous screen.

The next screen is the advisor screen. This screen is the user interface with the KB developed. The advisor screen in itself is composed of a set of screen. It starts with a preface screen, and displays a separate screen for each question it asks. The information given on each screen can be entered, otherwise Fusion default information for each screen is displayed. In other words, if the MEMO factor is entered, the text associated with this factor is used in the preface screen; otherwise, the user is directly asked the first question of the consultation.

Some of the attractive features of Fusion that are highlighted here are the chaining capabilities, weights and statistics considerations, providing reports and explanations, and commands that can be executed. Aside from the limits on the number of factors, results, and examples in a single KB, there are other reasons for using chaining of the rules. Chaining KBs makes debugging easier, since all the relationships are localized and easier to understand. For large collections of examples, a break up of the KB is necessary if a "Rule exceeds maximum size" error is encountered while using the Optimize or Left-right methods for generating the rules. And finally, it may be required for a factor to be replaced with several more detailed factors. Therefore, to avoid a major modification of the KB, chaining can be used.

A weight can be entered for each example used for developing the KB. Fusion uses the weights entered for each example and works up a set of statistics that takes account not only of weights, but of the number of examples, the frequency of results,

and the probability of a result. These statistics can be used in advice text to help back up a conclusion.

Fusion provides facilities for printing reports containing the text of every question asked during a consultation, and a listing of the possible answers, as well as the actual answer provided. Reports can either be generated individually or added to the end of existing report files. In addition to a reporting capability, Fusion also has an explanation facility which provides the users with reasons for arriving at a particular conclusion. Fusion helps out in this regard in several ways. First, the KB used by Fusion is pre-compiled, so that the developer can inspect the Rule screen and trace the result of a consultation at that moment. Second, Fusion can use the text associated with the individual results and examples to provide increased detail in the explanation.

Text associated with factors, values, results, and MEMOs can contain command statements. These statements consist of a command followed by the appropriate parameters. In particular, command statements allow execution of external programs written in Pascal, BASIC, or C, and a complete facility for parameter transfer is provided.

There are many other facilities provided by the 1st Class Fusion, and if one also has access to the 1st Class Fusion, Hyper Text, many more are added. In this section, the intent is to familiarize the reader with this software to be able to describe the development of the KB for FG analysis in later sections. However, before doing so, in the following section, the techniques used for developing the Optimized method and others are described.

The Inductive Inference Engine

The source for the material presented in this section is [36]. The inductive inference machinery is a simple mechanism for discovering a classification rule for a collection of objects belonging to classes. Each object must be described in terms of fixed attributes, each of which has its own set of possible attribute values. For example, “color” might be an attribute with a set of possible values, (red, green, blue).

Let us denote each example as an object and the result of each example as the class that other examples might be a member of. A classification rule in the form of a decision tree can be constructed for any such collection C of objects. The nodes of the tree are the attributes and the links between a parent and child node are the possible values of the parent node (attribute). The final nodes are then classes of disjoint sets of C 's.

In extreme cases, if C is empty then we associate it arbitrarily with any class. If all objects in C belong to the same class, then the decision tree is a leaf bearing that class name. Otherwise, C contains representatives of all classes; we select an attribute and partition C into disjoint sets C_1, C_2, \dots, C_n , where C_i contains those members of C that have the i^{th} value of the selected attribute. Each of these subcollections is then handled in turn by the same rule-forming strategy. The outcome is a tree in which each leaf carries a class name, and each interior node specifies an attribute to be tested with a branch corresponding to each possible value of that attribute.

To illustrate, the following example is presented, where three attributes are considered, “height” with values (tall, short), “hair” with values (dark, red, blond), and “eyes” with values (blue, brown), and where there are two classes denoted by “+”

Table 6.1: Examples and Classes

height	hair	eyes	class type
short	blond	blue	+
tall	blond	brown	-
tall	red	blue	+
short	dark	blue	-
tall	dark	blue	-
tall	blond	blue	+
tall	dark	brown	-
short	blond	brown	-

and “-”. In Table 6.1, a set of examples and their associated classes are listed.

If the second attribute is selected as the root of the decision tree, this results in the tree shown in Figure 6.1. The subcollections corresponding to the values ‘dark’ and ‘red’ contain objects of only a single class, and so require no further work. If we select the third attribute to test for the ‘blond’ branch, this yields the tree in Figure 6.2. Now all subcollections contain objects of one class, so we can replace each subcollection by the class name to get the decision tree shown in Figure 6.3.

An object is classified by starting at the root of the decision tree, finding the value of the tested attribute in the given object, taking the branch appropriate to that value, and continuing in the same fashion until a leaf is reached. This classification of a particular object may involve evaluating only a small number of the attributes depending on the length of the path from the root of the tree to the appropriate leaf. In the above example, the first step is always to inquire about the value of an object’s “hair” attribute. If this value is “dark” or “red” the object can be classified

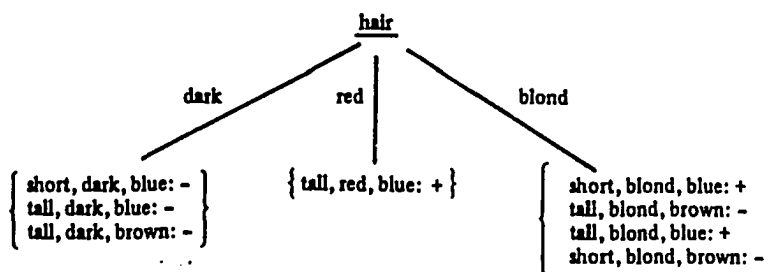


Figure 6.1: One-level decision tree

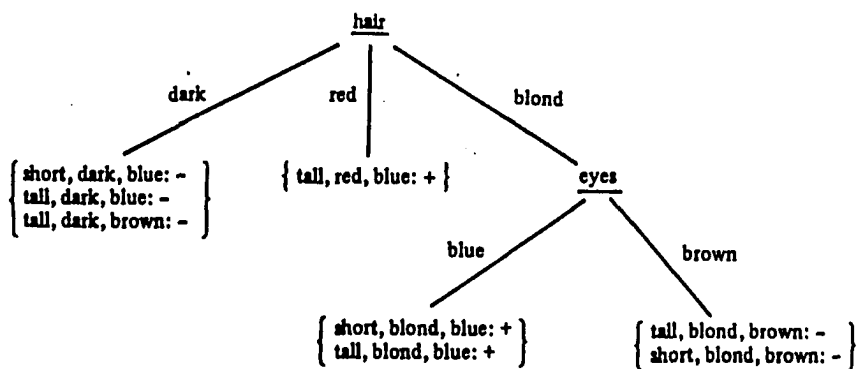


Figure 6.2: Two-level decision tree

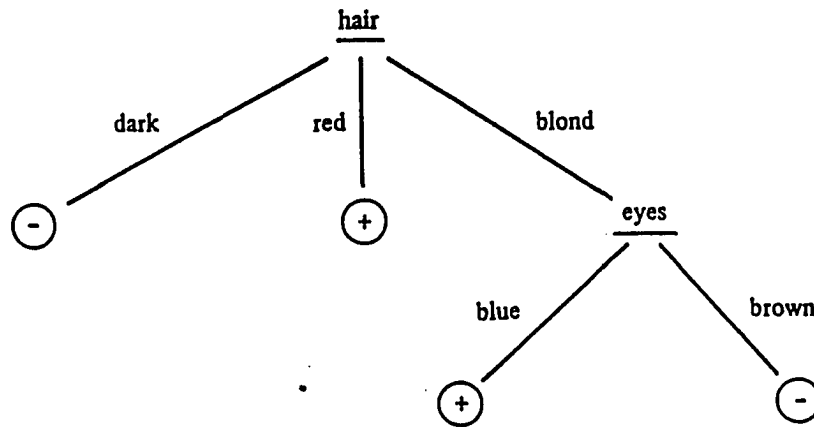


Figure 6.3: Decision tree with class names

immediately without looking at its other attributes. If the value is “blond” then its value of “eyes” must be determined before classifying it. Therefore, in none of the cases, is the value of the “height” attribute needed. This rule-forming procedure will always work provided that there are not two objects belonging to different classes but having identical values for each attribute; in such cases the attributes are inadequate for the classification task. Also, it is generally desirable to construct a tree that enables classification of the objects which were not used in its construction, so that concluding with classes with an empty set of examples is kept to a minimum.

So far, the selection process of the attribute used as the root of the decision tree was random. This is called the simple-minded algorithm, where the first attribute is selected for the root, the second attribute for the next level, and so on. This process is unreasonable, since the whole skill in this style of induction lies in selecting a useful attribute to test for a given collection of objects so that the final tree is in some sense minimal (total cost for searching the tree is minimized).

The technique used by Quinlan [36], called information-theoretic approach aimed at minimizing the expected number of tests to classify an object. A decision tree may be regarded as an information source that, given an object, generates a message which is the class of that object (“plus” or “minus”). The attribute selection part of this technique relies strongly on the plausible assumption that the complexity of the decision tree is related to the amount of information conveyed by this message. If the probability associated with “plus” and “minus” are p^+ and p^- , respectively, the expected information content of the message is,

$$-p^+ \log_2 p^+ - p^- \log_2 p^-.$$

The probabilities p can be approximated by the relative frequencies of the example in set C ; for example, p^+ becomes the proportion of objects in C with class “plus”. So, $M(C)$ is used to denote the calculation of the expected information content of a message from a decision tree for a set C of objects and for an empty set of C , this value is defined as zero, in order to establish the induction hypothesis.

Now, the possible choice of A is considered to be the next attribute to test. The partial decision tree is shown in Figure 6.4. The values A_i of attribute A are mutually exclusive, so the new expected information content becomes:

$$B(C, A) = (\text{probability that value of } A \text{ is } A_i) \times M(C_i),$$

where again, the probabilities can be replaced by the relative frequencies. Then the suggested choice of attribute to test next is that which provides the most information, in other words, the one for which

$$M(C) - B(C, A)$$

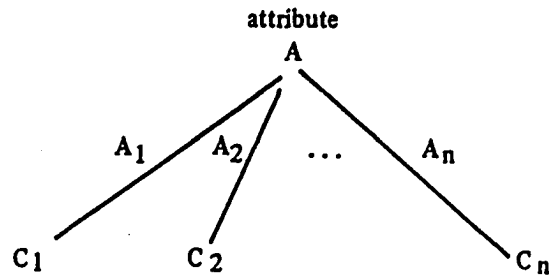


Figure 6.4: Partial decision tree

is a maximum.

In the example above, the value of $M(C)$ is calculated to be

$$M(C) = -3/8 \log_2 3/8 - 5/8 \log_2 5/8 = 0.954 \text{ bits},$$

since in the eight examples provided, three were in the “plus” and five in the “minus” classes. In Figure 6.5, the partial tree is depicted if the attribute chosen is “height”. Testing this attribute, the information still needed for a rule for the “tall” branch is:

$$-2/5 \log_2 2/5 - 3/5 \log_2 3/5 = 0.971 \text{ bits},$$

and information needed for the “short” branch is:

$$-1/3 \log_2 1/3 - 2/3 \log_2 2/3 = 0.918 \text{ bits}.$$

The expected information content is then calculated to be:

$$B(C, \text{height}) = 5/8 \times 0.971 + 3/8 \times 0.918 = 0.951 \text{ bits},$$

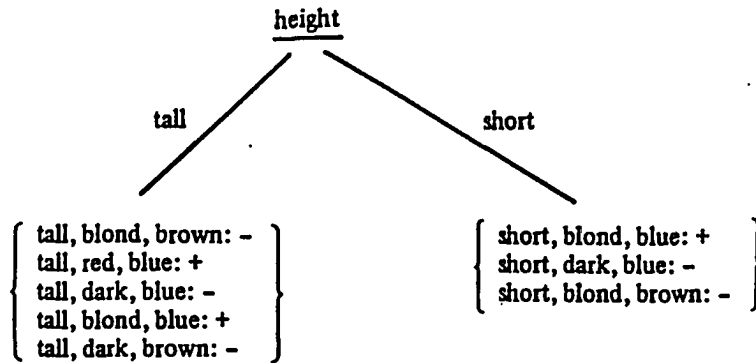


Figure 6.5: Binary attribute discrimination

and, the information gained by testing this attribute is:

$$0.954 - 0.951 = 0.003bits$$

which is negligible. Using the same technique, information gained by testing “eyes” and “hair” were calculated to be 0.347 and 0.454, respectively. Therefore, using “hair” as the root of the decision tree is cost efficient.

The description of the technique of inductive inference learning was given here to convey an understanding of how rules are generated using the Optimize method in 1st Class Fusion. This algorithm is used in the development of the learning part of the ES. This is referred to in more detail in the next chapter.

Derivation of Rules for FG Analysis

By using the inductive learning capability provided by 1st Class Fusion, a rule tree for FG analysis was generated. As was described in Section 6.1, 1st Class Fusion

uses a table of examples for generating the rule tree. Prior to setting up this table, a set of important factors and the associated values must be decided upon.

A set of important factors used for developing the rule tree for the FG analysis is provided in Figure 6.6. Following each factor, the values are listed. The maximum limit on the number of characters allowed by 1st Class Fusion for representing factors, values, and results is eleven characters. However, 1st Class Fusion permits entering a text for each of these items, where a clear description can be included. This text is also provided in Figure 6.6.

The values that describe the characteristics of the DN signal and slope were decided upon by categorizing the repeating behavior in these plots and formalizing them. For example, it is often observed that the value of slope suddenly increases to one and then gradually decreases. This characteristic was formalized as "sharp" slope. This was done by visual inspection of all of the plots included in the Appendix. For the sake of demonstrating the applicability of inductive learning in the development of this ES, it was justifiable to use this procedure; however, this process would ultimately have to be automated. This automation can be accomplished by using pattern recognition techniques. By using a pattern recognition technique, the behaviors are automatically categorized by matching patterns. When a new pattern is encountered, a new value is included for the associated factor.

The only piece of information extracted from the plot of the activity of FG isotopes was the increase in activity values due to the occurrence of a breach, even though more information is available in these plots, for example, the total volume of gas and the release rate. Access to this information becomes important when the indication of burnup level and alloy type of breach elements are included in the

DN@BK_BB [Is the DN signal at background level prior to the breach?]
yes
no

CHAN_IN_DN [Describe the behavior of the DN signal after breach:]
no [No indication of an increase in the DN signal.]
stepincr [Step increase.]
spikes [Spike with a wide width (more than a few hours).]
sharpspike [Spike with a short width (a few minutes).]

INCR_IN_DN [Enter the increase in the level of the DN signal.]

INCR_IN_135 [Enter the magnitude of largest spike in Xe135m activity.]

INCR_IN_87 [Enter the magnitude of largest spike in Kr87 activity.]

INCR_IN_133 [Enter the maximum level that Xe133 activity reached.]

SLOPE [Indicate the characteristics of the slope at time of breach?]
erratic [The slope shows erratic behavior, changes within minutes
between 0.2 to 0.8]
sharp [Sudden increase to one, then decreased similarly
to the activity of Xe133.]
grad_incr [Gradual increase and decrease to/from one
(displayed in a few days period).]
burp [Slope remains between 0.4 and 0.7.]

DIAGNOSTIC [The result is
]
met-fc [Metal Fuel Column Failure.]
met-dimple [Failure in the dimple region of a MK-II metal fuel.]
met-weld [Failure due to anomaly in the welding of the metal fuel.]
met-not-det [Failure in the metal fuel is not detected due to the
overriding effects of previously breached mixed-oxide
elements.]
ox-fc [Mixed-oxide breach along the fuel column.]
ox-fc-mul-b [Mixed-oxide failure in the fuel column region in the
presence of other mixed-oxide failed elements in-core.]
ox-plenum [Mixed-oxide failure in the plenum region.]
pre-b-oxide [Mixed-oxide element that had already breached in the fuel column
region is present in-core.]

Figure 6.6: A listing of the definitions, values, and final results

diagnosis. As was mentioned in the analysis of the FG data, we refrained from providing this diagnostic capability due to the lack of analytical methods that allow us to model the FG storage and release, unavailability of a theoretical model that allows for subtracting the effects of the previous breaches, and lack of information on identification of the breach elements, i.e., unavailability of TG information on some breaches.

Also included in Figure 6.6 are the final results. These results or diagnoses are the different types of breaches that occurred in the past five years. The table of examples that was used to generate the rule tree is depicted in Figure 6.7 and the rule tree is shown in Figure 6.8. The number associated with each example in Figure 6.7 is the same as the number allocated to each breach in the tables provided in the previous chapter, with the exception of examples 42 and 43. Both of these examples were extracted from the last breach in 1990, since several distinct sudden gas releases occurred from the element in subassembly X470.

The procedure followed for deriving the factors, and the associated values given in Figure 6.6, was as follows. At first, a complete set of factors and the associated values was conservatively defined. In other words, all possible factors in the diagnostics were included. Then, for each of the breaches occurring in the past five years, an example was set up by extracting the value of each factor from the plots in the Appendix. As a result, a comprehensive table of examples was formed. The rule tree was then generated by using the Optimized method. When the Optimized method is used, 1st Class Fusion provides a listing of factors that were not used in generating the rule tree. By using this list, the unimportant factors were eliminated from the table of examples and the second rule tree was generated. It was expected that the second

Examples for Knowledge Base FGAS

6:59 pm 10/23/1990

DIAGNOSTIC	weight	SLOPE	INCR_IN_133	INCR_IN_87	INCR_IN_135	INCR_IN_DN	CHAN_IN_DN	DN#BK_BB
erratic	1.00	ox-fc	*	200.	100.	600.	spikes	1: yes
erratic	1.00	ox-fc-mul-b	5000.	110.	1000.	stepincr	2: no	
erratic	1.00	ox-fc-mul-b	5000.	90.	1000.	stepincr	3: no	
burp	1.00	met-not-det	0.	0.	0.	no	4: no	
erratic	1.00	ox-fc-mul-b	20000.	400.	1000.	stepincr	5: no	
erratic	1.00	ox-fc	20000.	200.	1500.	spikes	6: yes	
erratic	1.00	ox-fc	*	1000.	2500.	spikes	7: yes	
burp	1.00	pre-b-oxide	1000.	50.	2000.	stepincr	8: yes	
erratic	1.00	ox-fc-mul-b	20000.	200.	1000.	stepincr	9: no	
erratic	1.00	met-fc	5000.	140.	0.	no	10: no	
grad_incr	1.00	met-dimple	20000.	150.	0.	no	11: no	
grad_incr	1.00	met-dimple	10000.	120.	0.	no	12: no	
erratic	1.00	ox-fc	25000.	750.	0.	no	13: no	
burp	1.00	pre-b-oxide	*	0.	1000.	stepincr	14: yes	
erratic	1.00	ox-fc	13000.	1400.	600.	spikes	15: yes	
sharp	1.00	met-weld	800.	0.	0.	no	16: no	
sharp	1.00	met-weld	2000.	0.	0.	no	17: no	
erratic	1.00	ox-fc	3000.	500.	1500.	stepincr	18: yes	
grad_incr	1.00	met-dimple	7000.	10.	0.	no	19: yes	
grad_incr	1.00	met-dimple	3750.0	0.	0.	no	20: yes	
erratic	1.00	met-fc	800.	15.	0.	no	21: yes	
erratic	1.00	met-fc	2200.0	20.	0.	no	22: yes	
sharp	1.00	met-weld	2200.	10.	0.	no	23: yes	
erratic	1.00	met-fc	2000.	50.	0.	no	24: yes	
sharp	1.00	met-weld	1000.	7.5	0.	no	25: yes	
sharp	1.00	met-weld	2000.	6.0	0.	no	26: yes	
erratic	1.00	met-fc	5000.	100.	0.	no	27: yes	
sharp	1.00	met-weld	3000.	40.	0.	no	28: yes	
erratic	1.00	met-fc	3000.	50.	0.	no	29: yes	
sharp	1.00	met-weld	7500.0	7.5	0.	no	30: yes	
grad_incr	1.00	met-weld	7500.	7.	0.	no	31: yes	
erratic	1.00	met-fc	6000.	500.	0.	no	32: yes	
sharp	1.00	met-weld	15000.	50.0	0.	no	33: yes	
sharp	1.00	met-weld	10000.	0.	0.	no	34: yes	
sharp	1.00	met-weld	10000.	15.	0.	no	35: yes	
erratic	1.00	met-fc	8000.	300.	500.	sharpspike	36: yes	
erratic	1.00	met-fc	5000.	125.	0.	no	37: yes	
sharp	1.00	met-weld	3000.0	25.	0.	no	38: yes	
erratic	1.00	ox-fc	35000.	150.	2000.	spikes	39: yes	
burp	1.00	ox-plenum	300.	0.	600.	sharpspike	40: yes	
erratic	1.00	met-fc	3500.	750.0	200.0	sharpspike	41: yes	
sharp	1.00	ox-plenum	5000.	100.	0.	no	42: yes	
sharp	1.00	ox-plenum	15000.	400.	75.	no	43: yes	

Figure 6.7: The listing of examples

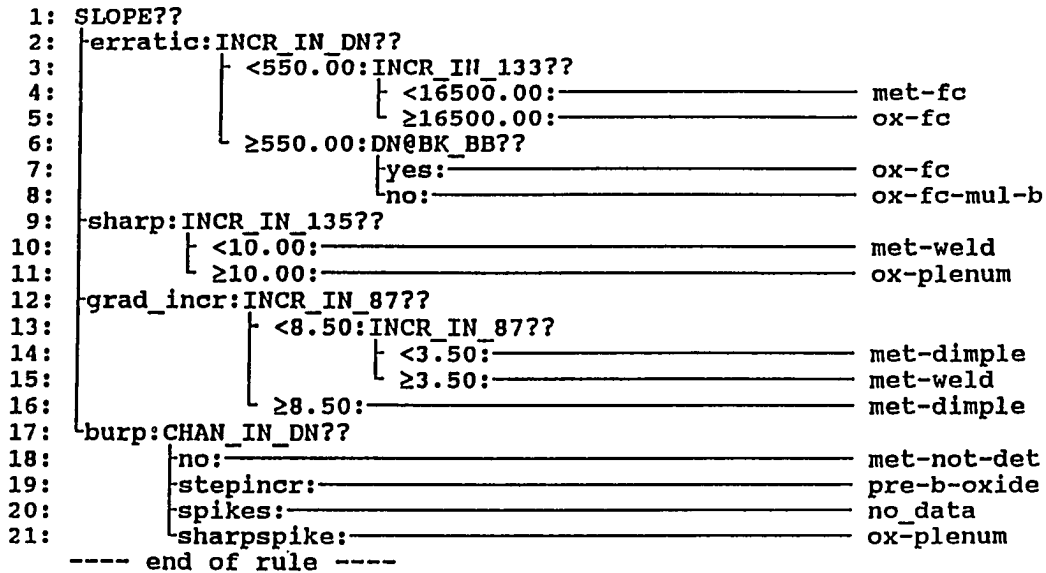


Figure 6.8: The rule tree for FG analysis

rule tree would be identical to the first one. The comprehensive list of factors initially given to Fusion includes the following effects: (a) the characteristics of the cumulative activity, such as a step increase in the cumulative activity, the value of the slope of the cumulative activity prior to the breach, (b) the level of the FG activity prior to the breach, (c) whether the short half-life gas was seen at the same time or after the long half-life gas appeared (heuristic rule), and (d) whether or not the increase in DN signal lagged the appearance of the FG and by how long (heuristic rule). However, after generating the rule tree by using the Optimize method, it was realized that these factors were unimportant in deriving conclusions from the rule tree, and therefore they were eliminated from the example table.

In the description of the inductive learning technique that was utilized to develop the Optimize method, it was indicated that the factor contributing the most in the diagnosis appears as the root of the rule tree. The characteristics of the slope was

the root which indicates the importance of this factor in the FG analysis.

To test the rule tree, the query option provided by Fusion was used for diagnosing all breaches that occurred since May of 1986. All breaches were diagnosed correctly, as was expected. Of course, since only the information from all breaches that occurred in the past five years was included in the example table for developing the rule tree, we were not able to test this rule tree by diagnosing a breach that was not included in the example table.

Figures, 6.9, 6.10, 6.11, and 6.12 provide examples of reports of the query sessions for diagnosing breach 1, 9, 22, and 34 that are specified in Tables 5.1, 5.2, and 5.3.

The Customized method was then used to incorporate the heuristic rules that were used during the analysis of data, since, in attempting to enter them as factors, they were found to be unimportant. However, since the rules generated by inductive learning were few in number and conclusive on their own, including the heuristic rules only introduced inefficiencies.

Indicate the characteristics of the slope at time of breach?

- * The slope shows erratic behavior, changes within minutes
- * Sudden increase to one, then decreased similarly
- * Gradual increase and decrease to/from one
- * Slope remains between 0.4 and 0.7.

==> The slope shows erratic behavior, changes within minutes

Enter the increase in the level of the DN signal.

* Enter a number:

==> 600.00

Is the DN signal at background level prior to the breach?

- * yes
- * no

==> yes

The result is

Mixed-oxide breach along the fuel column.

End of Session Report for Knowledge Base FGAS

7:30 pm 10/23/1990

Figure 6.9: Query session report of breach 1

Indicate the characteristics of the slope at time of breach?

- * The slope shows erratic behavior, changes within minutes
- * Sudden increase to one, then decreased similarly
- * Gradual increase and decrease to/from one
- * Slope remains between 0.4 and 0.7.

==> The slope shows erratic behavior, changes within minutes

Enter the increase in the level of the DN signal.

* Enter a number:

==> 1000.00

Is the DN signal at background level prior to the breach?

- * yes
- * no

==> no

The result is

Mixed-oxide failure in the fuel column region in the presence of other mixed-oxide failed elements in-core.

End of Session Report for Knowledge Base FGAS

7:32 pm 10/23/1990

Figure 6.10: Query session report of breach 9

Indicate the characteristics of the slope at time of breach?

- * The slope shows erratic behavior, changes within minutes
- * Sudden increase to one, then decreased similarly
- * Gradual increase and decrease to/from one
- * Slope remains between 0.4 and 0.7.

==> The slope shows erratic behavior, changes within minutes

Enter the increase in the level of the DN signal.

* Enter a number:

==> 0.00

Enter the maximum level that Xe133 activity reached.

* Enter a number:

==> 2200.00

The result is

Metal Fuel Column Failure.

End of Session Report for Knowledge Base EGAS

7:33 pm 10/23/1990

Figure 6.11: Query session report of breach 22

Indicate the characteristics of the slope at time of breach?

- * The slope shows erratic behavior, changes within minutes.
- * Sudden increase to one, then decreased similarly
- * Gradual increase and decrease to/from one
- * Slope remains between 0.4 and 0.7.

==> Sudden increase to one, then decreased similarly

Enter the magnitude of largest spike in Xe135m activity.

* Enter a number:

==> 0.00

The result is

Failure due to anomaly in the welding of the metal fuel.

End of Session Report for Knowledge Base FGAS

7:34 pm 10/23/1990

Figure 6.12: Query session report of breach 34

CHAPTER 7. DESIGN OF THE EXPERT SYSTEM AND SUGGESTIONS FOR FUTURE DIRECTION

In analyzing the FG data of EBR-II, more complexities were encountered than in analyzing the FG data of a commercial power plant, since EBR-II is an experimental facility where various fuel types are always used in-core, whereas, in commercial power plants only a few different types of fuel are utilized. Therefore, a database for storing information on the fuel elements that have been used in EBR-II is included in the design of the ES. The data on the fuel loading of EBR-II (including information on burnup, and alloy type) would allow for a more comprehensive diagnosis of failed fuel elements; in particular, information on alloy types and burnup levels can be included in the diagnosis.

Although the experience gained from the FG analysis of the data gathered for the past five years was invaluable, it was not sufficient for generating a comprehensive rule tree, simply because of the unavailability of some of the diagnostic tools (e.g., extent of the breach from DN analysis, the FG volume released from the breached element, a true calculation of cumulative activity where the loss effects are taken into account, etc.) or due to the deficiencies of some diagnostic tools (e.g., TG analysis). Due to lack of tag information (either caused by not tagging or by an untimely purging of the cover gas), more than a third of the breaches that occurred since May

of 1986 were not identified at the time of breach by TG analysis. However, in the design of the ES all of the diagnostic tools developed to this date were included. Also, the capability of the addition of new diagnostic tools in the KB of this ES must be provided in an automated fashion.

The diagnostic tools and the rule-based component is depicted in Figure 7.1. Since, this ES will be used on a real-time basis, the analytical components (i.e., GIRAFFE, and FG analysis) have also to be run on a real-time basis. Whereas POLYFAIL (used for TG analysis) has to be executed only when a new breach occurs or when the tag ratios have to be modified for correcting for burnup and buildup of tag isotopes. GIRAFFE, relatively requires the longest computation time, has been modified so that it can be run on a parallel processing system. These analytical components have been developed in FORTRAN and are modified to be run on a real-time basis. The characteristics of the output of some of these diagnostic tools must be analyzed by pattern recognition techniques, as was referred to earlier on.

It was demonstrated that the inductive learning technique is efficient in diagnosing breaches in EBR-II. However, similar to the analytical components, the ES must be able to include, (a) a new event, (b) a new diagnostic tool, or (c) a new pattern that is detected in the output of one of the diagnostic tools, on a real-time basis.

Finally, to summarize the design features of the ES for fuel failure diagnosis in EBR-II developed by using an inductive learning inference engine, the following items must be taken into consideration.

- A database must be available so that the ES is capable of extracting information on the breached element.
- The execution of the analytical components which provide the diagnostic tools

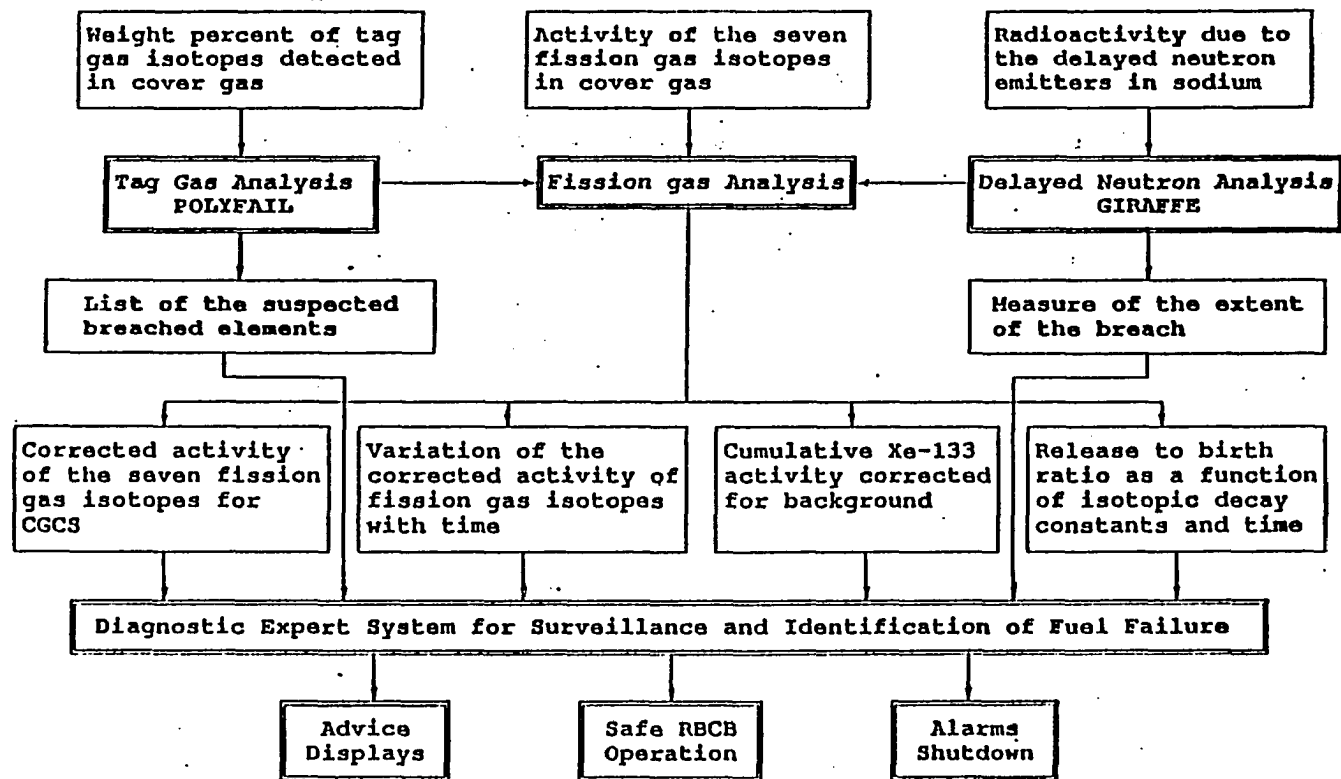


Figure 7.1: Schematic of the design of the expert system

must be controlled in an automated fashion by the ES.

- The characteristics of the output of some diagnostic tools must be analyzed by pattern recognition techniques.
- When a new event (a new breach type) is detected, a new result must be included in the example table, and the rule tree must be regenerated.
- When a breach occurs that is within the domain of the expertise of the KB (more simply, when similar breach types are already included in the example table) a new example must be entered into the example table and the rules regenerated.
- When a new diagnostic tool becomes available new factors must be introduced to the example table and the rule tree regenerated.
- When a new pattern or piece of information is identified, it must be included in the example table by introducing a new value for the factor associated with the diagnostic tool and a new rule tree must be regenerated.
- All of the above items must be performed in an automated fashion, with human interaction minimized.

CHAPTER 8. ACKNOWLEDGMENTS

I wish to express my deepest gratitude to my major professor, Dr. R. A. Danofsky and my supervisors at Argonne, Dr. K. C. Gross and Dr. J. D. B. Lambert, not only for their constant advice, help and guidance during the performance of this research, but also for their kindness, friendship, and encouragement. I would like to extend my appreciation to Dr. W. N. Beck at Argonne. He shared his invaluable expertise in fuel diagnostics throughout many hours of bull sessions. Drs. J. H. Bottcher and R. V. Strain at Argonne also greatly contributed to the analysis of the FG data. Also, everyone's help in bureaucratic and personal affairs made the completion of this project easier.

I express my gratitude to Drs. B. I. Spinrad, M. S. Wechsler, D. M. Roberts, G. M. Prahbu, C. W. Wright for being a member of my graduate committee, with special thanks for Dr. Spinrad for his guidance and friendship. I wish him and Lois a healthy and happy life at Oregon.

I am indebted to Argonne for financial support during my Laboratory Graduate term and to Iowa State University during my Research Assistant term. In this regard, the interest and financial support of the DOE and PNC is appreciated.

Dr. Mostafa and Hajar Mahmoudian Mikaili (my parents) played a great role in my education. Also, Carol (my other mom), Arman, Afshin (my brothers), and

Duane (my other dad), gave me a great deal of encouragement. I would like to give special thanks to them.

During my stay at Argonne (away from home) Jordi Roglans-Ribas, Anna Pla-Delmau, Serhat, and Gonenc Alten, helped and encouraged me a great deal. I would like extend my thanks to them.

And finally, there are no words that express my appreciation for Linda, Niyazi, Sasha, Bachany, Peeshi and Ike for their love.

I would like to dedicate this work to Ruth Anderson. Cancer took her life but the pleasant memories that we have of her will never leave us.

BIBLIOGRAPHY

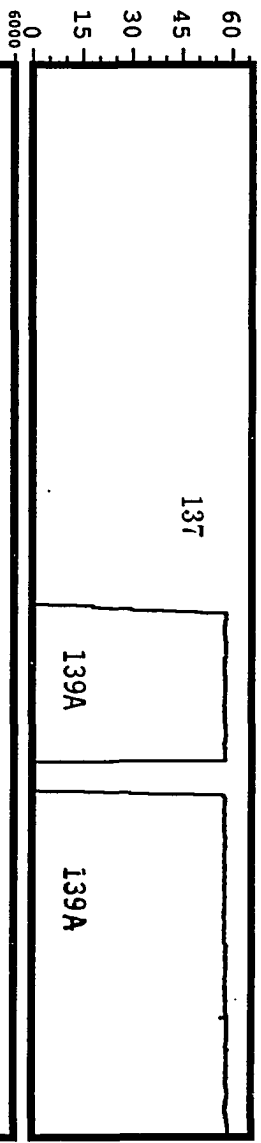
- [1] "EBR-II Since 1964," Intra-Laboratory Report, Argonne National Lab. (West), 1987 (Unpublished).
- [2] A. Barr and E. A. Feigenbaum, "The Handbook of Artificial Intelligence," vol. 1, California: Addison-Wesley, 1981.
- [3] J. R. Anderson, "Cognitive Psychology and Its Implications," 2nd ed. New York: W. H. Freeman and Company, 1985.
- [4] P. H. Winston, "Artificial Intelligence," New York: Addison-Wesley, 1979.
- [5] G. F. Luger and W. A. Stubblefield, "Artificial Intelligence and the Design of Expert Systems," Redwood City, California: The Benjamin/Cummings Publishing Company, Inc., 1989.
- [6] P. Harmon and D. King, "Expert Systems. Artificial Intelligence in Business," New York: John Wiley and Sons, 1985.
- [7] B. R. T. Frost, "Nuclear Fuel Elements," New York: Pergamon Press, 1982.
- [8] R. V. Strain, Personal Communication, Argonne Natl. Lab. (1990).
- [9] S. Nomura and K. C. Gross, "Method for Subtracting the Effect of CGCS Operation from DAS Data," Intra-Laboratory Memo, Argonne National Lab., 1984 (Unpublished).
- [10] J. D. B. Lambert, B. Y. So, F. S. Kirn, J. R. Armstrong, E. R. Ebersole, and M. T. Laug, "Recent Improvements in Identifying Fission Product sources in the Experimental Breeder Reactor II," Nucl. Technol. 39, 279 (1978).

- [11] P. B. Henault, G. J. Bernstein, L. F. Coleman, E. R. Ebersole, W. J. Larson, and R. R. Smith, "Identification of Failed Fuel Elements by Xenon Tag," *Trans. Am. Nucl. Soc.* 12, 102 (1969).
- [12] B. Y. C. So, J. D. B. Lambert, E. R. Ebersole, and M. T. Laug, "Change in Xenon Tag Composition with Exposure-EBR-II Experience," *Trans. Am. Nucl. Soc.* 23, 473 (1976).
- [13] J. H. Opelka and D. Meneghetti, "Burnup and Production of Xenon Tag Isotopes in Fueled Experiments in EBR-II," *Trans. Am. Nucl. Soc.* 22, 622 (1975).
- [14] B. Y. So, J. D. B. Lambert, and E. R. Ebersole, "Fractional Releases of Xenon Tag and Fission Gas from Defective Element in EBR-II," *Trans. Am. Nucl. Soc.* 23, 472 (1976).
- [15] G. L. Hofman and D. L. Johnson, "Semiempirical Correlations for Fission Gas Release from Fast Reactor Fuels," *Trans. Am. Nucl. Soc.* 21, 179 (1975).
- [16] J. D. B. Lambert, B. Y. C. So, and M. T. Laug, "Use of ($^{131}\text{Xe}/^{134}\text{Xe}$) Ratio to Distinguish Between Defective Uranium and Plutonium-Bearing Elements in EBR-II," *Trans. Am. Nucl. Soc.* 23, 474 (1976).
- [17] B. Y. C. So and G. W. Stauffer, "MIXTAG-A Code to Identify the Components of a Mixture of Xenon Tags," *Trans. Am. Nucl. Soc.* 26, 522 (1977).
- [18] G. S. Brunson, "Monitoring Fission Gas in EBR-II by High-Resolution Gamma Spectrometry," *Nucl. Tech.* 25, 533-571 (1974).
- [19] K. C. Gross and C. Passerello, "Barycentric-Coordinates Technique for Identification of Simultaneous Fuel Failures with Gas Tagging," *Nucl. Science and Engineering*, 75, 1-11 (1980).
- [20] K. C. Gross, Personal Communication, Argonne Natl. Lab. (1990).
- [21] R. P. Omberg and R. E. Schenter, *Trans. Am. Nucl. Soc.* 16, 215 (1973).
- [22] K. C. Gross and R. V. Strain, "Delayed Neutron Signal Characterization in Fast Reactor," *Nucl. Science and Engineering*, 76, 163-174 (1980).
- [23] K. C. Gross and R. V. Strain, "Apparatus for and Method of Monitoring for Breached Fuel Elements," United States Patent, 4,415,524 (1983).
- [24] K. C. Gross and L. K. Polley, "Investigation of Nonrecoil Fission-Product Release Phenomena Using Multifrequency Source-Perturbation Experiments in EBR-II," *Trans. Am. Nucl. Soc.* 52, 643 (1986).

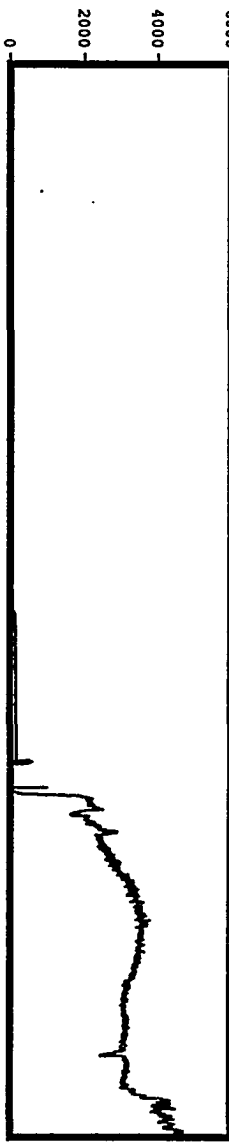
- [25] K. C. Gross and R. V. Strain, "System for On-Line Characterization of Delayed-Neutron Signals," *Trans. Am. Nucl. Soc.* 47 (1984).
- [26] S. Nomura, K. C. Gross, and J. D. B. Lambert, "Breached Pin Diagnosis by Fission-gas Analysis in the EBR-II Program," *Proc. of Inter. Conf. on Reliable Fuels for Liquid Metal Reactor*, *Am. Nucl. Soc.*, pp. 6-105 to 6-119, Tucson, Ar., Sept. 1986.
- [27] G. F. Knoll, "Radiation Detection and Measurement," New York: John Wiley and Sons, 1979.
- [28] D. R. Olander, "Fundamental Aspects of Nuclear Reactor Fuel Elements," TID-26711-p1, (1967), p. 287.
- [29] G. Hoffman, et al., "Fuel Failure Detection and Location in Fast Breeder Reactor," *Proc. of IAEA Specialist Meeting on Fuel Failure Detection and Location in LMFBR*, Karlsruhe, KfK3203 IWGFR/38 (1982), p. 215.
- [30] I. Fujii, et al.: *J. Brit. Nucl. Energy Soc.*, 13, 403 (1974).
- [31] N. Mitsutsuka, Y. Gohshi, and H. Feuerstein, "Method for Determining De-gassing Constant of Xenon in Liquid Sodium," *J. of Nucl. Science and Tech.*, Vol. 15, No. 9, 678-684 (1978).
- [32] T. D. Claar, "Determination of the Primary Argon Gas Loss Rate from Cover Gas Activity Measurements: Attachment 1," *Inter-Lab. Report, ANL-West*, (Unpublished).
- [33] R. G. Nobles, "Determination of the Primary Argon Gas Loss Rate from Argon Make-Up, Inventory, and Floating Head Tank Dynamics: Attachment 2," *Inter-Lab. Report, ANL-West*, (Unpublished).
- [34] 1st Class Fusion. Wayland, Mass.: 1st Class Expert Systems, Inc., 1989.
- [35] A. Lane, "1st-Class Fusion, A Knowledge Engineering Product," *the Artificial Intelligence Magazine for Personal Computing*, May/June 1989.
- [36] J. R. Quinlan, "Machine Learning: An Artificial Intelligence Approach", ed. R. Michalski, J. Carbonell, and, T. Mitchell, Morgan Kaufmann Publishers, Los Altos, CA, 1980.

**APPENDIX PLOTS OF FG ANALYSIS FROM MAY OF 1986 TO
APRIL OF 1990**

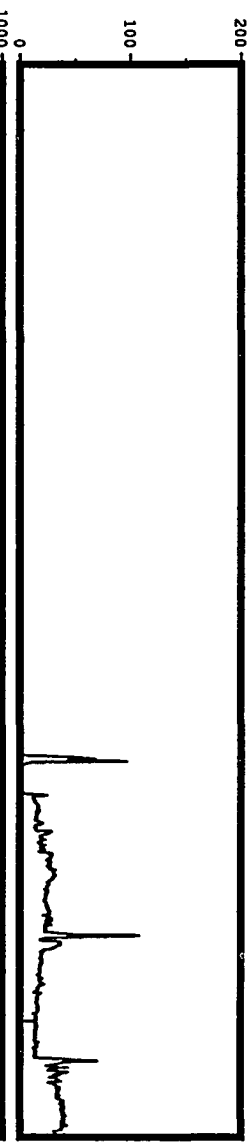
POWER, MWt



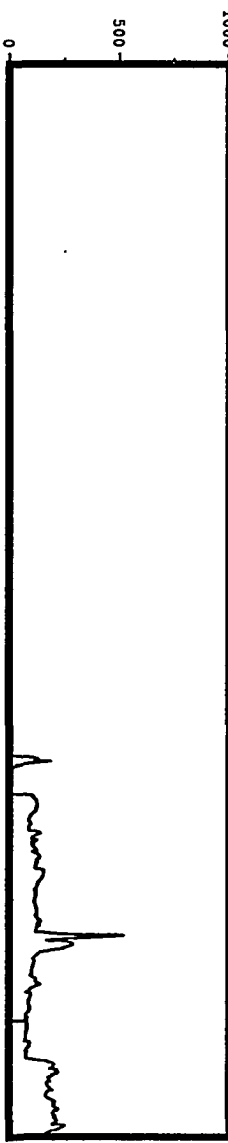
DN, cps



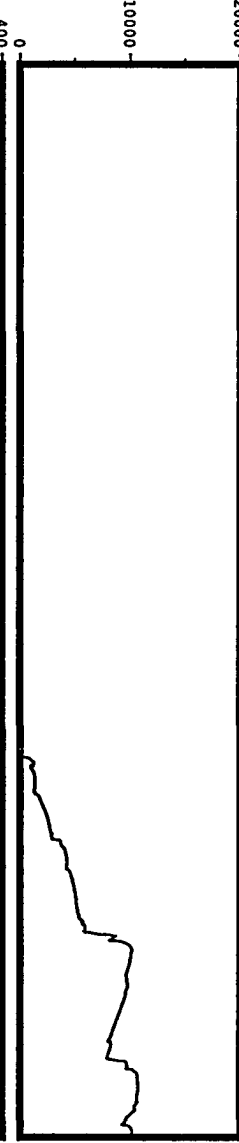
XE-135M, nCi/ml



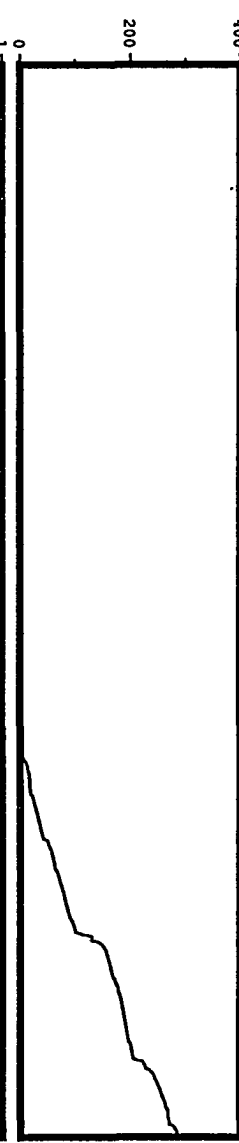
KR-87, nCi/ml



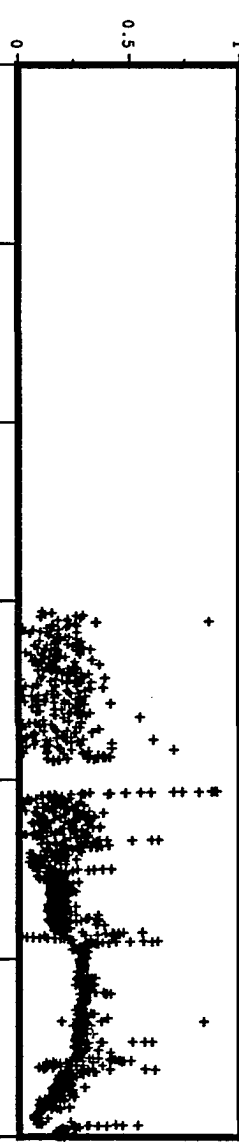
XE-133, nCi/ml



CUM XE-133, Ci

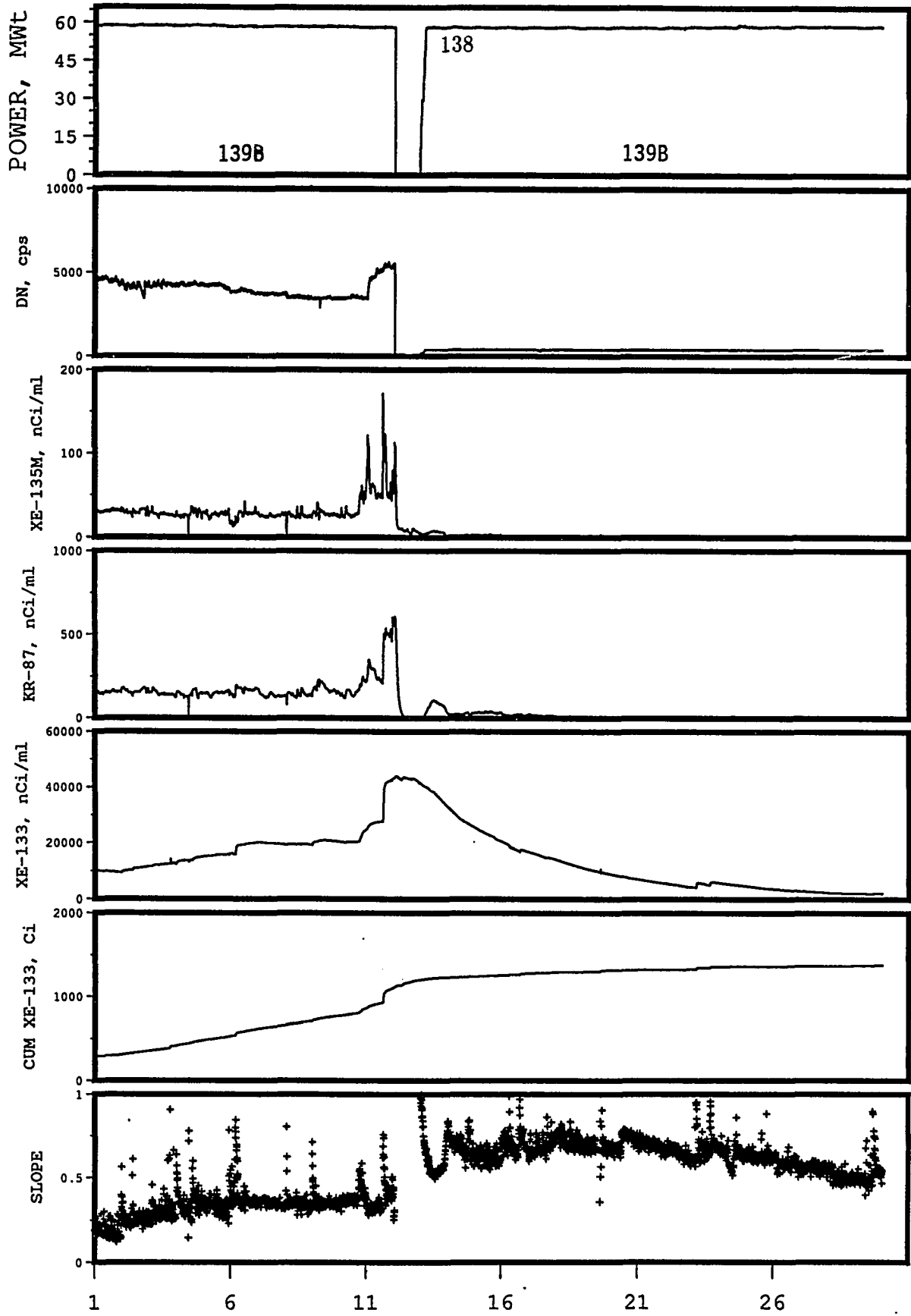


SLOPE



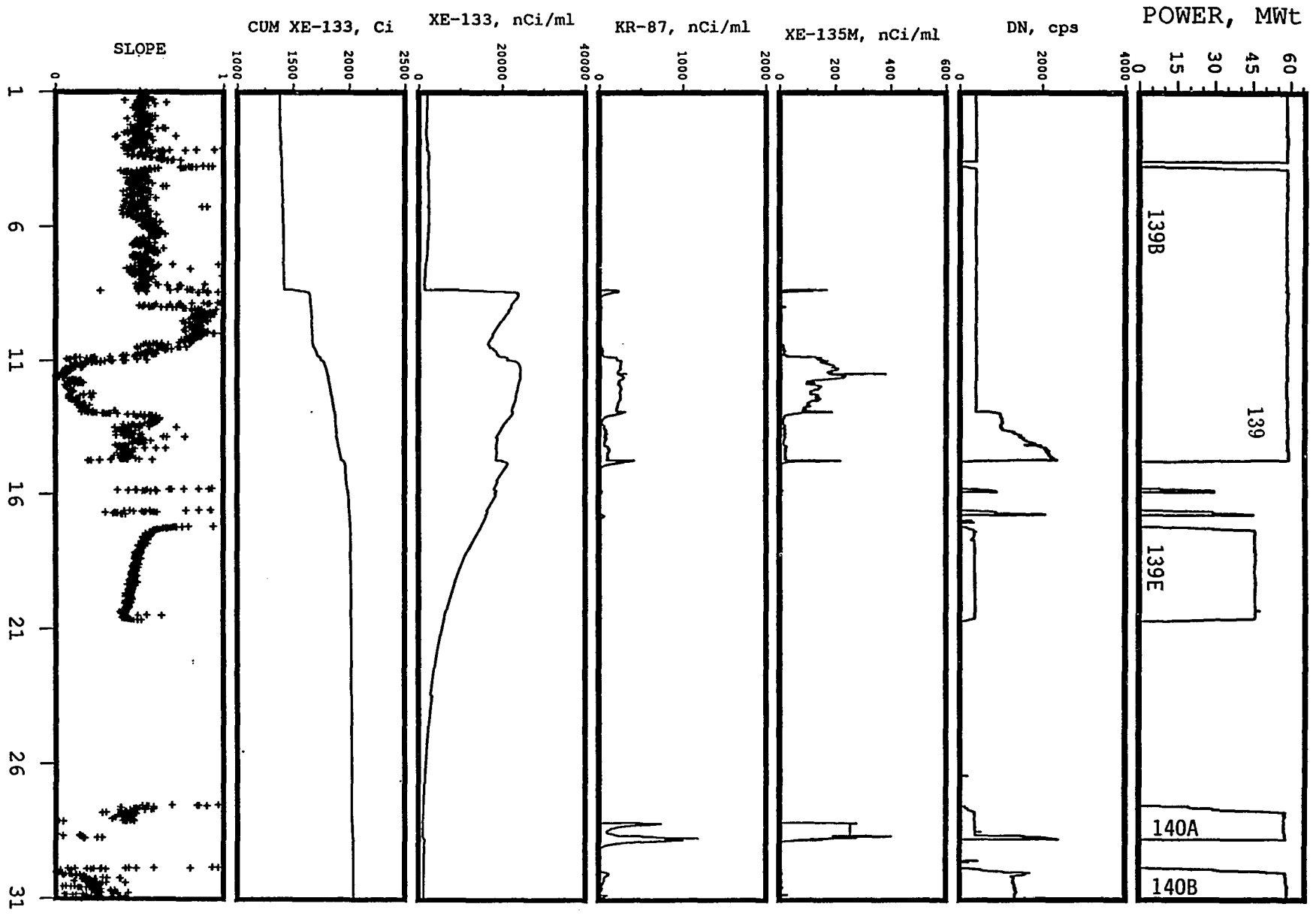
1 6 11 16 21 26 31

MAY
1986



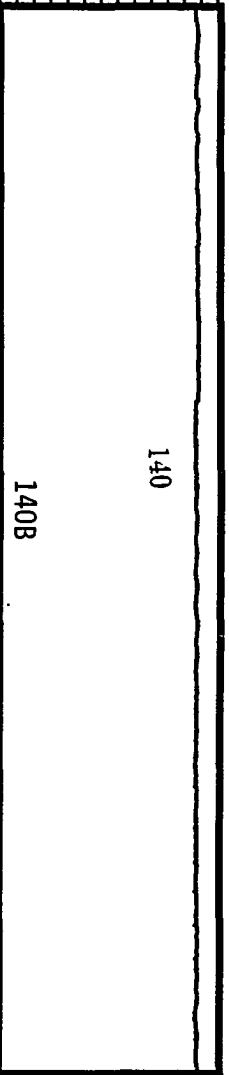
JUNE
1986

JULY
1986



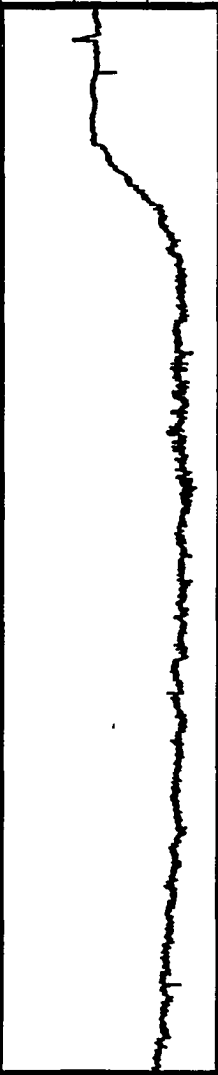
POWER, MWt

60
45
30
15
0



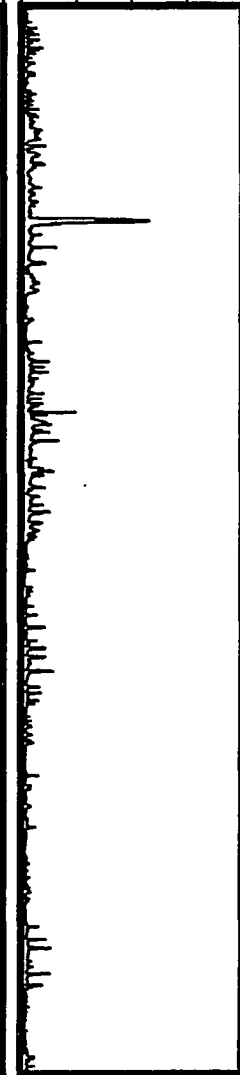
DN, cps

1000
2000
3000
0



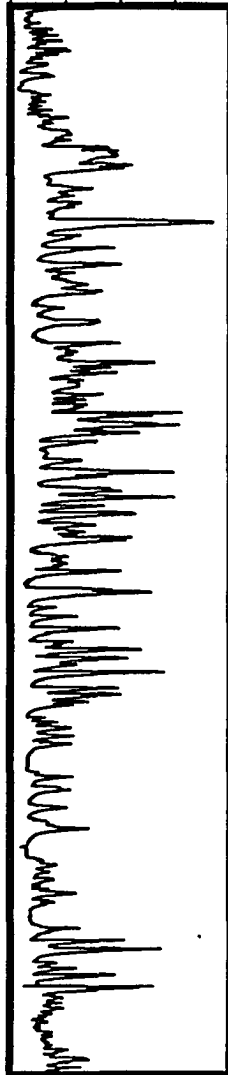
XE-135M, nCi/ml

400
200
0



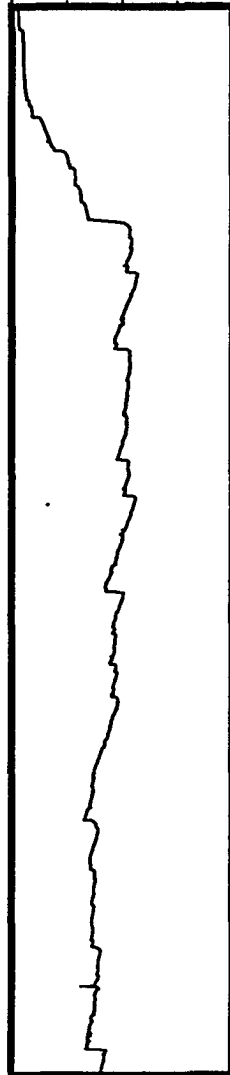
KR-87, nCi/ml

200
0



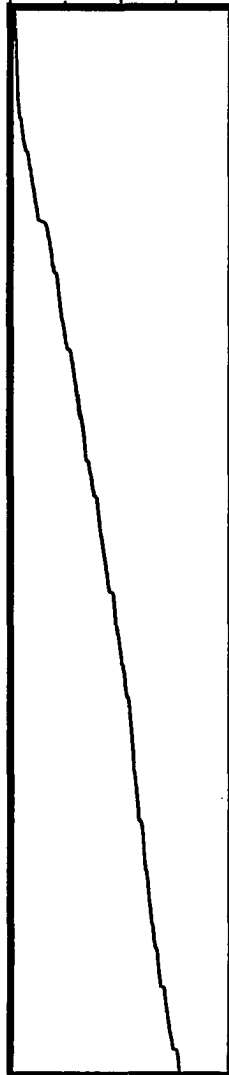
XE-133, nCi/ml

40000
20000
0



CUM XE-133, Ci

2000
3000
4000
0



SLOPE

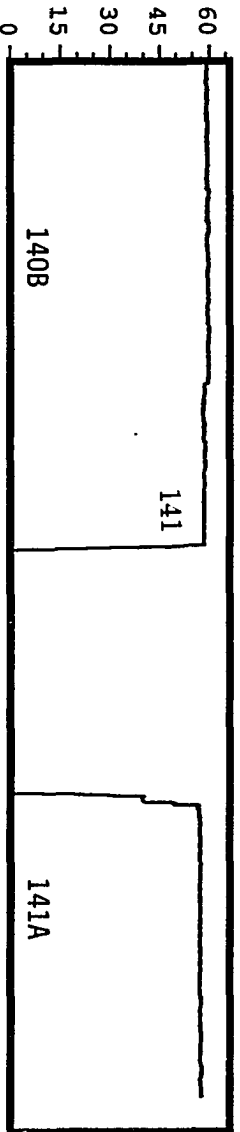
0.5
1
0



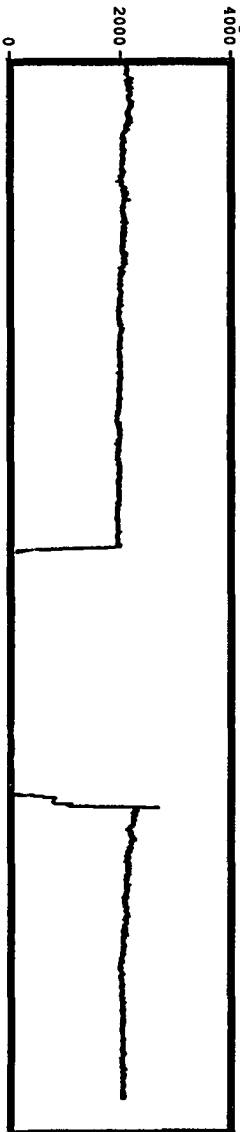
1 6 11 16 21 26 31

AUGUST
1986

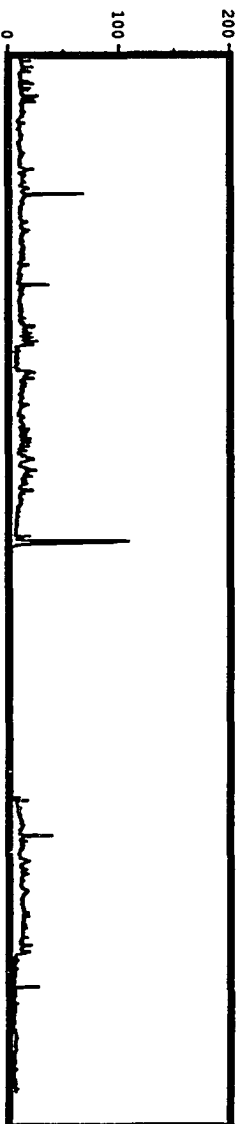
POWER, MWt



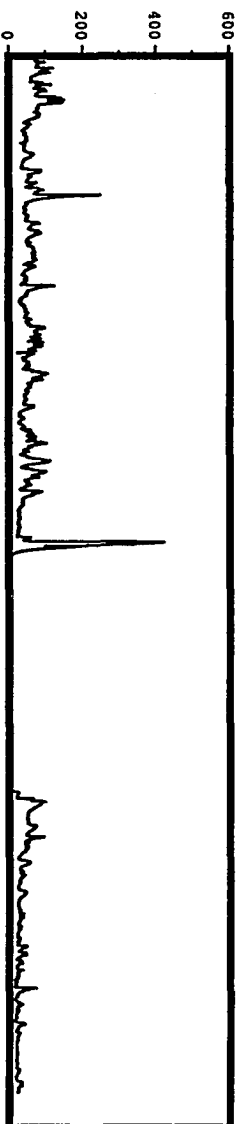
DN, cps



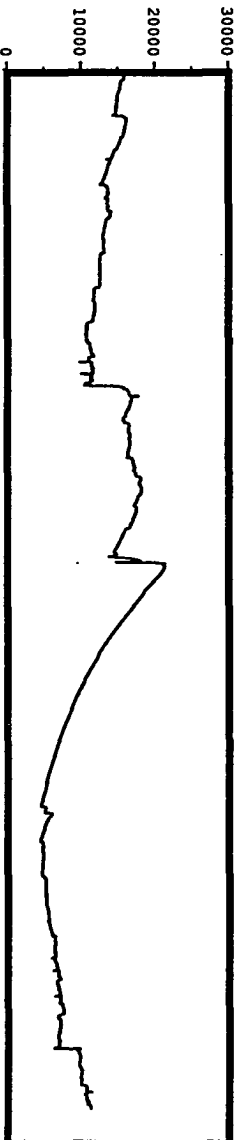
XE-135M, nCi/ml



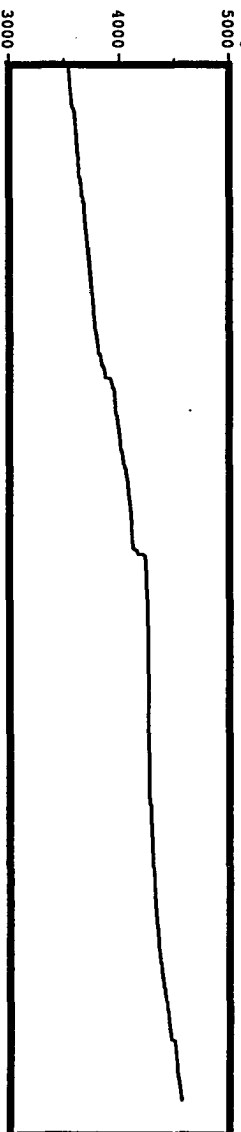
KR-87, nCi/ml



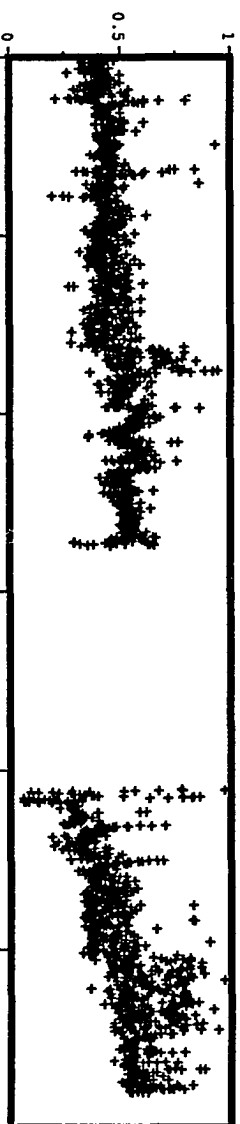
XE-133, nCi/ml



CUM XE-133, Ci



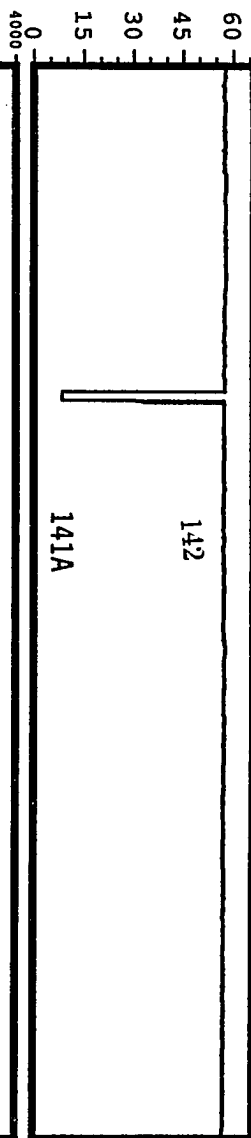
SLOPE



1 6 11 16 21 26

SEPTEMBER 1986

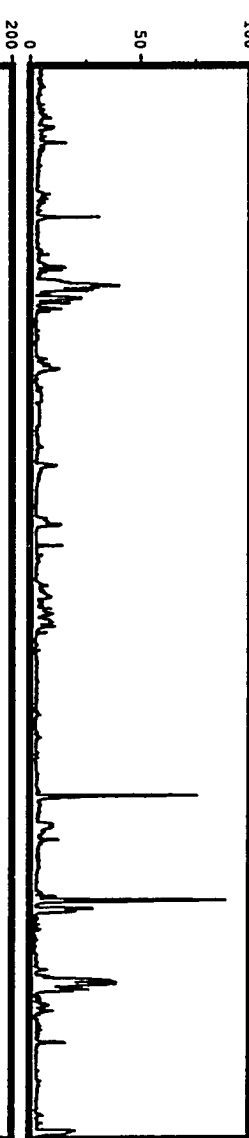
POWER, MWt



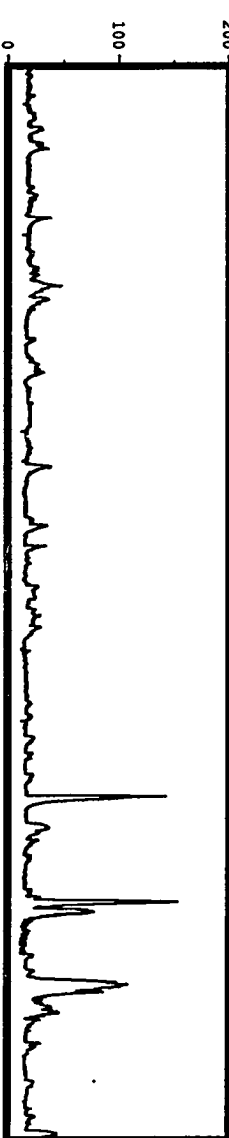
DN, cps



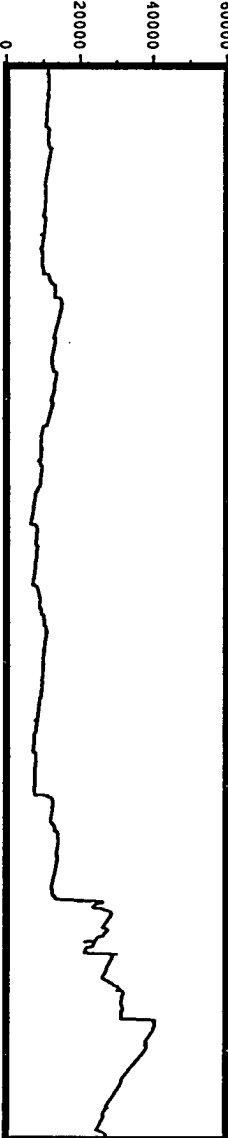
XE-135M, nCi/ml



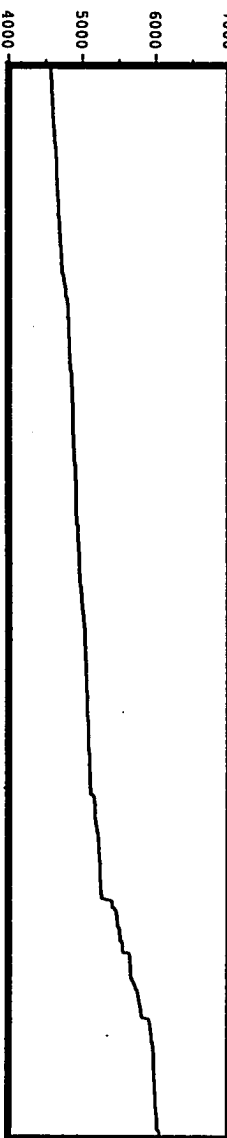
KR-87, nCi/ml



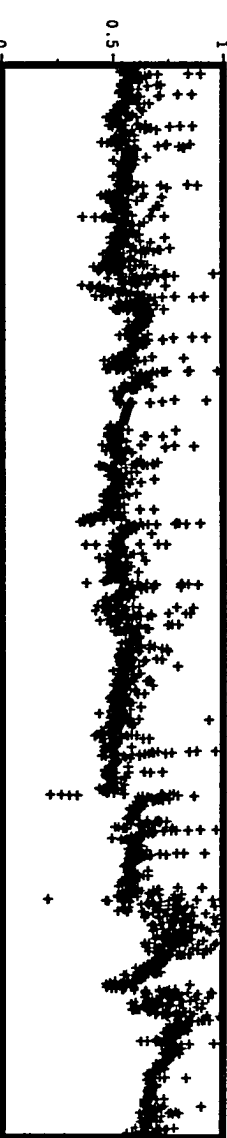
XE-133, nCi/ml



CUM XE-133, Ci



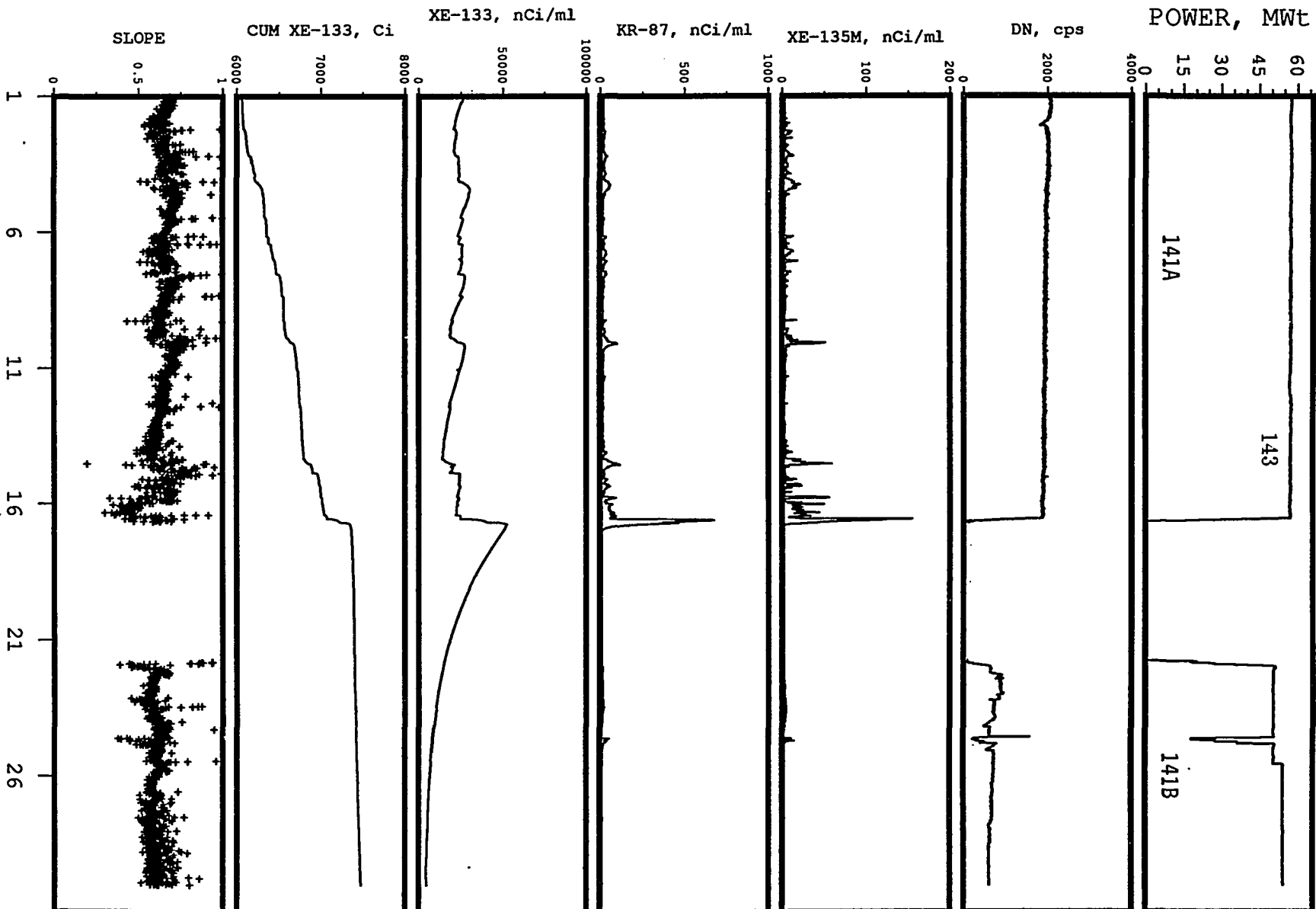
SLOPE

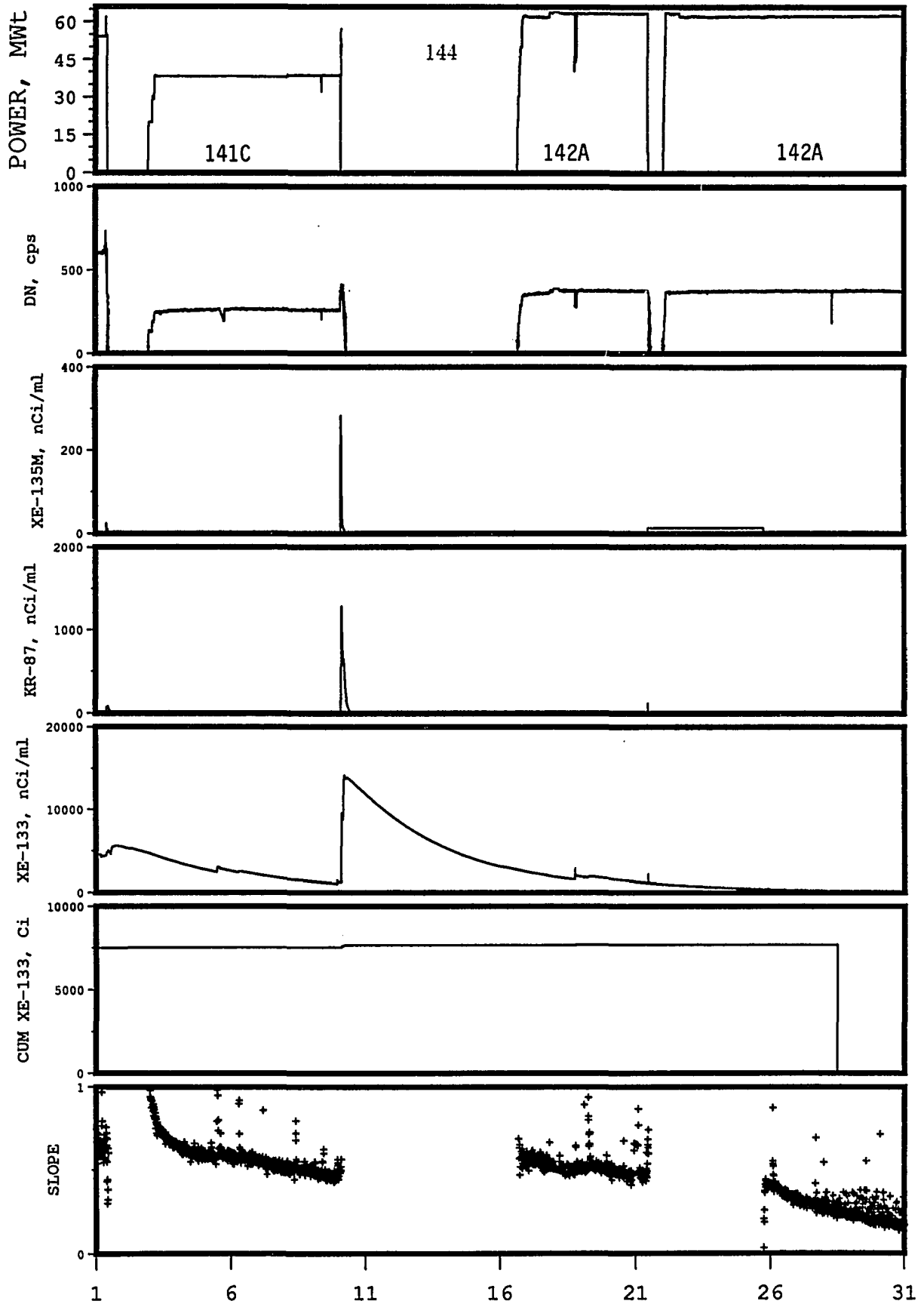


1 6 11 16 21 26 31

OCTOBER
1986

NOVEMBER
1986

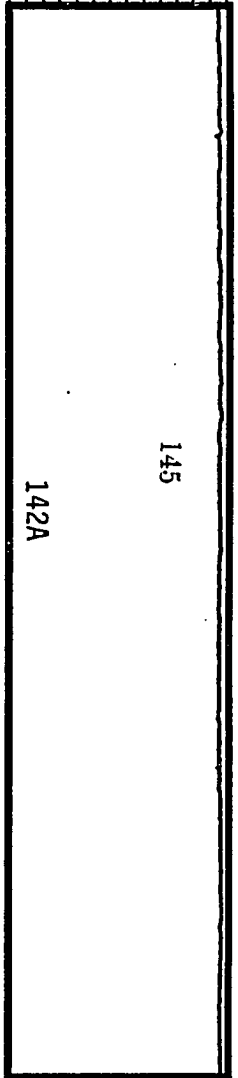




DECEMBER
1986

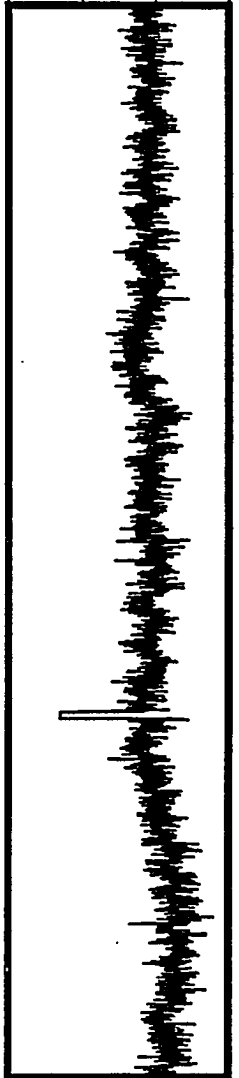
POWER, MWt

60
45
30
15
0



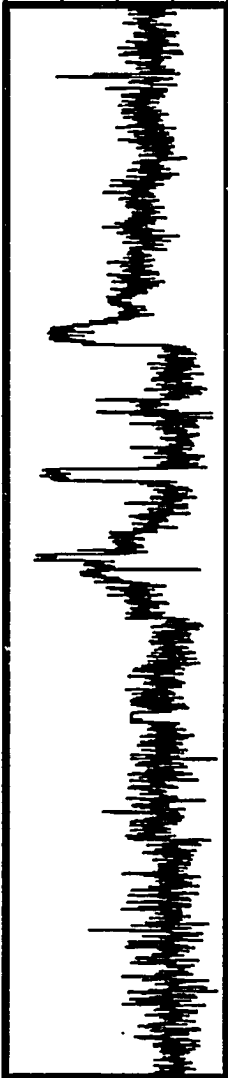
DN, cps

340
320
300
280
260
240
220
200
180
160
140
120
100
80
60
40
20
0



XE-135M, nCi/ml

0.4
0.2
0.0



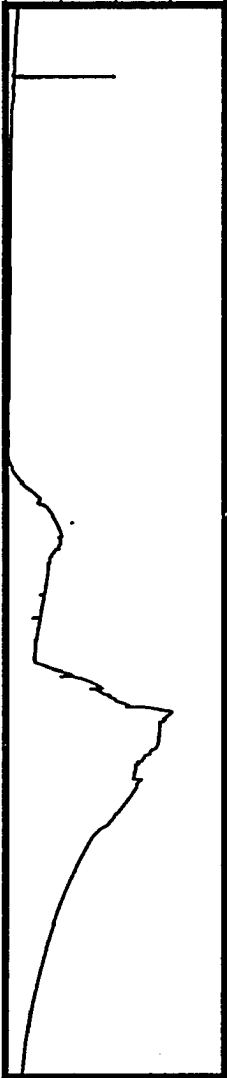
KR-87, nCi/ml

2
4
6



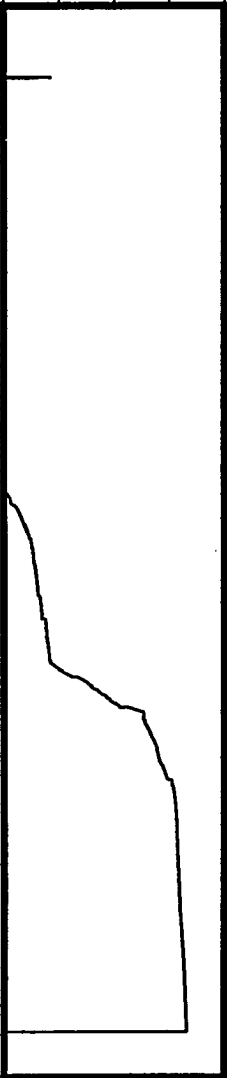
XE-133, nCi/ml

0
1000
2000



CUM XE-133, Ci

0
20
40



SLOPE

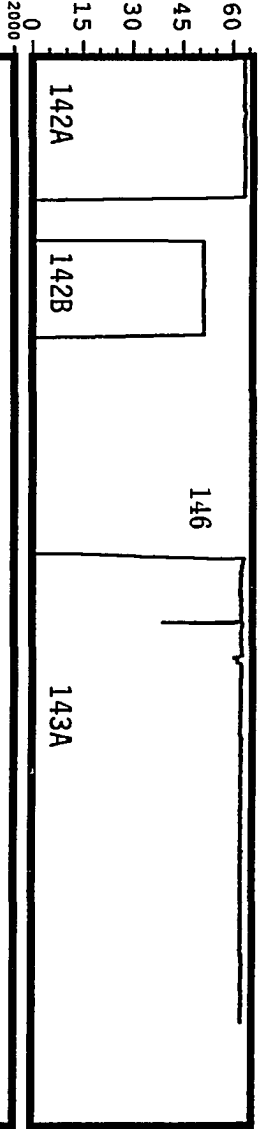
0
1



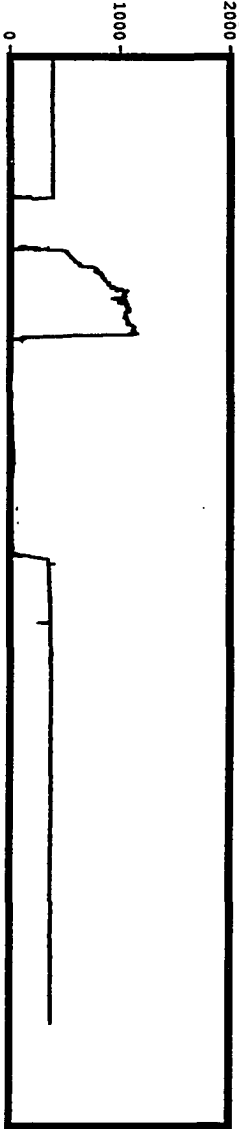
1
6
11
16
21
26
31

JANUARY
1987

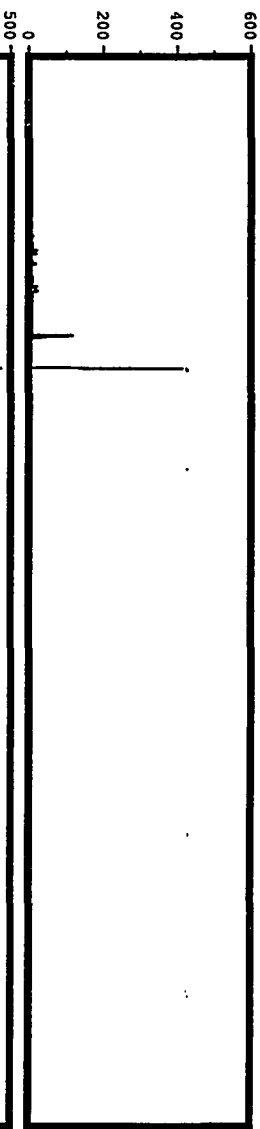
POWER, MWt



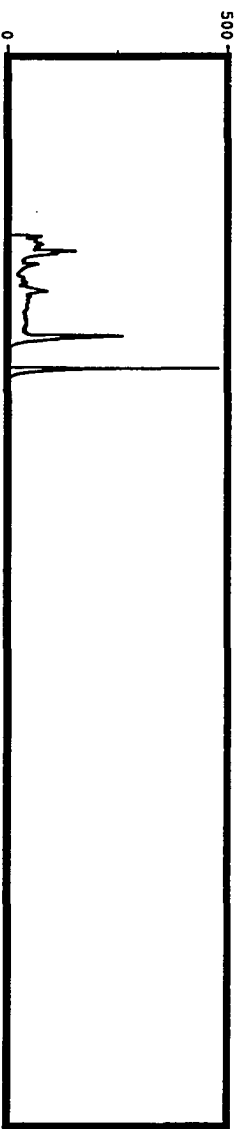
DN, cps



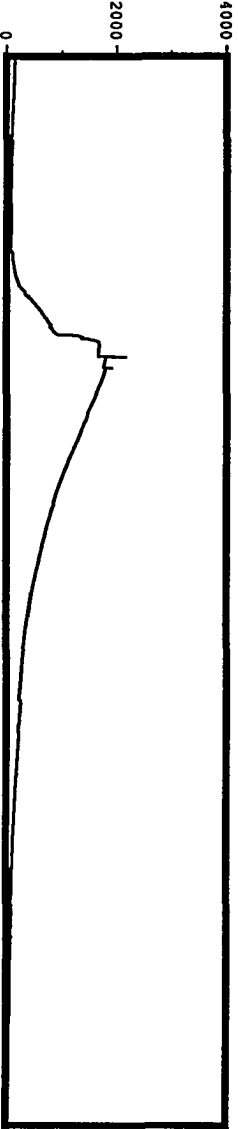
XE-135M, nCi/ml



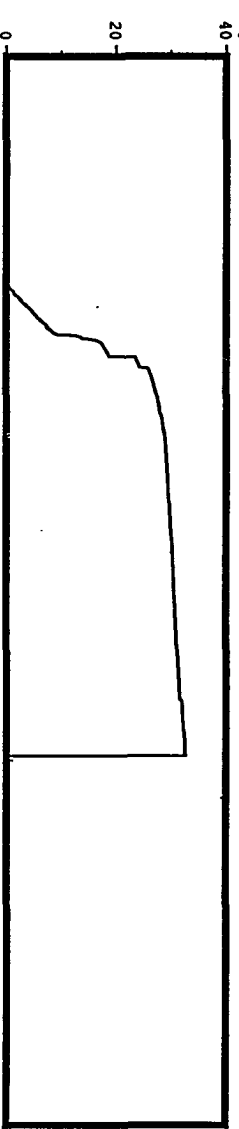
KR-87, nCi/ml



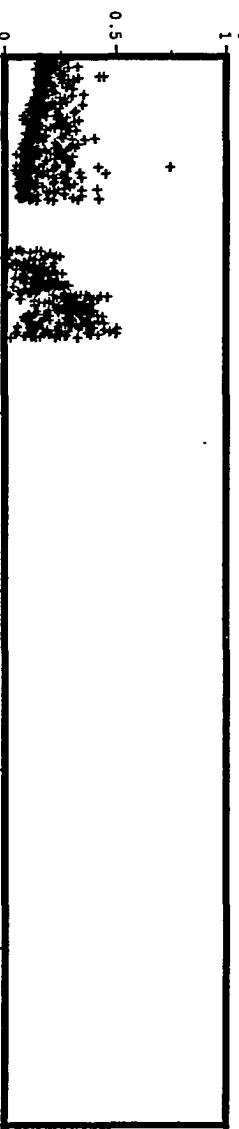
XE-133, nCi/ml



CUM XE-133, Ci



SLOPE

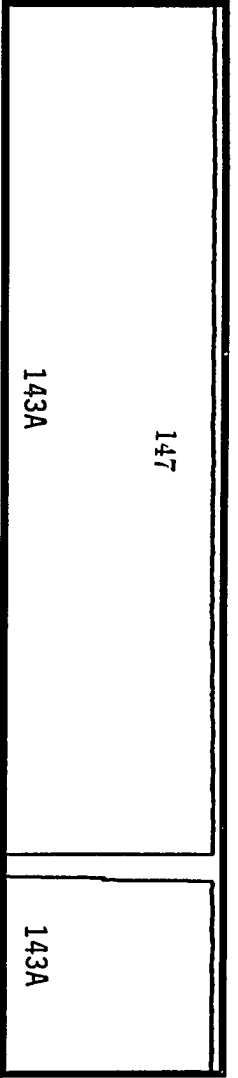


1 6 11 16 21 26

FEBRUARY 1987

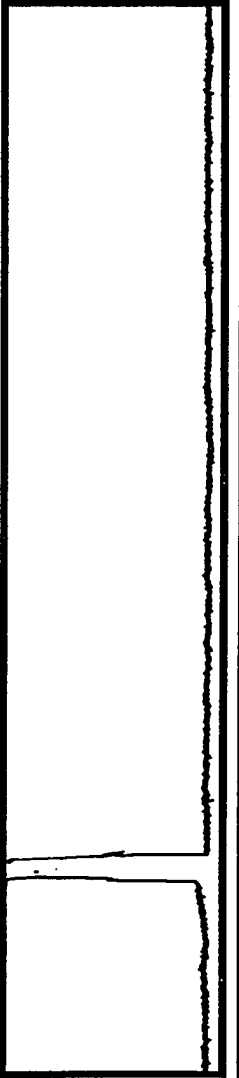
POWER, MWt

60
45
30
15
0



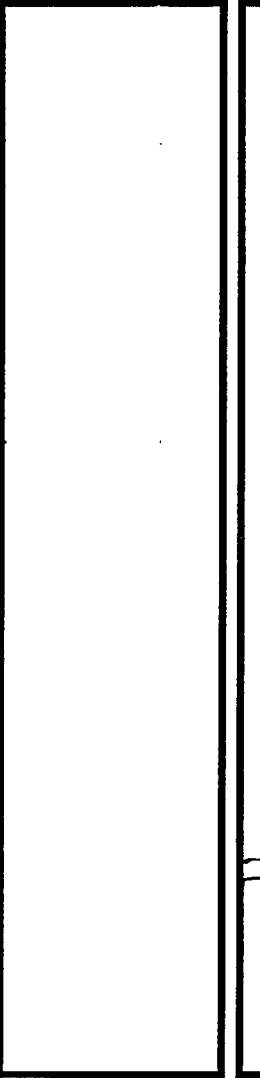
DN, cps

400
200
0



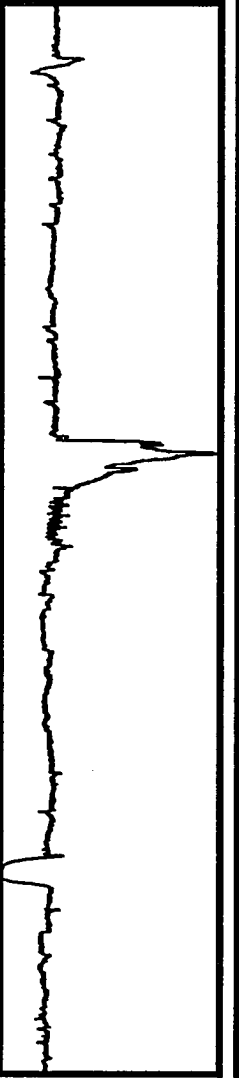
XE-135M, nCi/ml

600
400
200
0



KR-87, nCi/ml

10
0



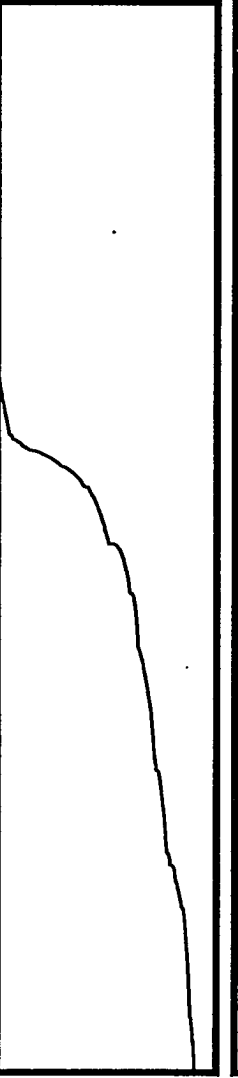
XE-133, nCi/ml

10000
5000
0



CUM XE-133, Ci

200
100
0



SLOPE

1
0.5
0



1 6 11 16 21 26 31

MARCH
1987

POWER, MWt

60
45
30
15
0

143A

148

DN, cps

0

0.4

XE-135M, nCi/ml

0.0

0.2

KR-87, nCi/ml

0

2

XE-133, nCi/ml

0

4000

CUM XE-133, Ci

0

200

SLOPE

0.5

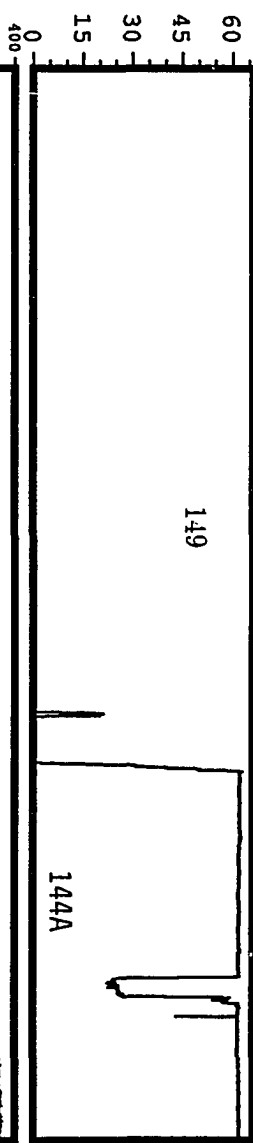
1

1 6 11 16 21 26

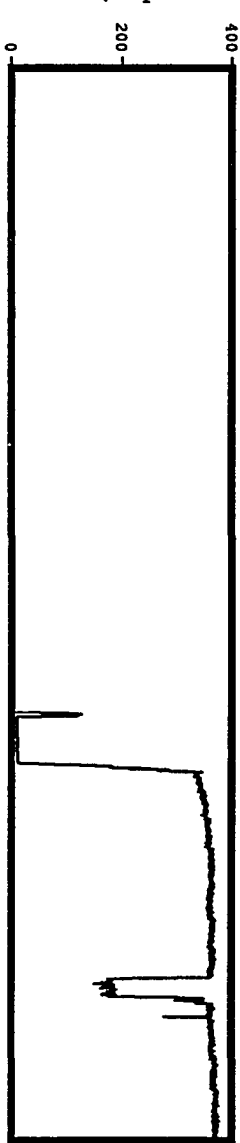


APRIL
1987

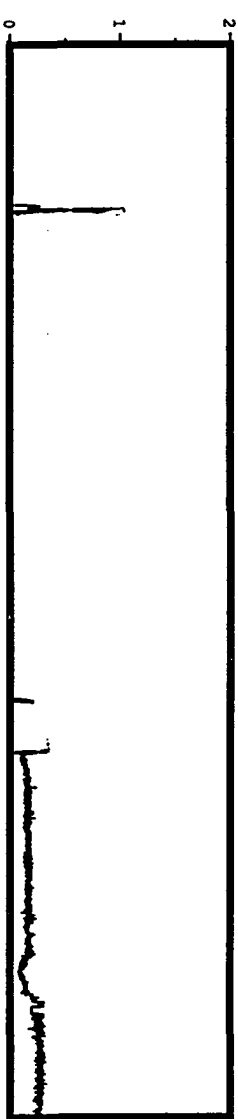
POWER, MWt



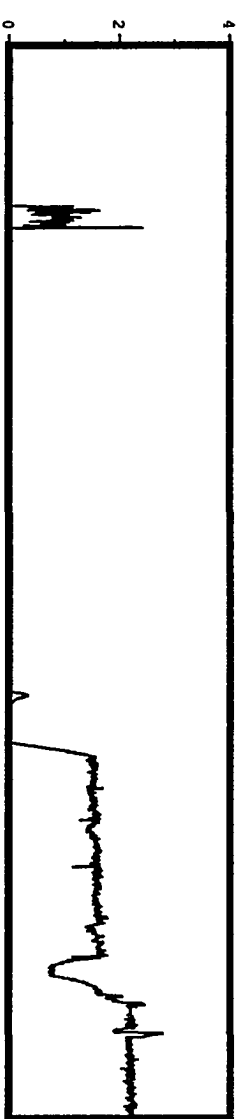
DN, cps



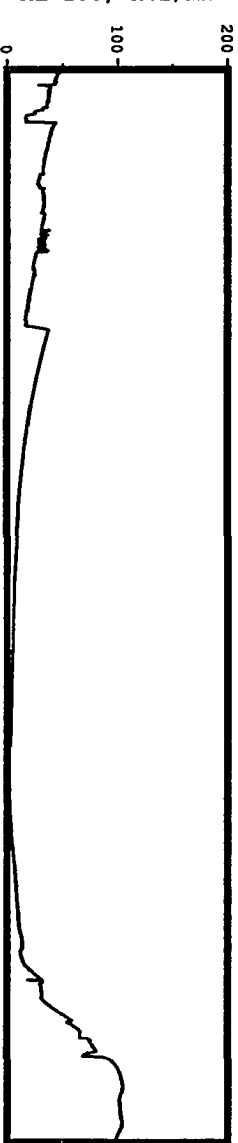
XE-135M, nCi/ml



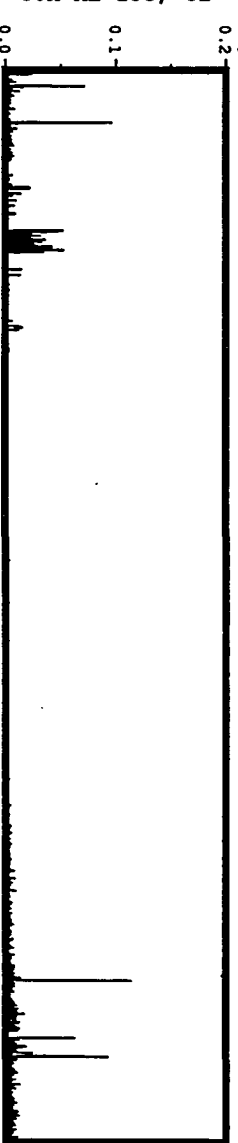
KR-87, nCi/ml



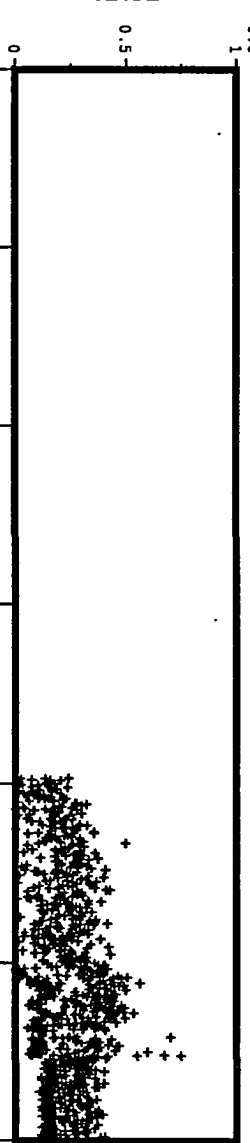
XE-133, nCi/ml



CUM XE-133, Ci



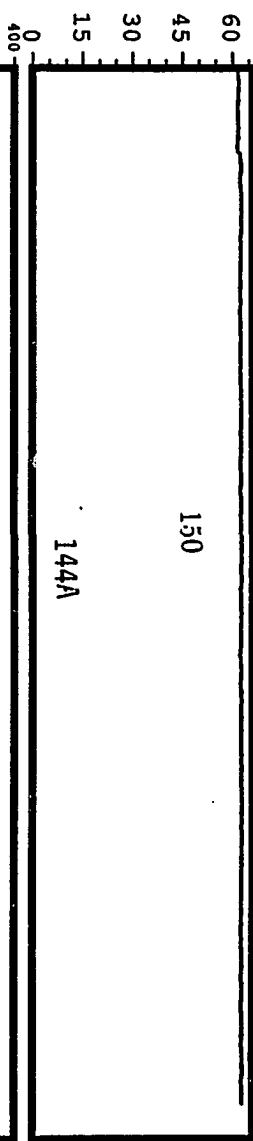
SLOPE



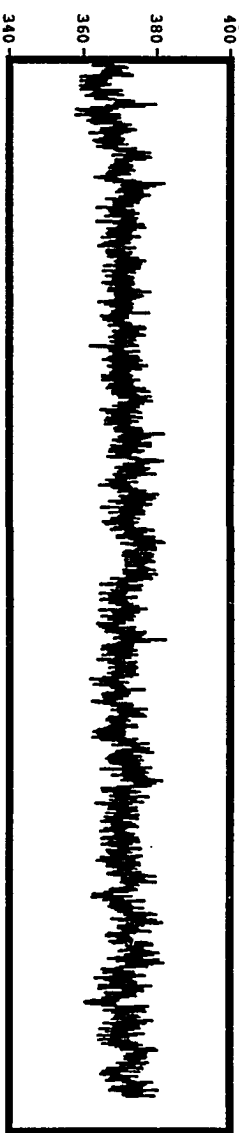
MAY
1987

1 6 11 16 21 26 31

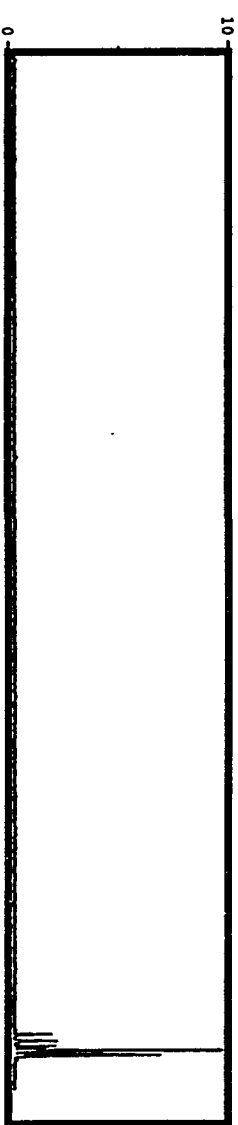
POWER, MWt



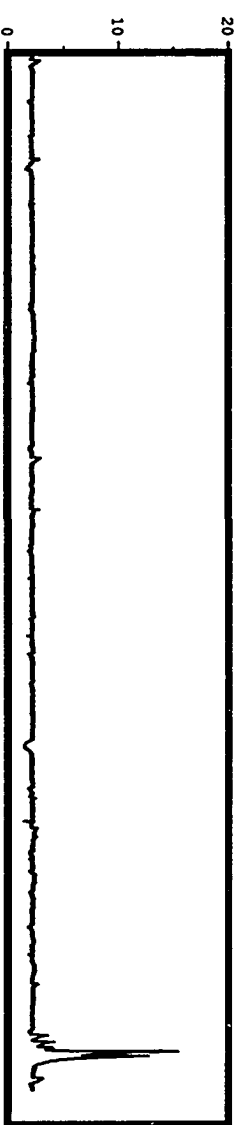
DN, cps



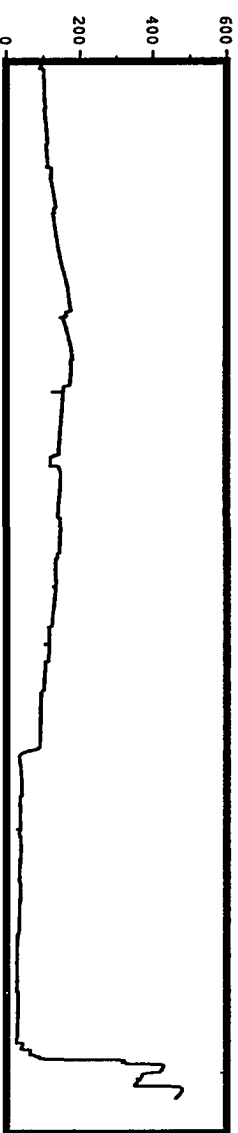
XE-135M, nCi/ml



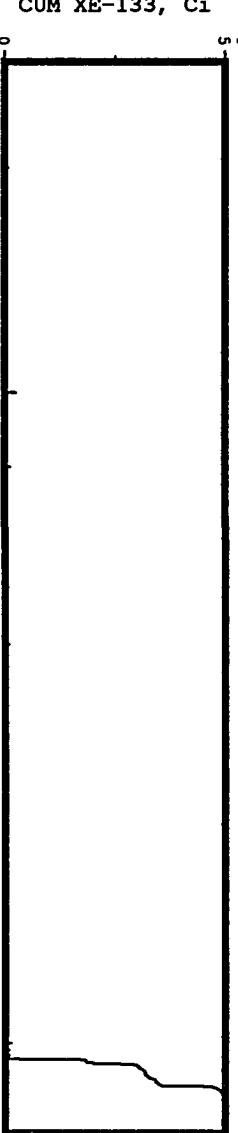
KR-87, nCi/ml



XE-133, nCi/ml



CUM XE-133, Ci



SLOPE



1
6
11
16
21
26

JUNE
1987

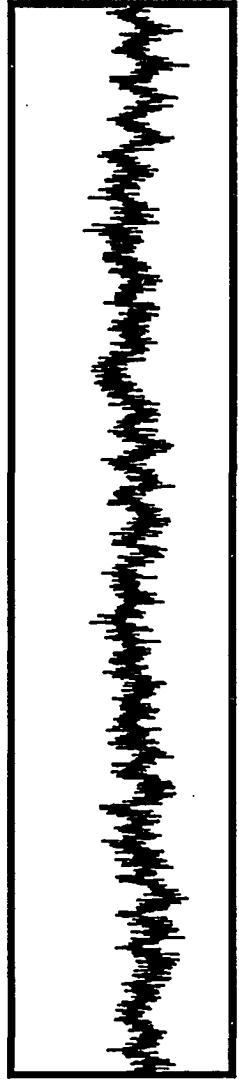
POWER, MWt

60
45
30
15
0

151
144A

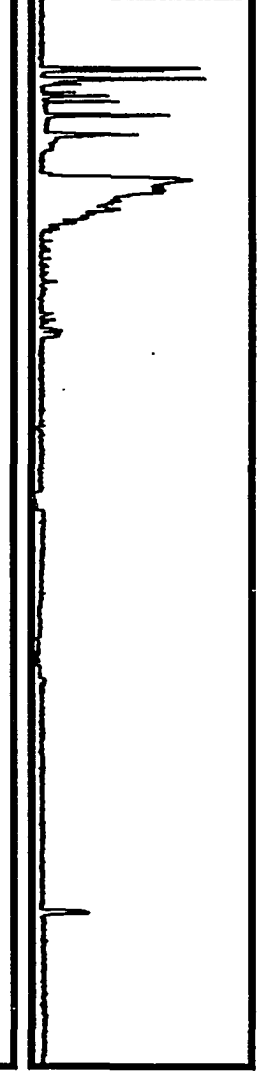
DN, cps

340
360



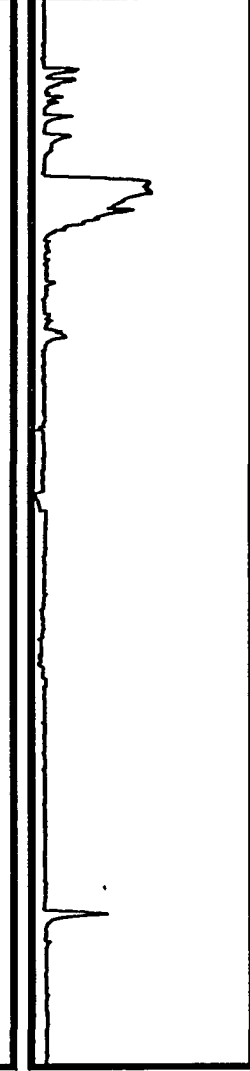
XE-135M, nCi/ml

0 2 4 6



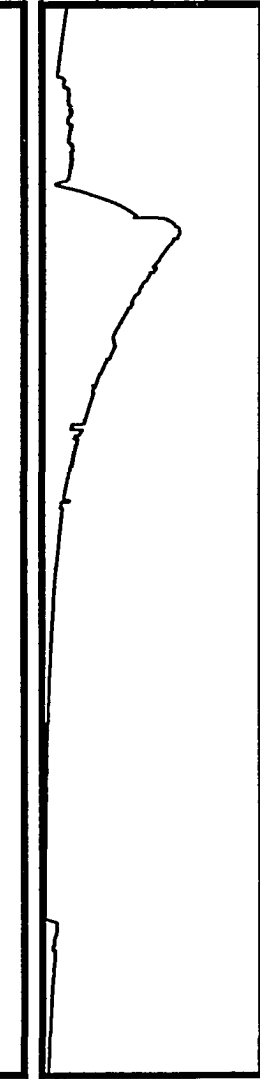
KR-87, nCi/ml

0 20 4000



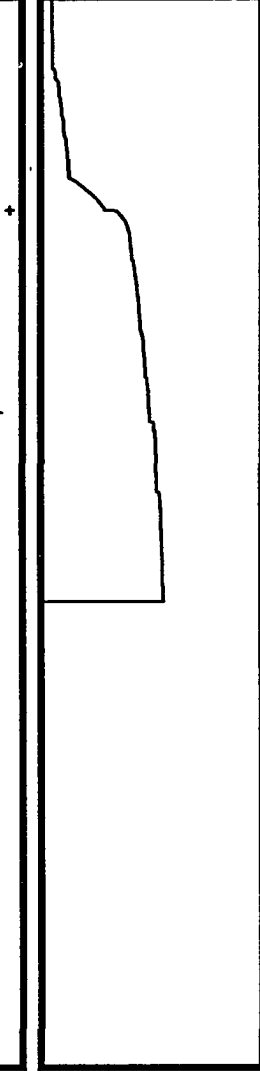
XE-133, nCi/ml

0 2000 4000



CUM XE-133, Ci

0 50 100



SLOPE

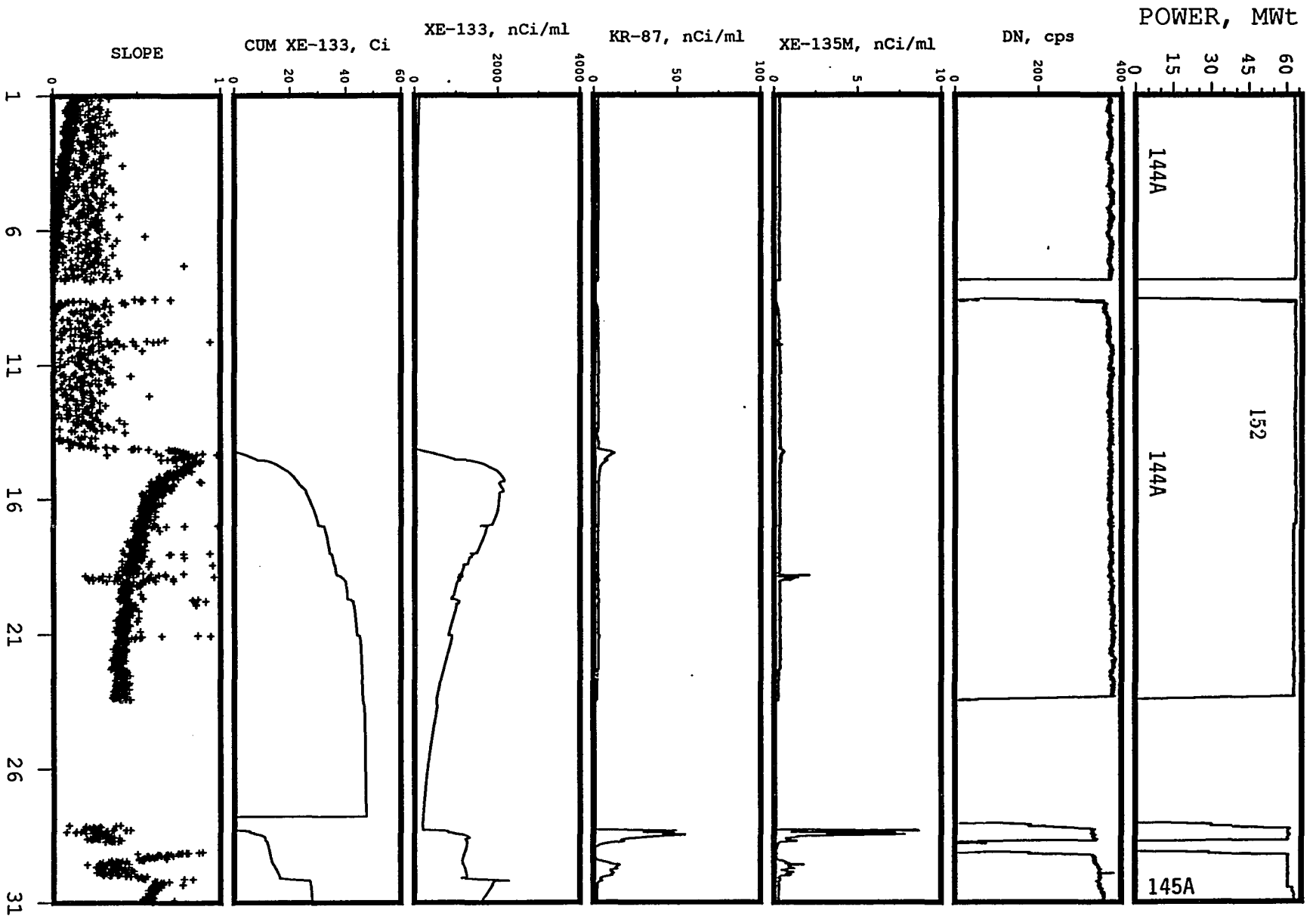
0 0.5 1



1 6 11 16 21 26 31

JULY
1987

AUGUST
1987



POWER, MWt

60
45
30
15
0

153

145A

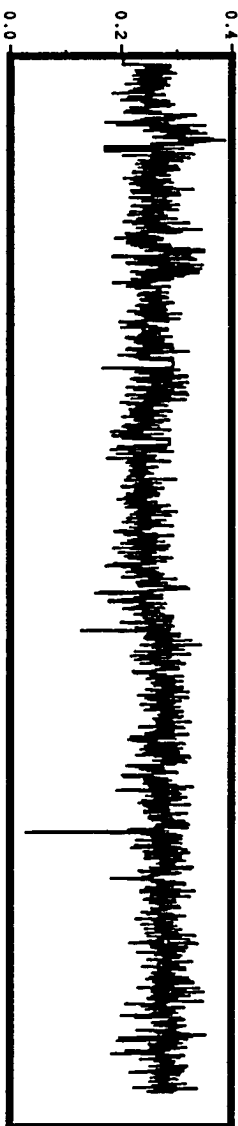
DN, cps

300
0



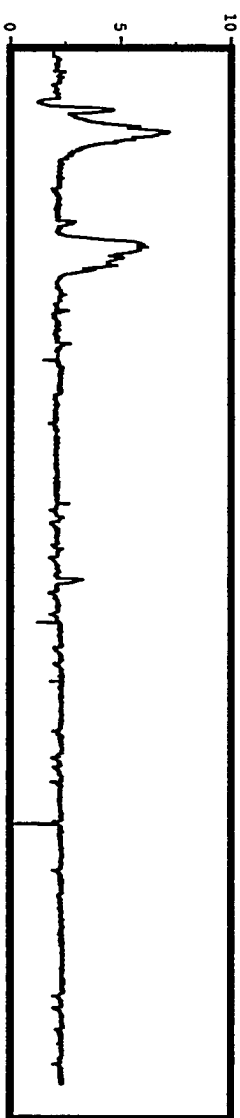
XE-135M, nCi/ml

0.4
0.2
0.0



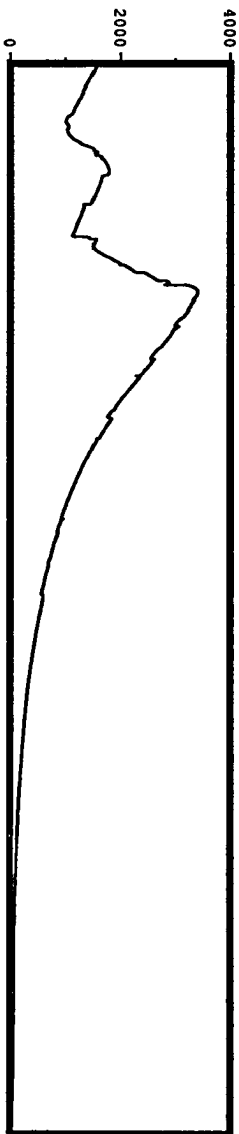
KR-87, nCi/ml

5
0



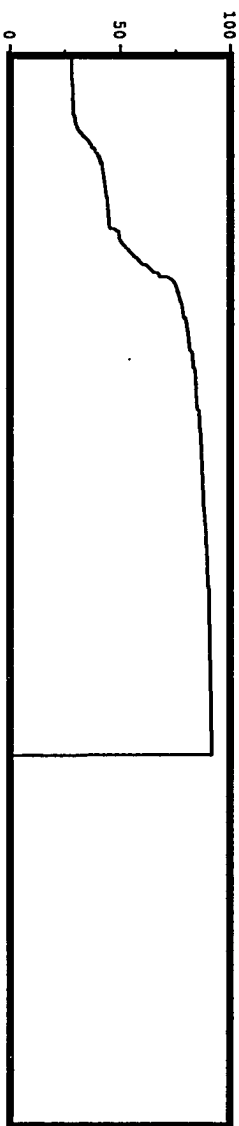
XE-133, nCi/ml

4000
2000
0



CUM XE-133, Ci

50
0



SLOPE

1
0

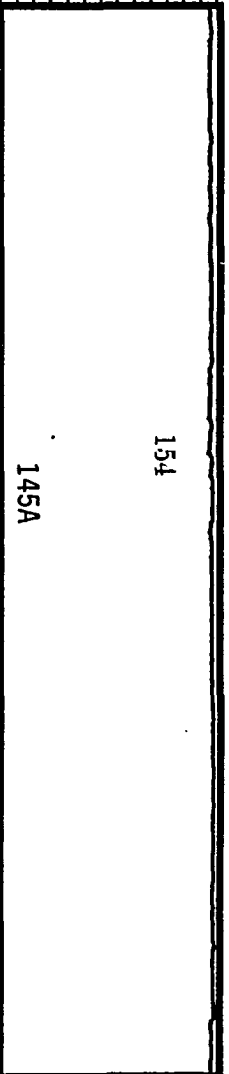


1 6 11 16 21 26

SEPTEMBER
1987

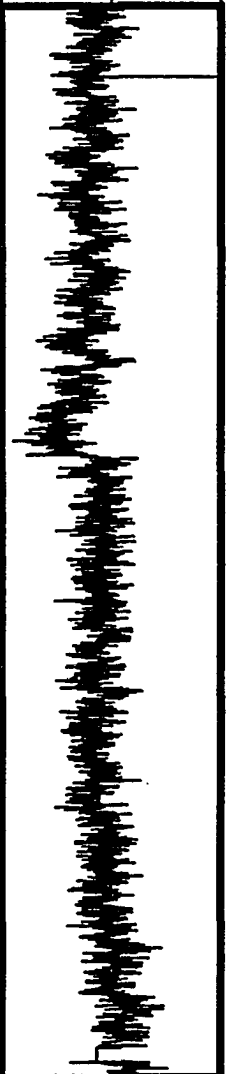
POWER, MWt

60
45
30
15
0



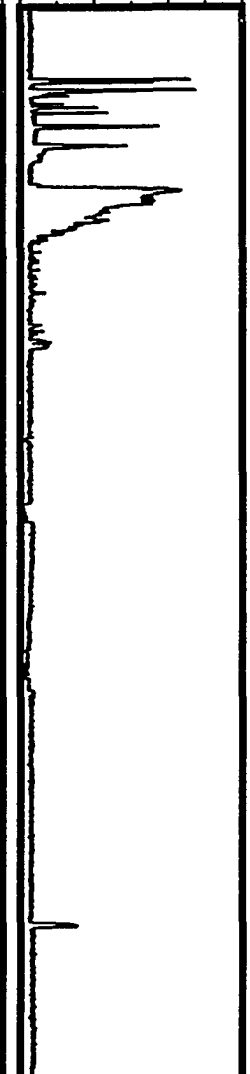
DN, cps

360
380



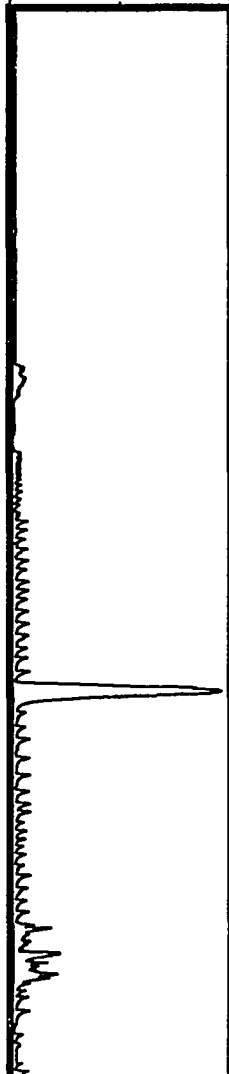
XE-135M, nCi/ml

340
6
4
2
0



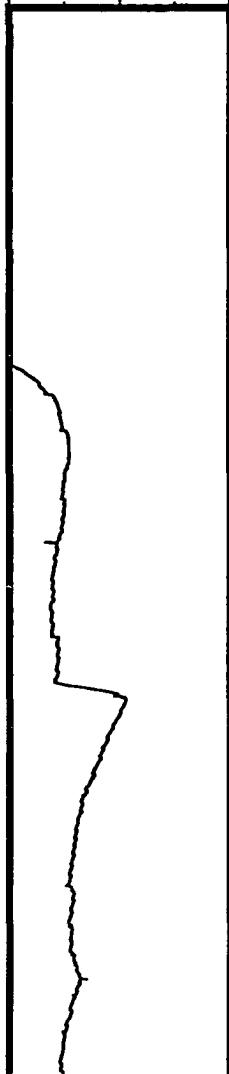
KR-87, nCi/ml

10000
0



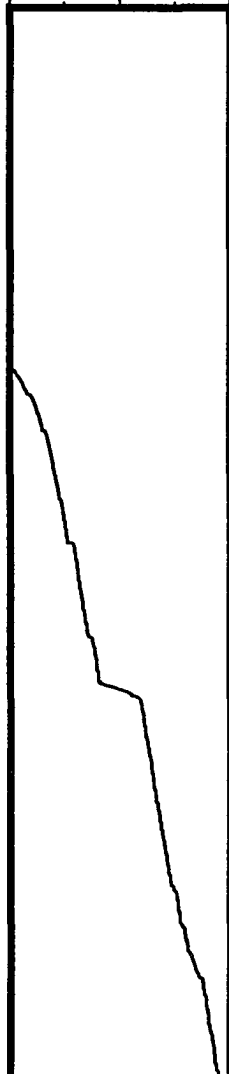
XE-133, nCi/ml

5000
200
0



CUM XE-133, Ci

100
0



SLOPE

1
0

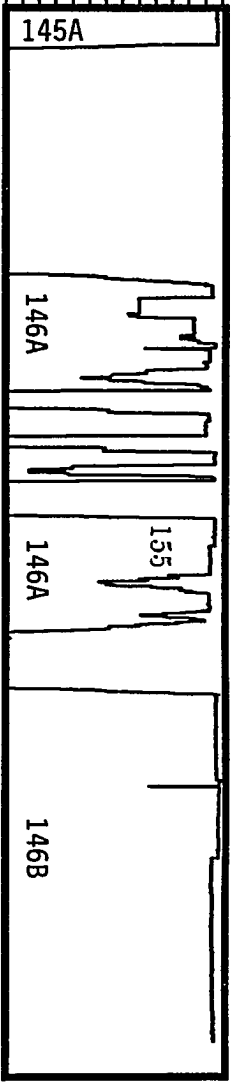


1 6 11 16 21 26 31

OCTOBER
1987

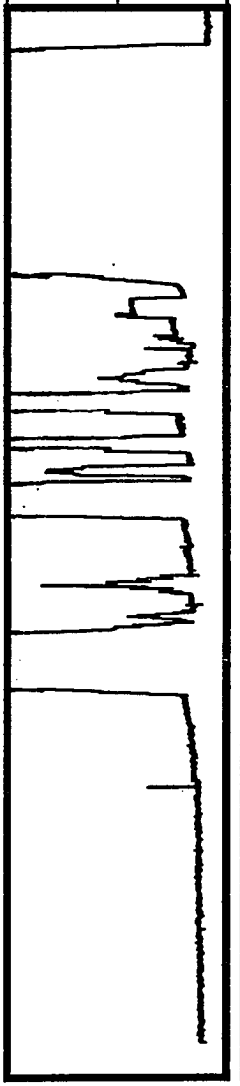
POWER, MWt

60
45
30
15
0



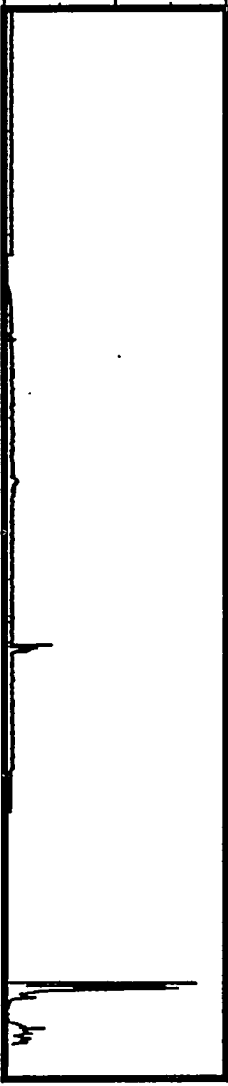
DN, cps

200
0



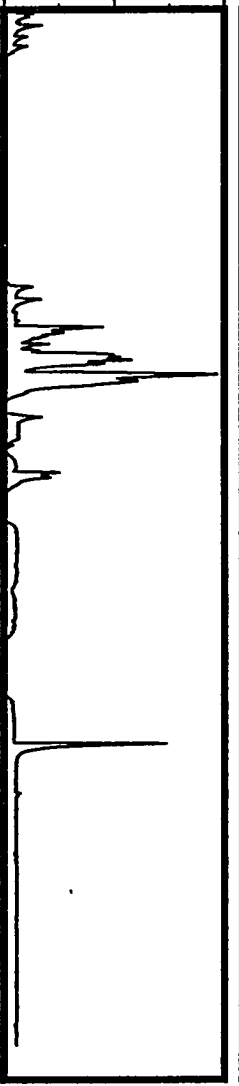
XE-135M, nCi/ml

5
0



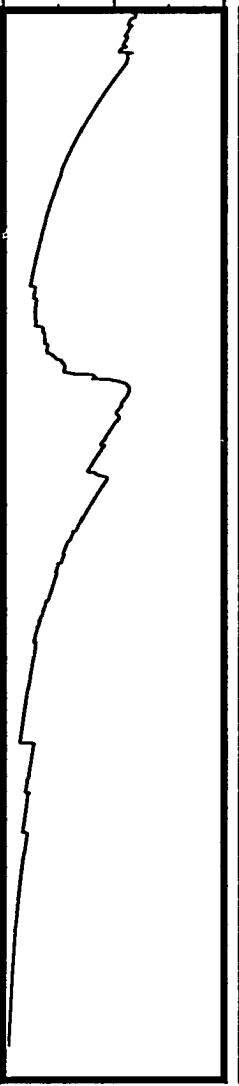
KR-87, nCi/ml

20
0



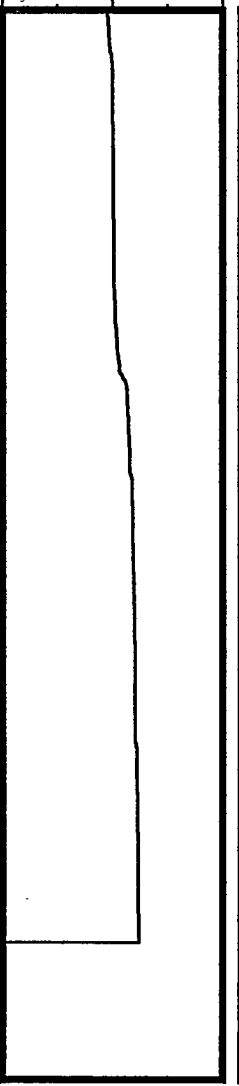
XE-133, nCi/ml

2000
0



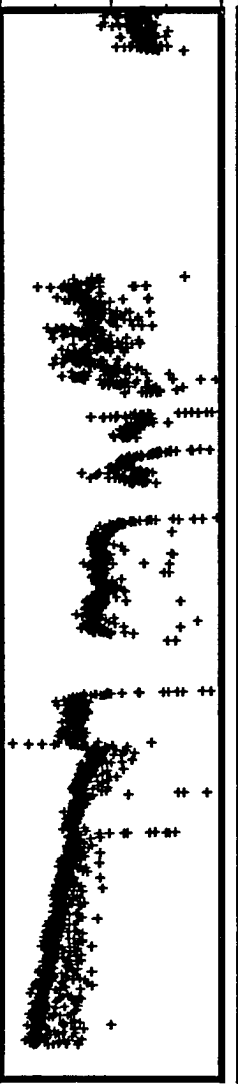
CUM XE-133, Ci

200
0



SLOPE

0.5
0



1
6
11
16
21
26

NOVEMBER
1987

POWER, MWt

60
45
30
15
0

156
1468

DN, cps

360
300
240
180
120
60
0

0.4
0.2
0.0

XE-135M, nCi/ml

60
40
20
0

KR-87, nCi/ml

4000
2000
0

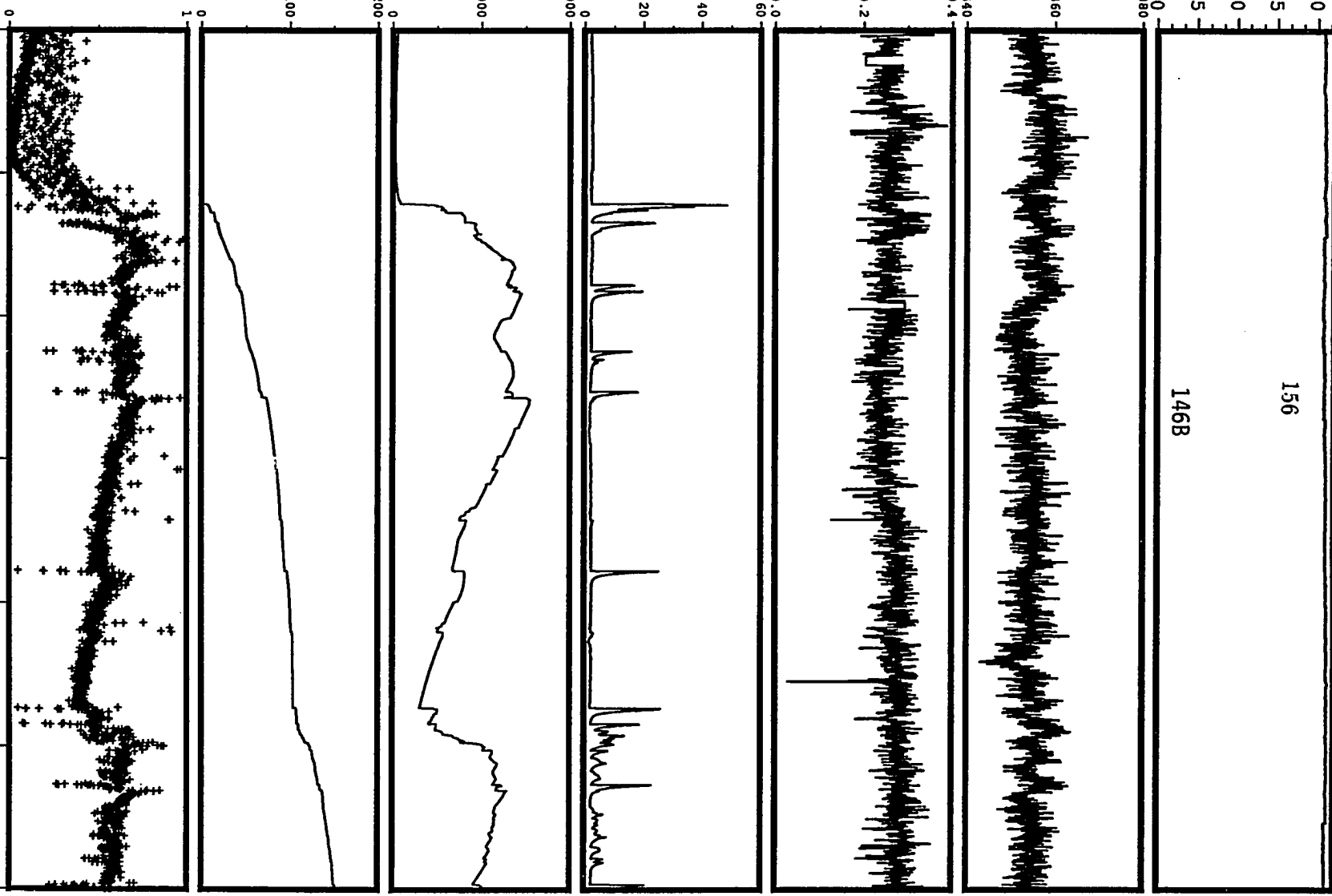
XE-133, nCi/ml

200
100
0

CUM XE-133, Ci

1
0

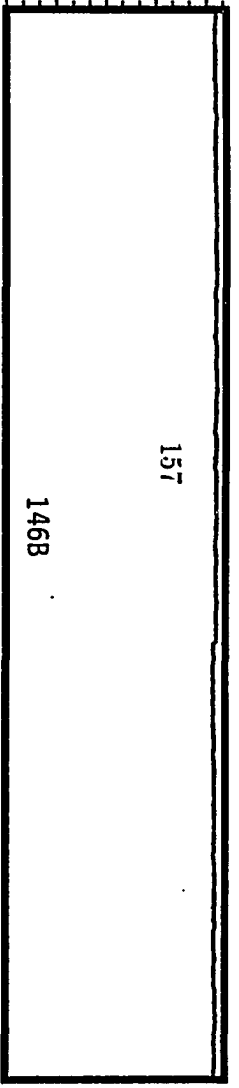
SLOPE



DECEMBER
1987

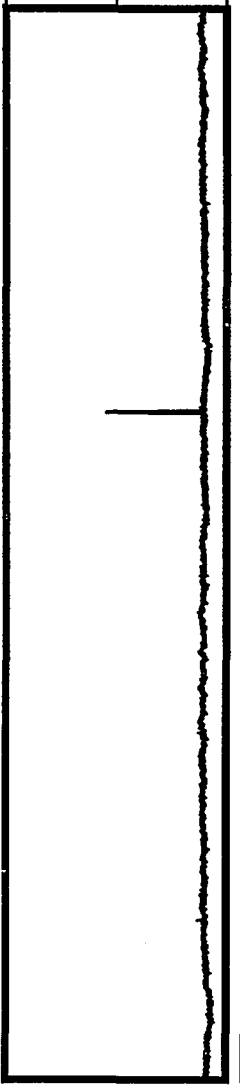
POWER, MWt

60
45
30
15
0



DN, cps

200
400
0



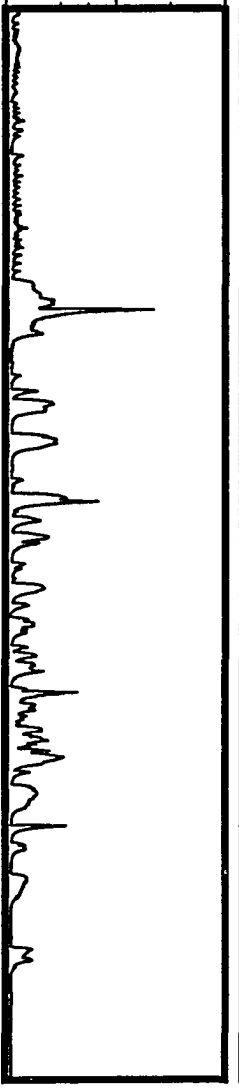
XE-135M, nCi/ml

40
20
0



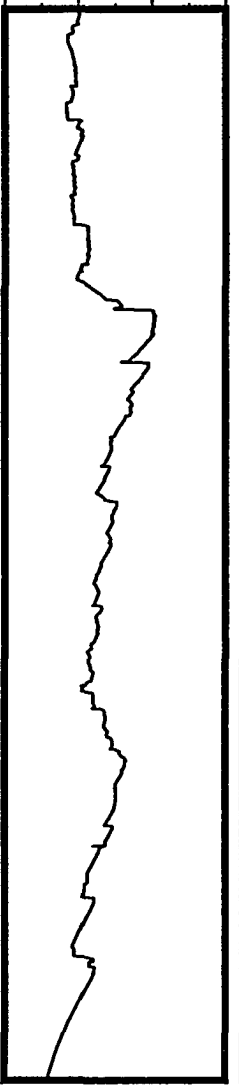
KR-87, nCi/ml

6000
0



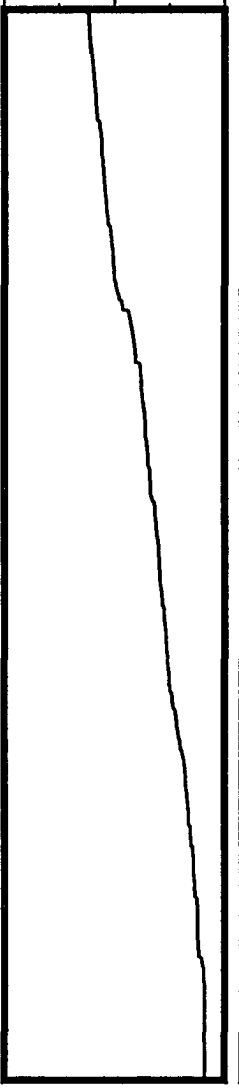
XE-133, nCi/ml

4000
2000
0



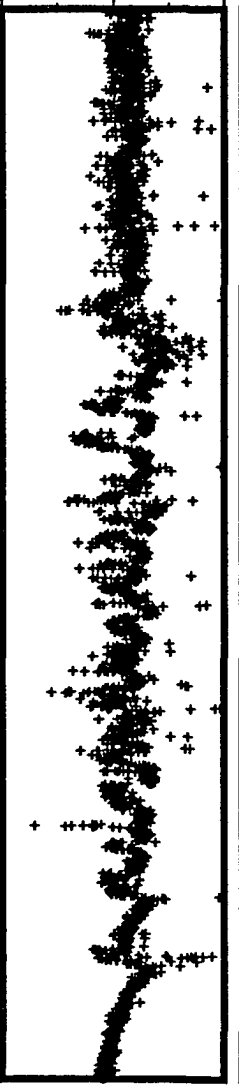
CUM XE-133, Ci

200
0



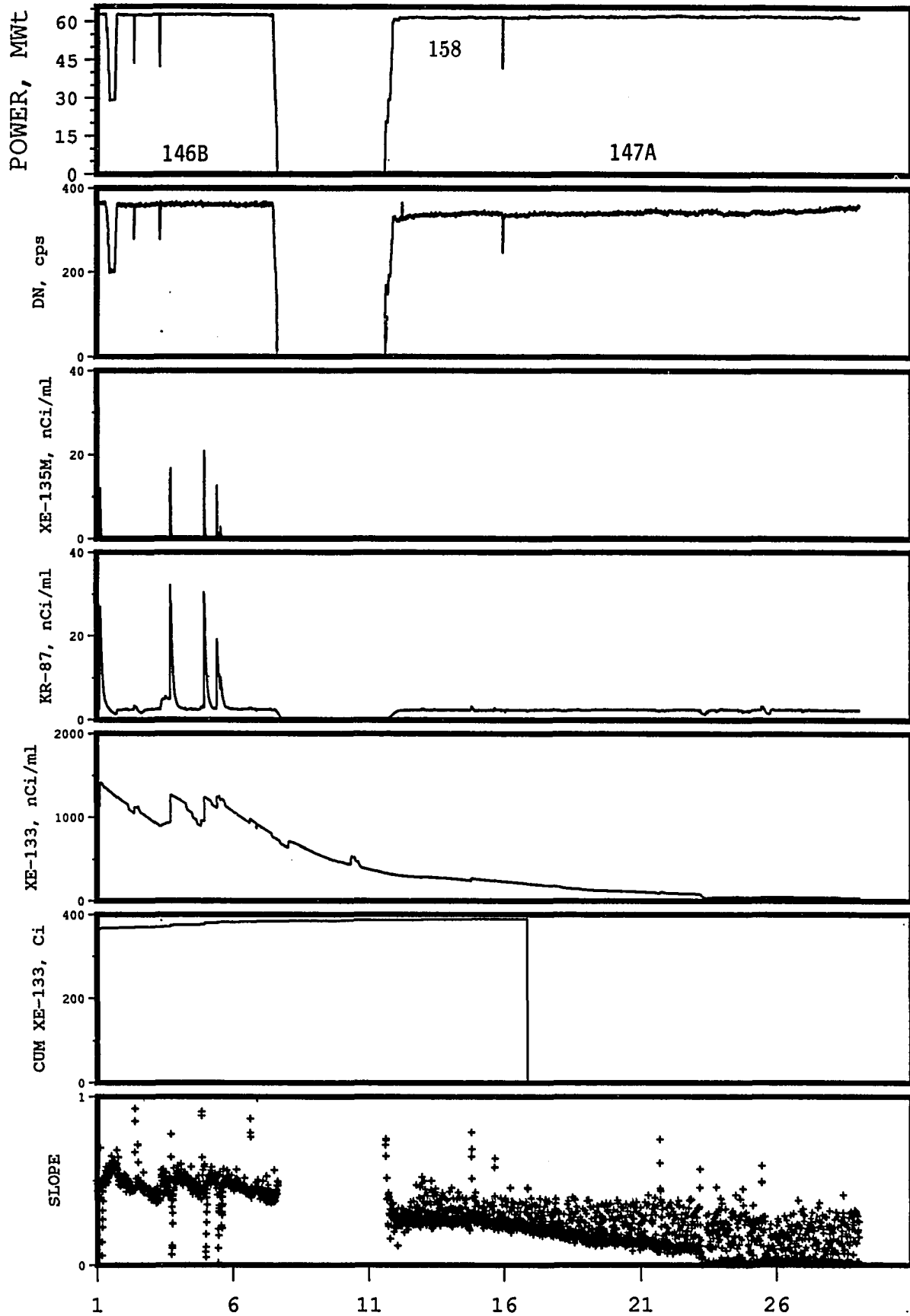
SLOPE

1
0.5
0



1 6 11 16 21 26 31

JANUARY
1988



FEBRUARY
1988

POWER, MWt

60
45
30
15
0

159

147A

DN, cps

200
400
0

XE-135M, nCi/ml

0.6
0.4
0.2
0.0

KR-87, nCi/ml

5
10
0

XE-133, nCi/ml

100
200
0

CUM XE-133, Ci

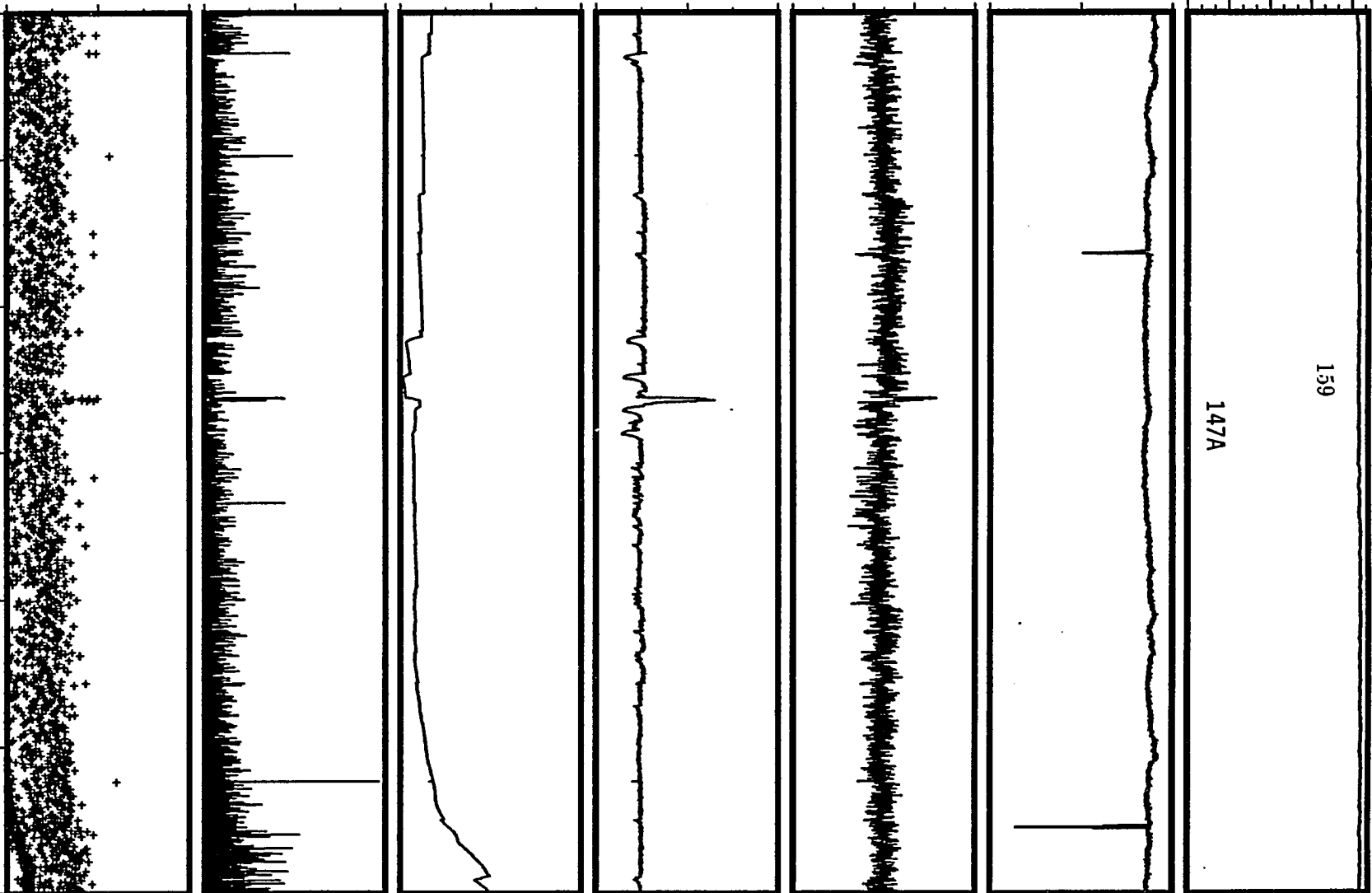
0.02
0.00
1

SLOPE

0.5
0

1 6 11 16 21 26 31

MARCH
1988



POWER, MWt

60
45
30
15
0

160

DN, cps

200
0

XE-135M, nCi/ml

200
100
0

KR-87, nCi/ml

100
0

XE-133, nCi/ml

100
0

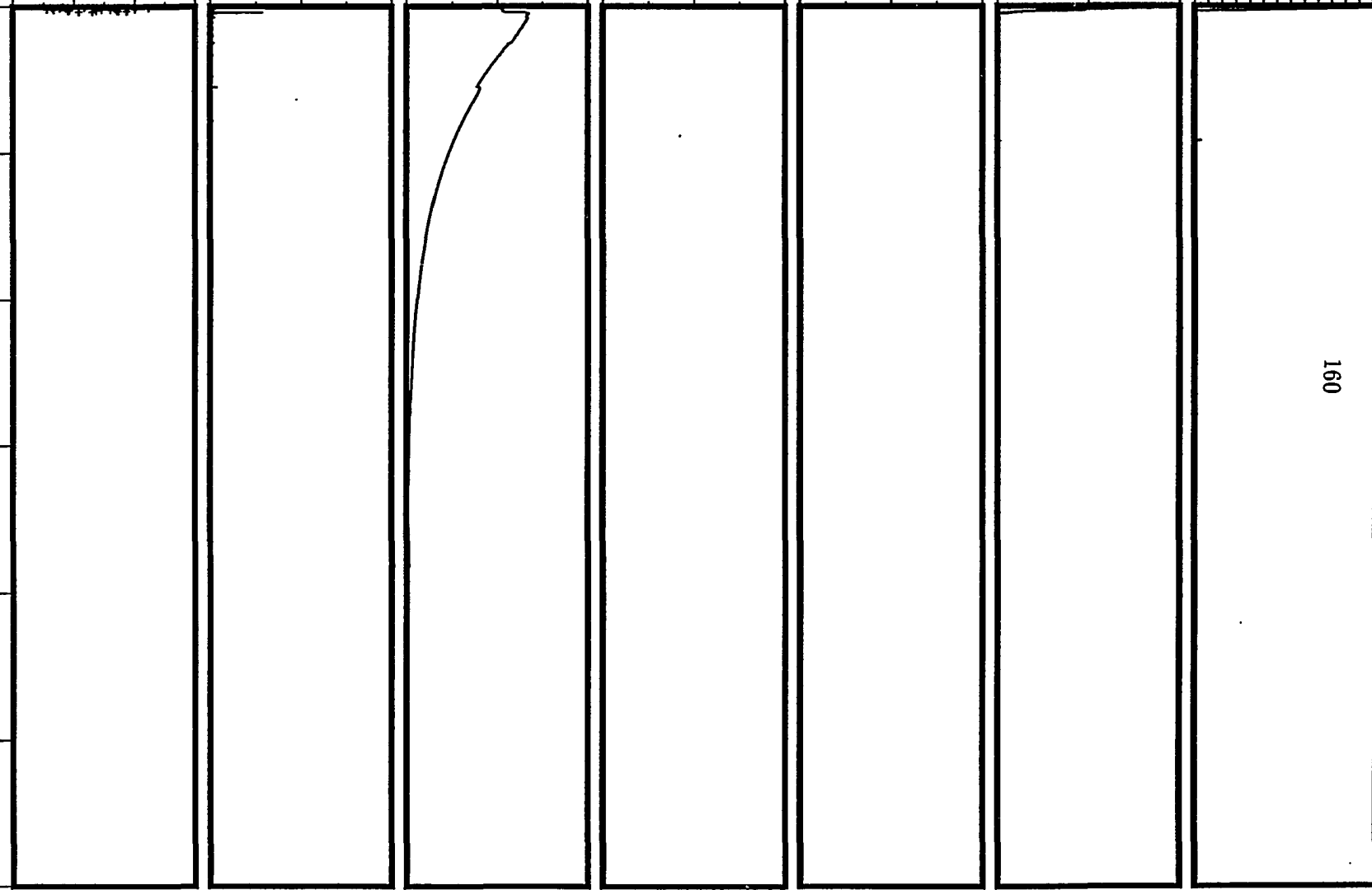
CUM XE-133, Ci

0.2
0

SLOPE

0.4
0.2
0.0

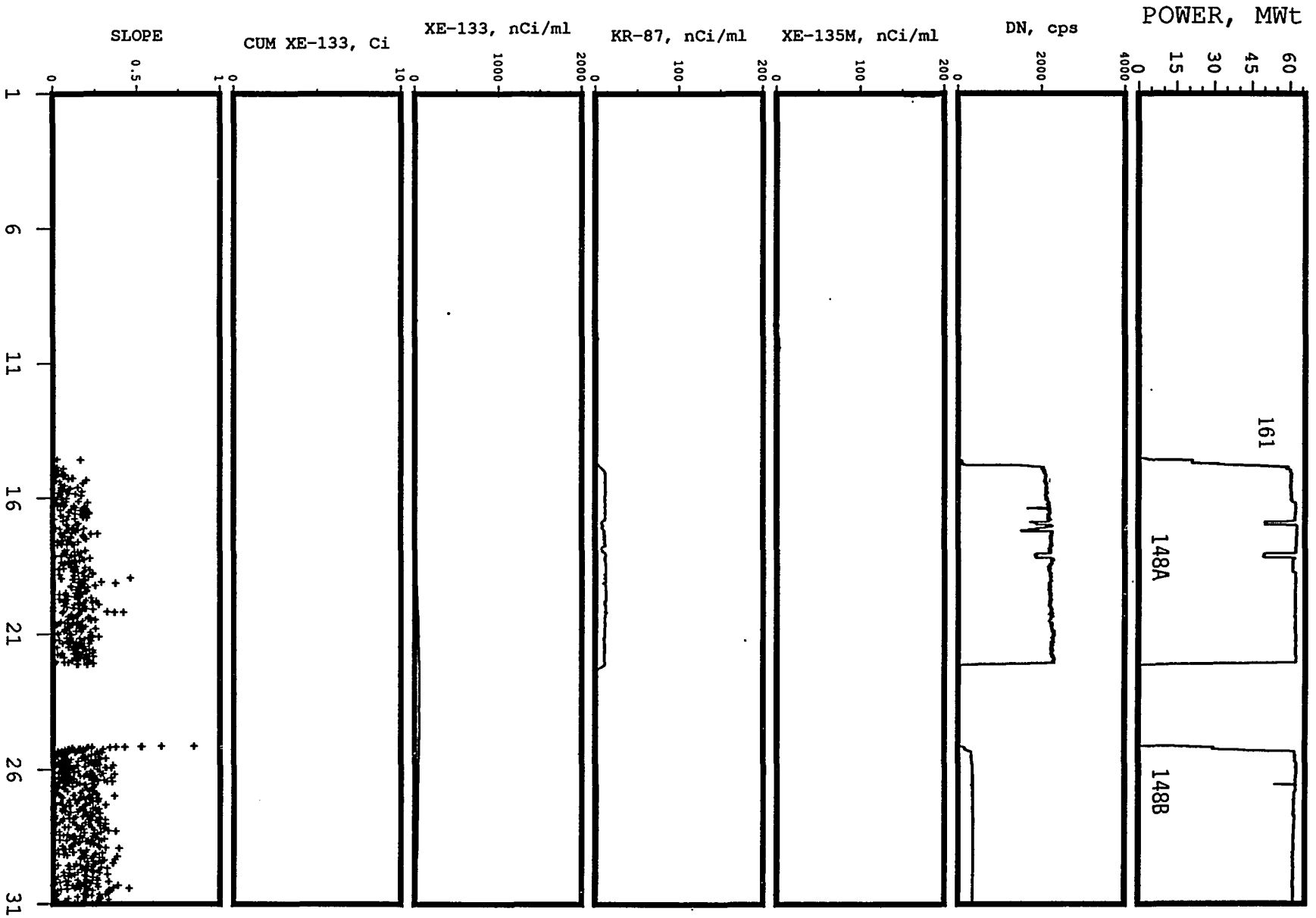
1
6
11
16
21
26



APRIL

1988

MAY
1988



POWER, MWt

60
45
30
15
0

162

1488

DN, cps

200
400

XE-135M, nCi/ml

0.4
0.2
0.0

KR-87, nCi/ml

2
1

XE-133, nCi/ml

40
30
20
10
0

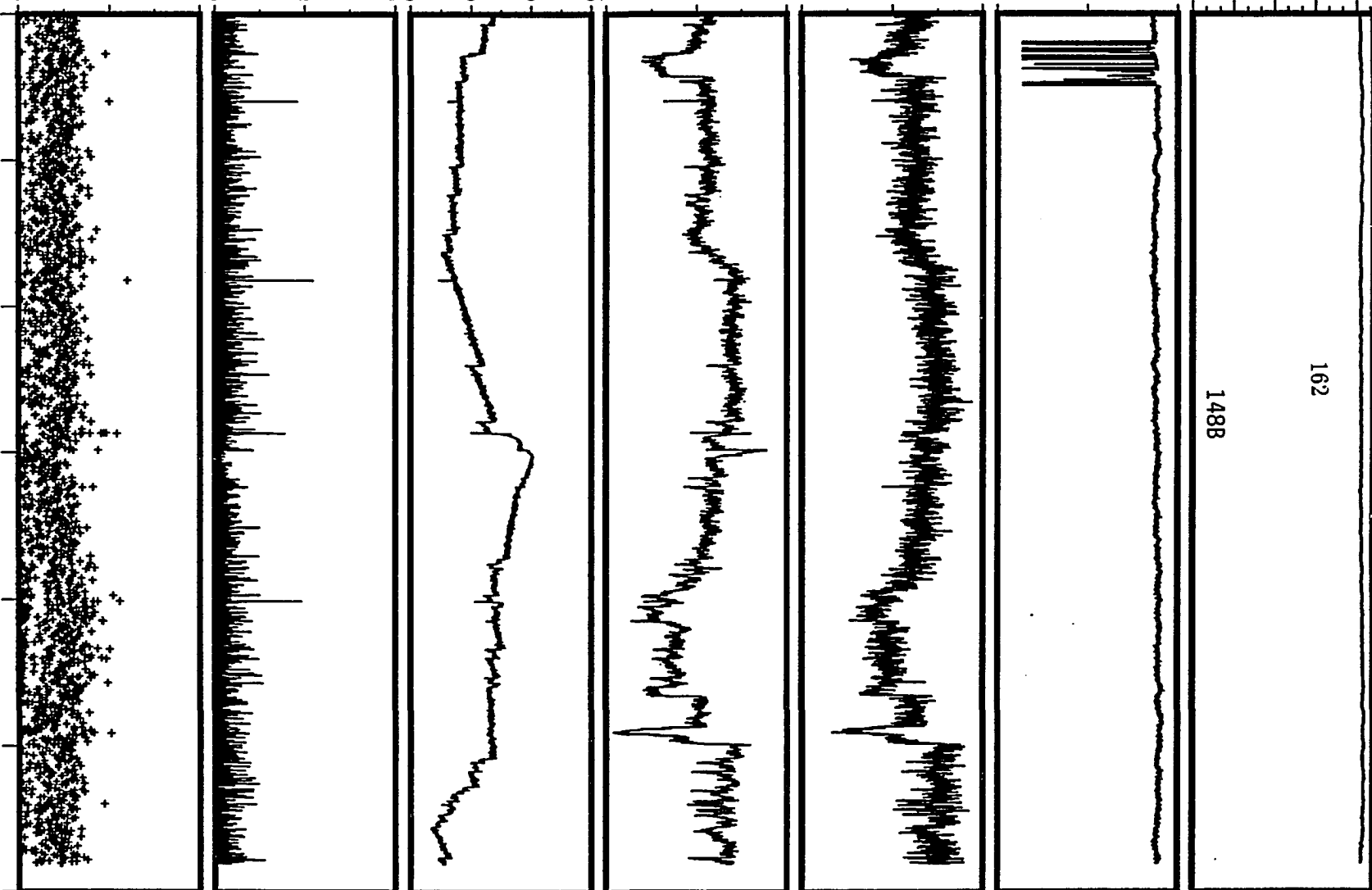
CUM XE-133, Ci

0.02
0.00
1

SLOPE

0.5
0

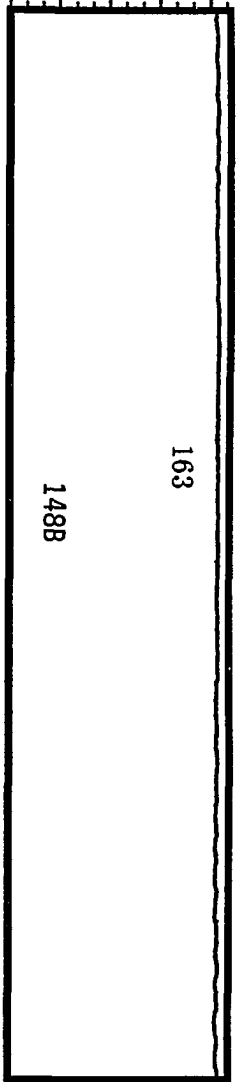
1 6 11 16 21 26



JUNE
1988

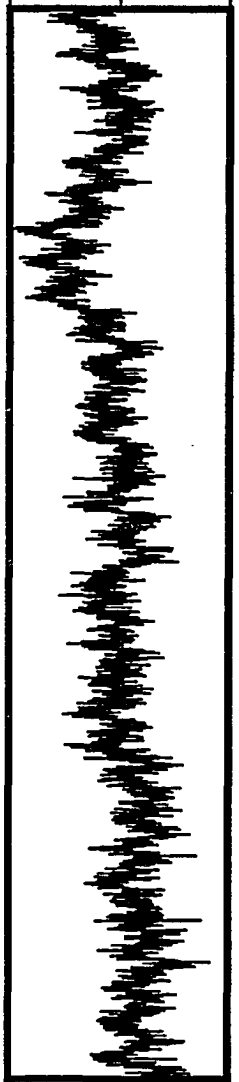
POWER, MWt

60
45
30
15
0



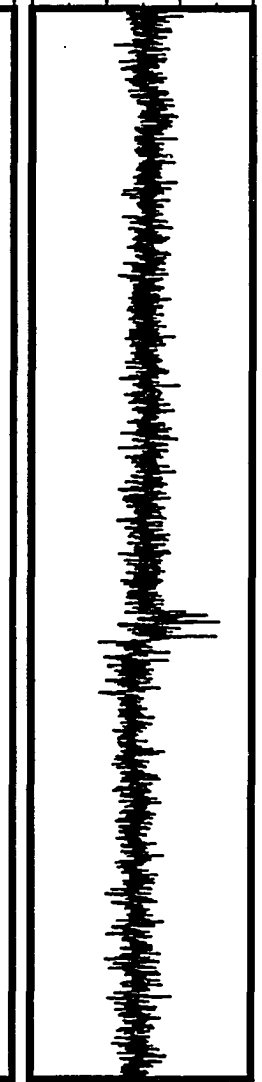
DN, cps

360
340



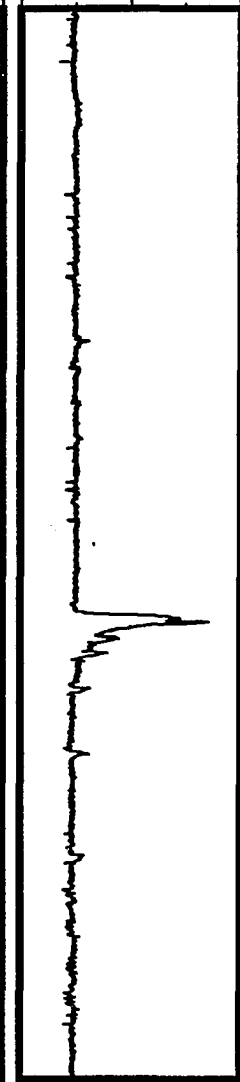
XE-135M, nCi/ml

0.6
0.4
0.2
0.0



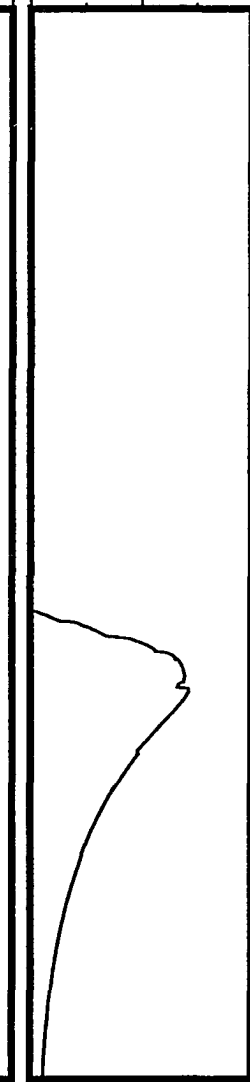
KR-87, nCi/ml

5
10



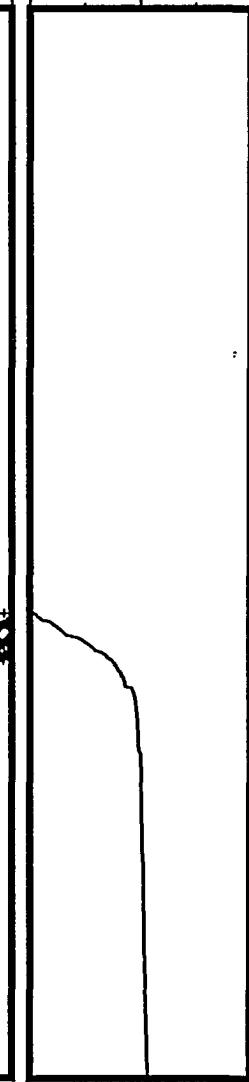
XE-133, nCi/ml

10000
5000
0



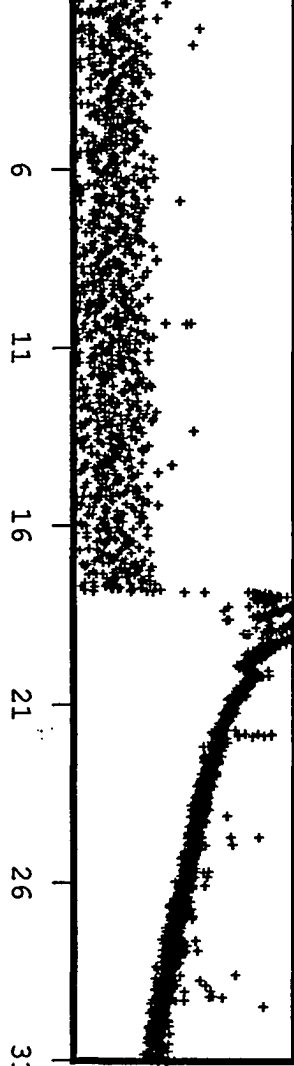
CUM XE-133, Ci

1
0



SLOPE

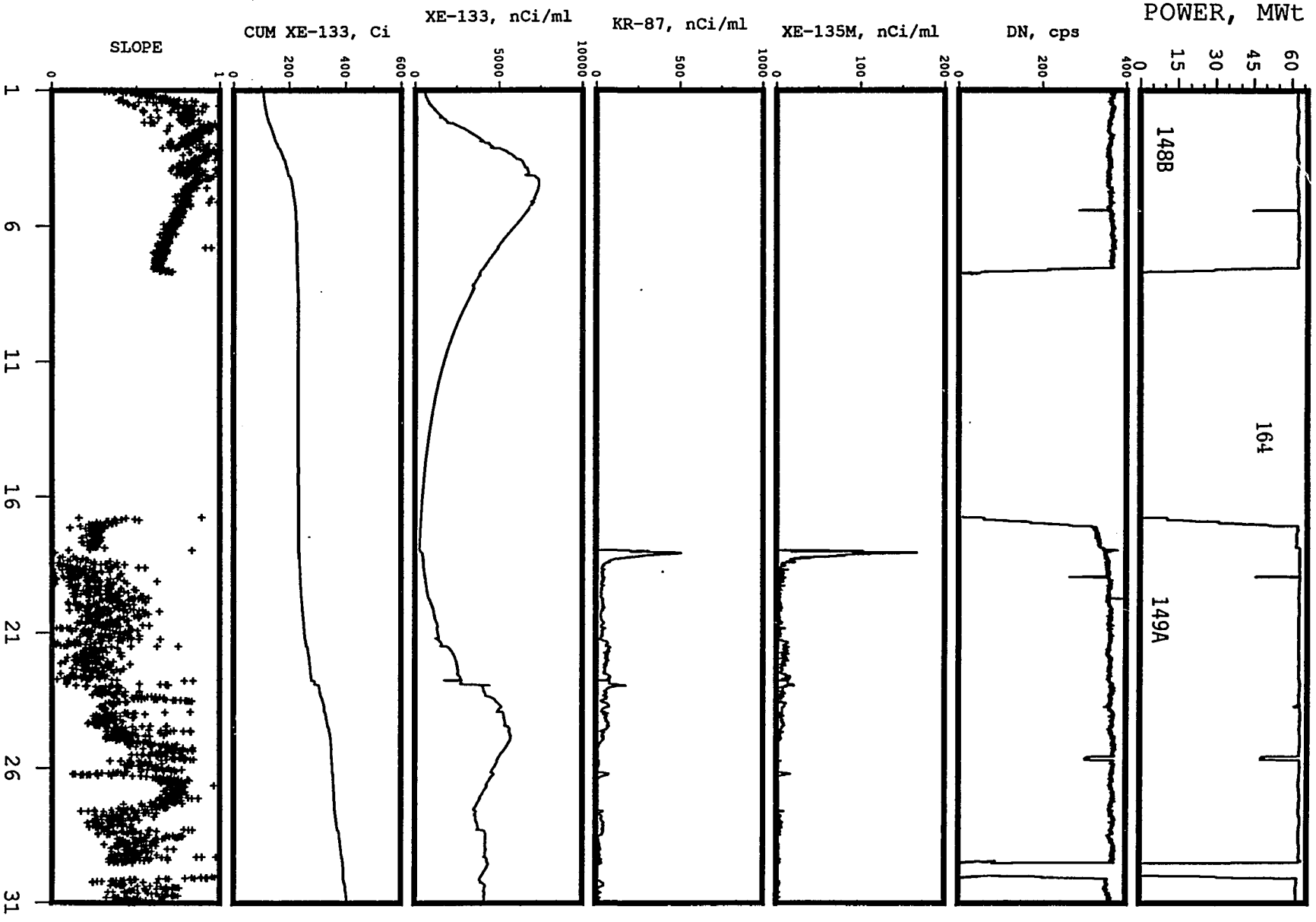
0
1



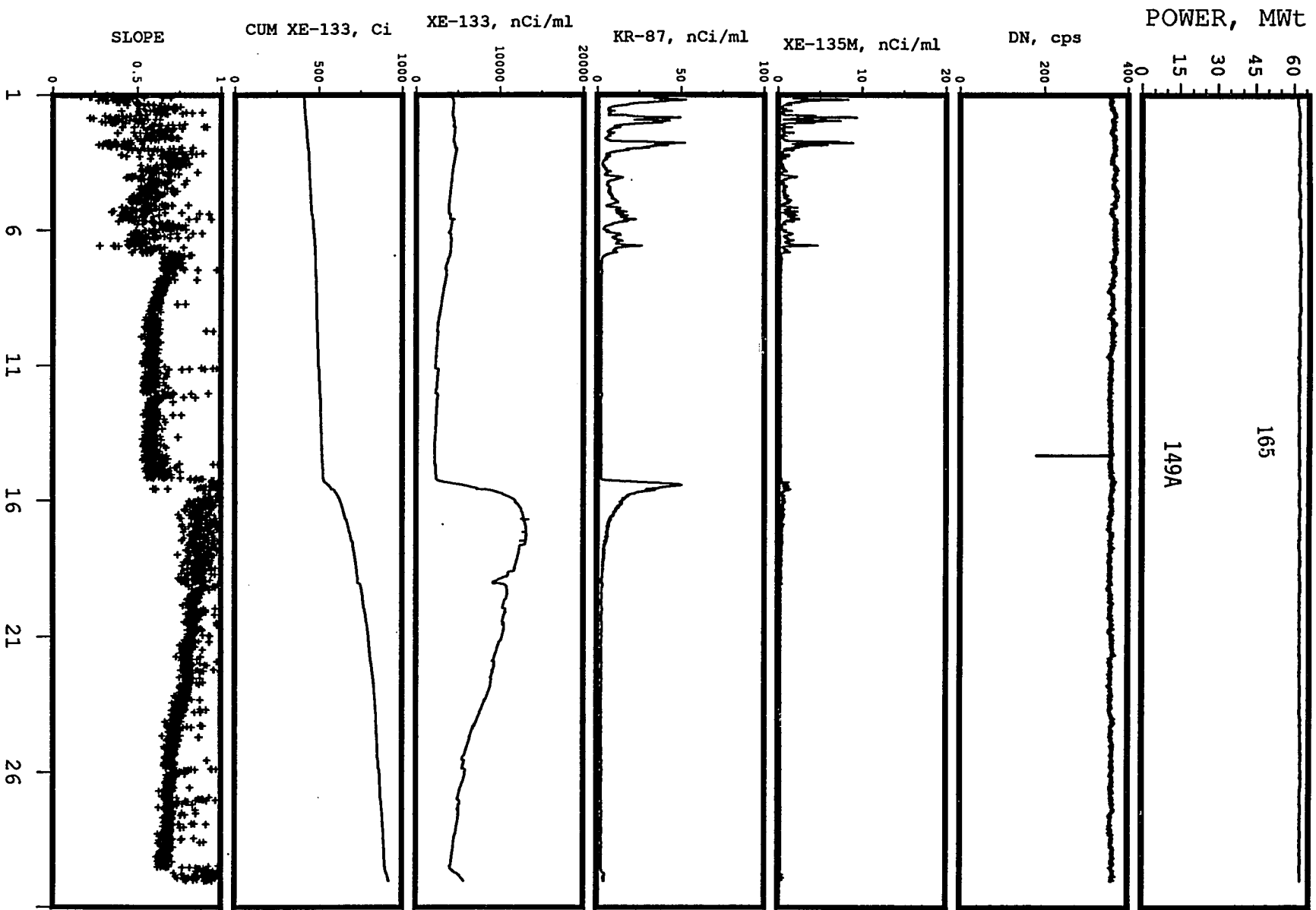
1
6
11
16
21
26
31

JULY
1988

AUGUST
1988



SEPTEMBER
1988



POWER, MWt

166

149A

DN, cps

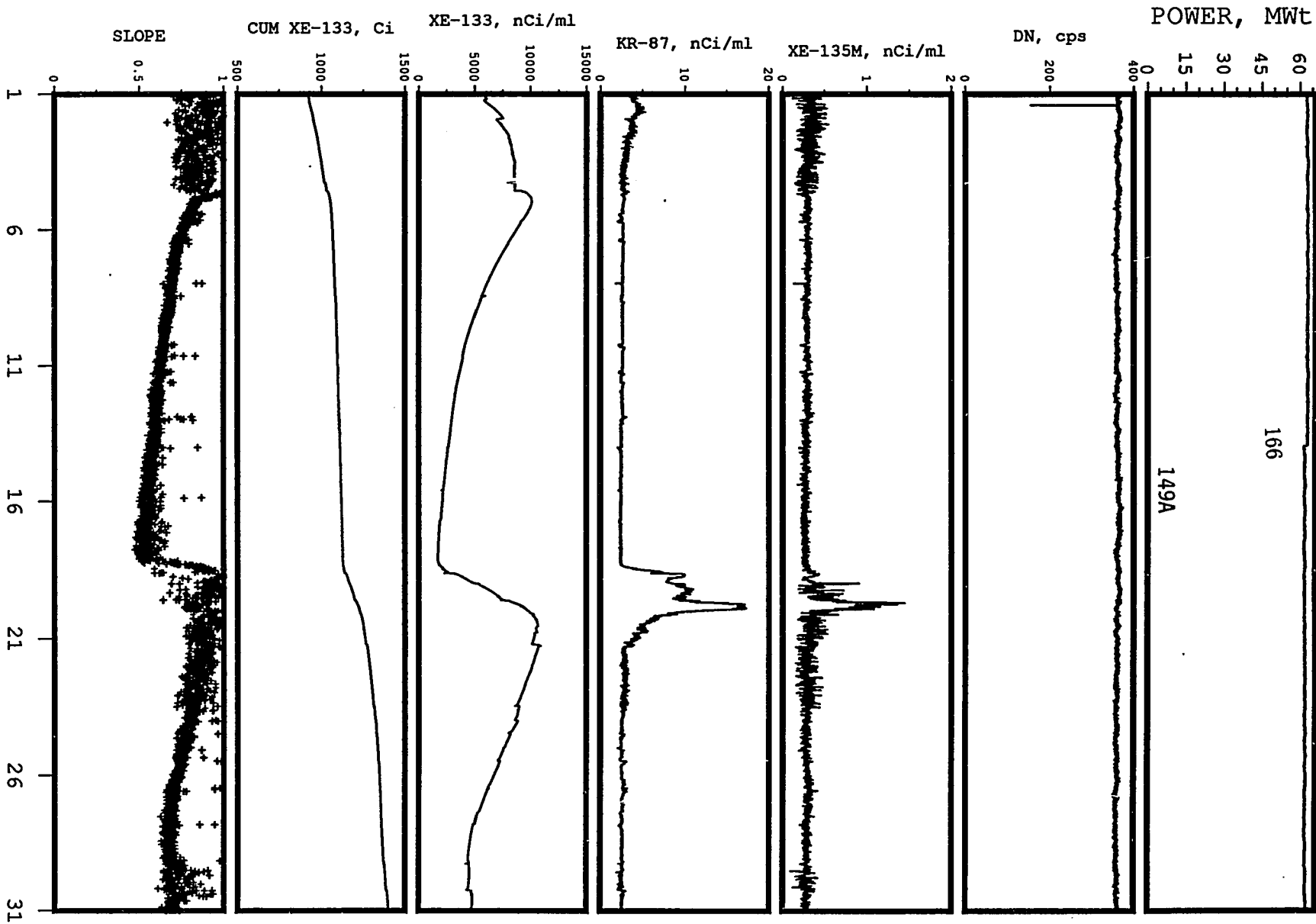
XE-135M, nCi/ml

KR-87, nCi/ml

XE-133, nCi/ml

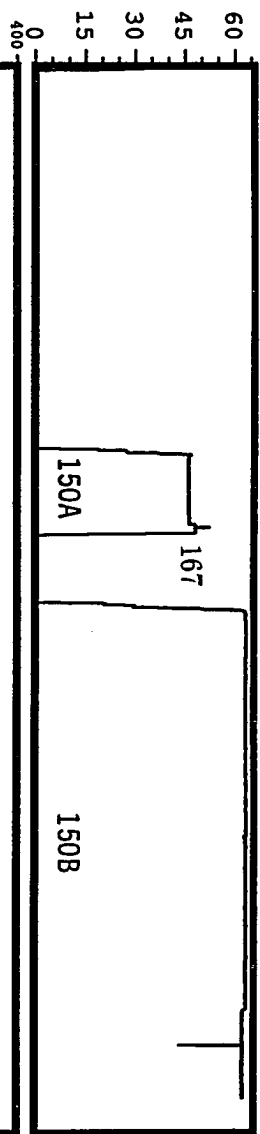
CUM XE-133, Ci

SLOPE

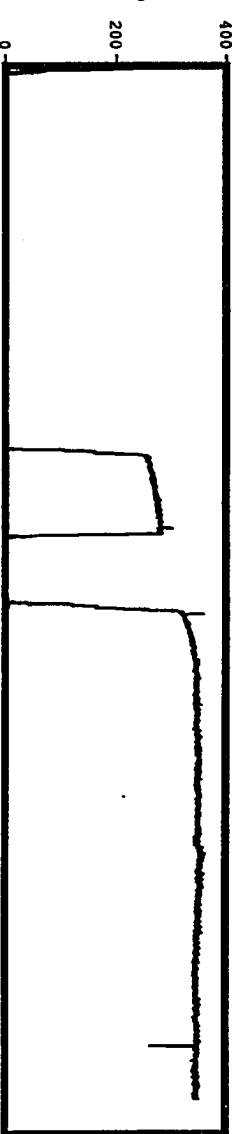


OCTOBER
1988

POWER, MWt



DN, cps



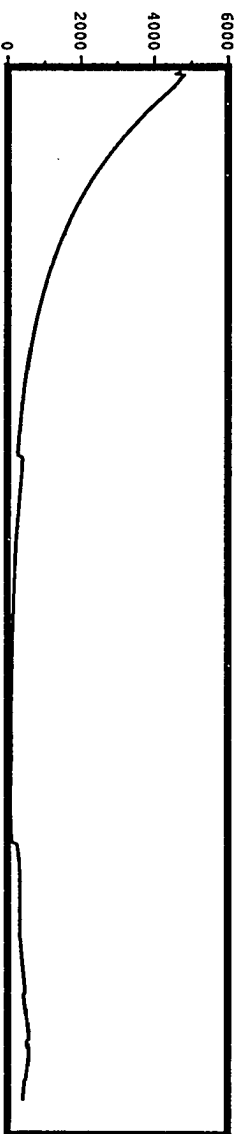
XE-135M, nCi/ml



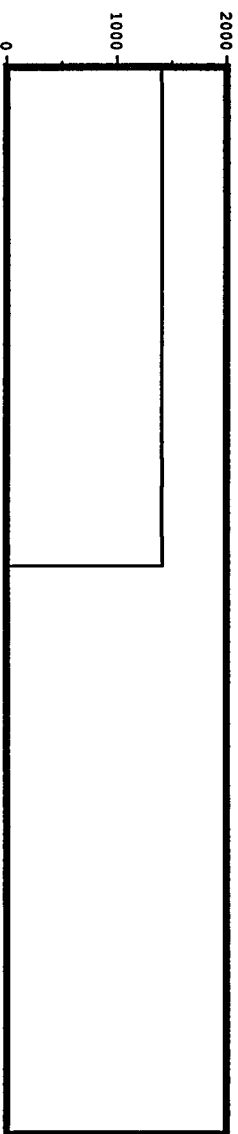
KR-87, nCi/ml



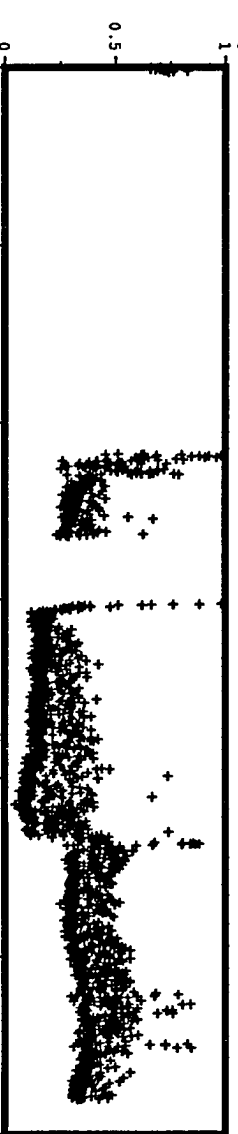
XE-133, nCi/ml



CUM XE-133, Ci



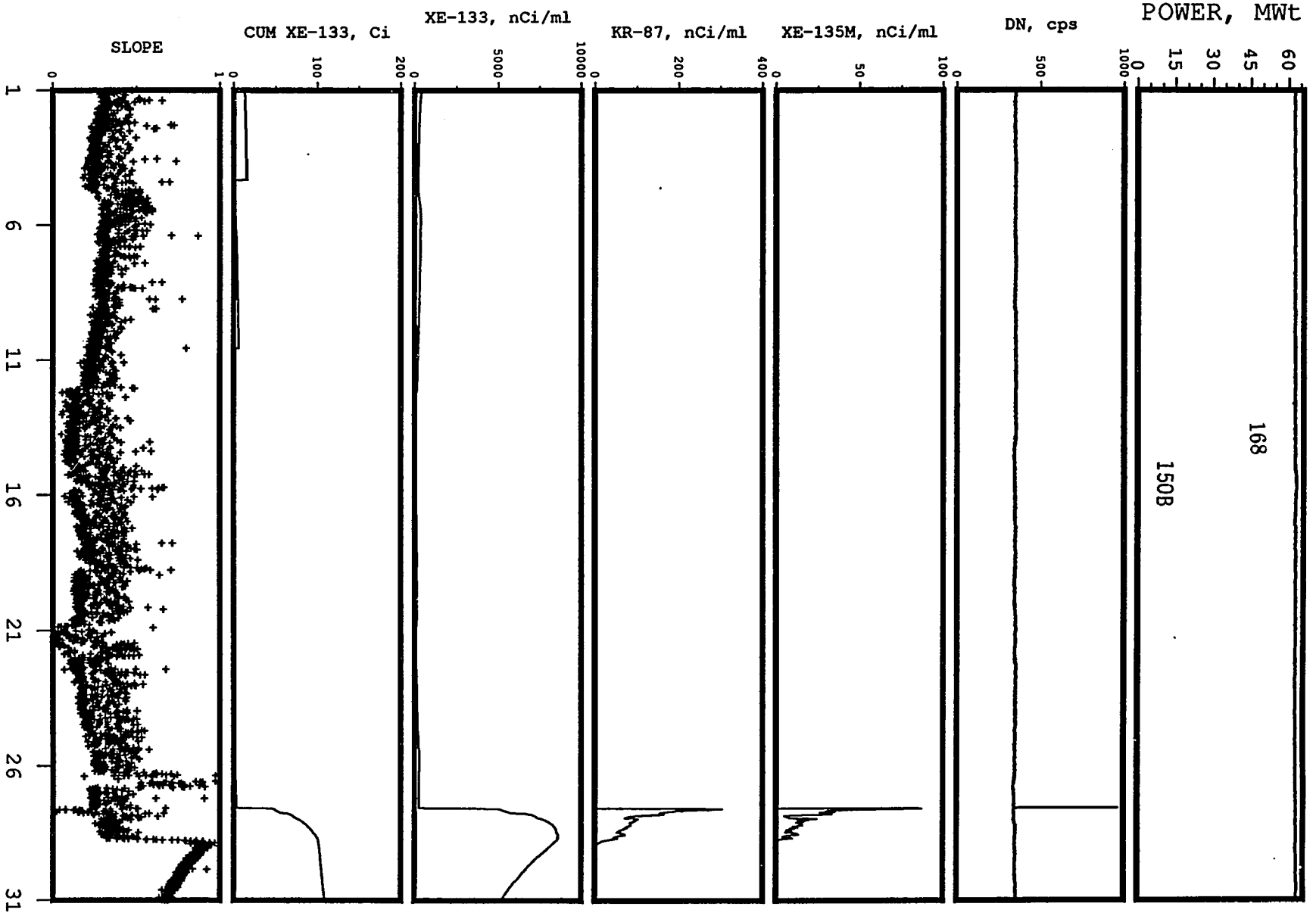
SLOPE



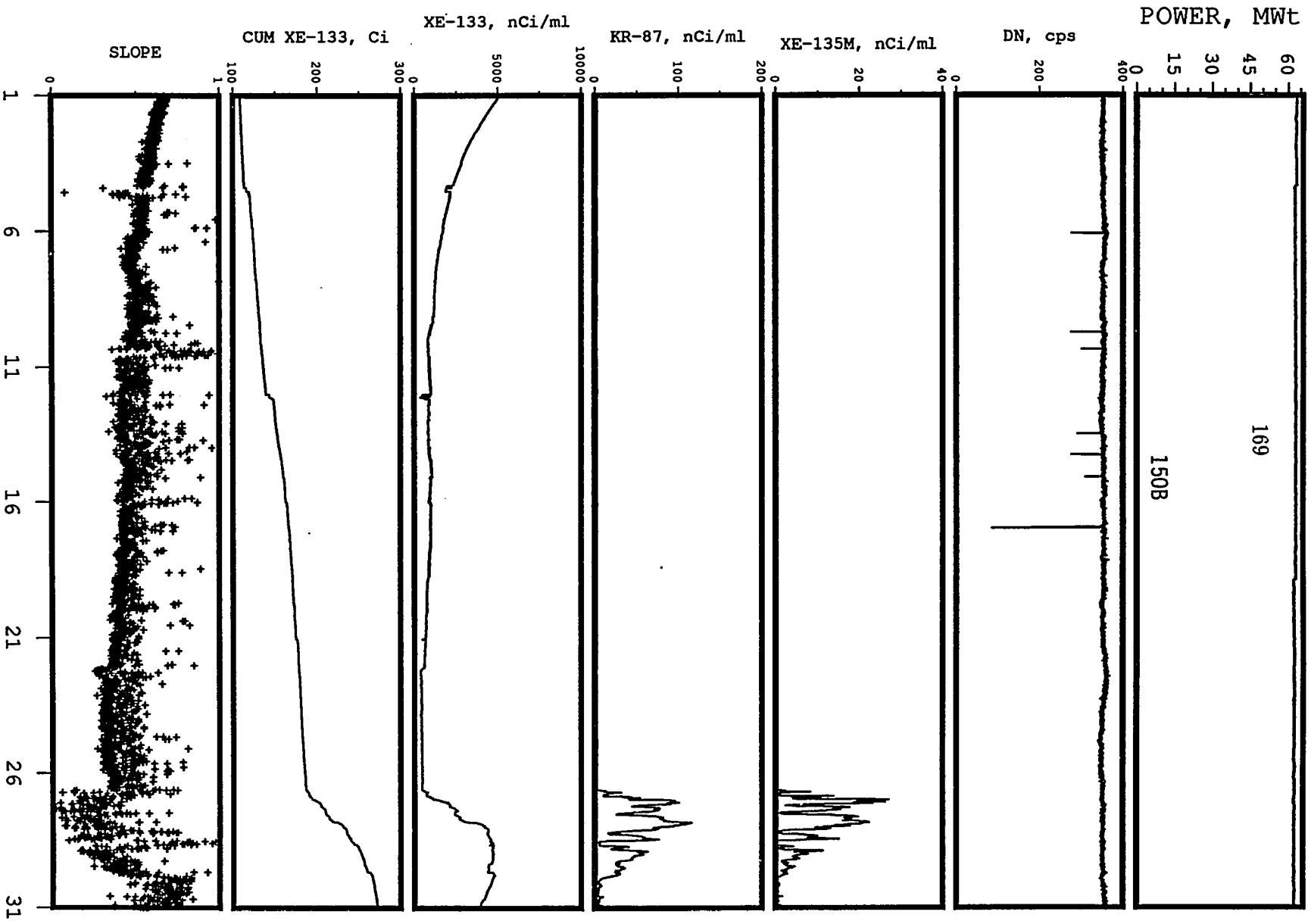
1 6 11 16 21 26

NOVEMBER
1988

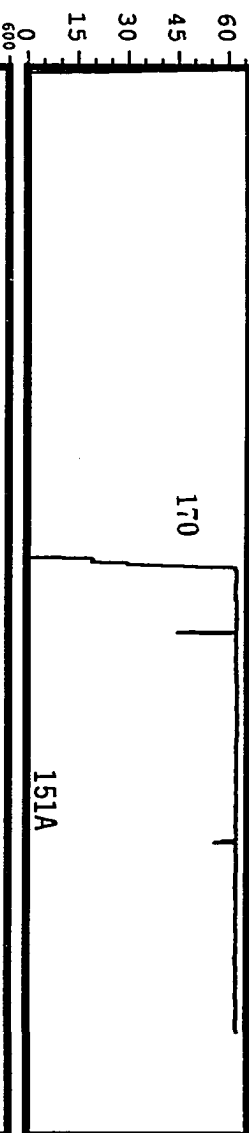
DECEMBER
1988



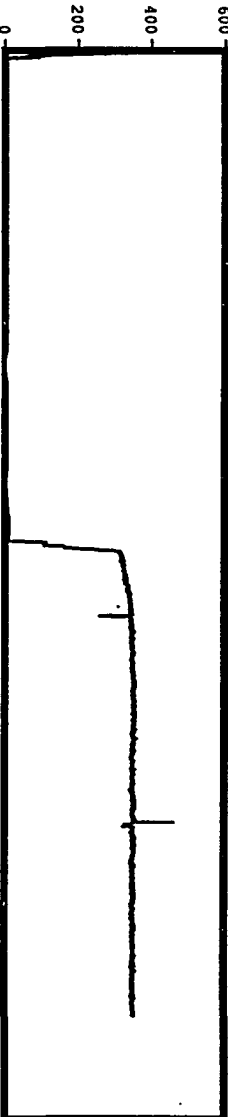
JANUARY
1989



POWER, MWt



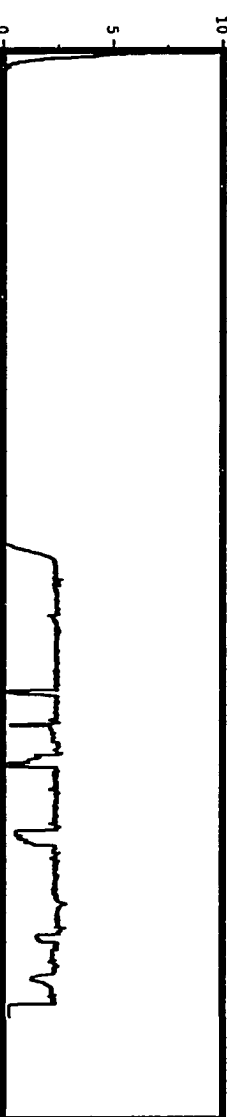
DN, cps



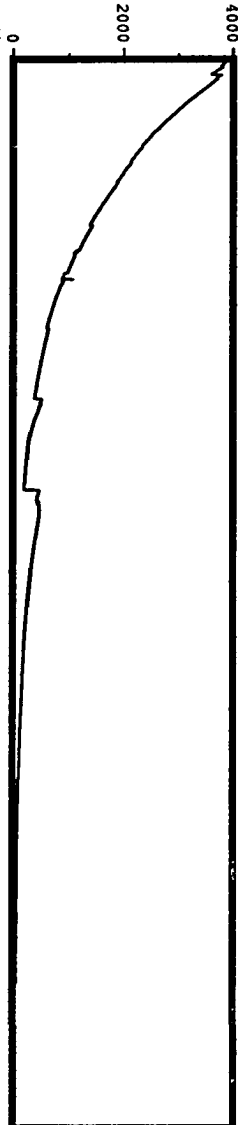
XE-135M, nCi/ml



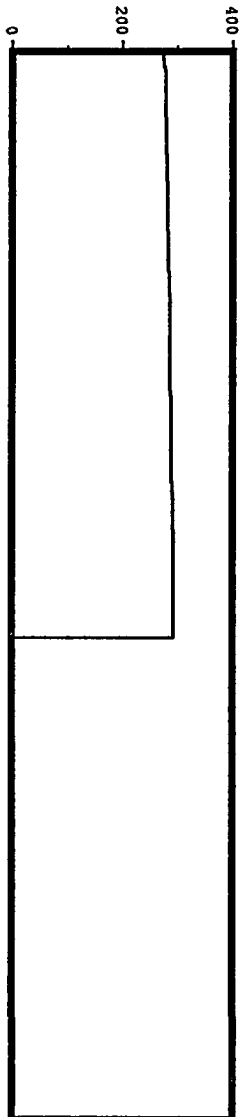
KR-87, nCi/ml



XE-133, nCi/ml



CUM XE-133, Ci

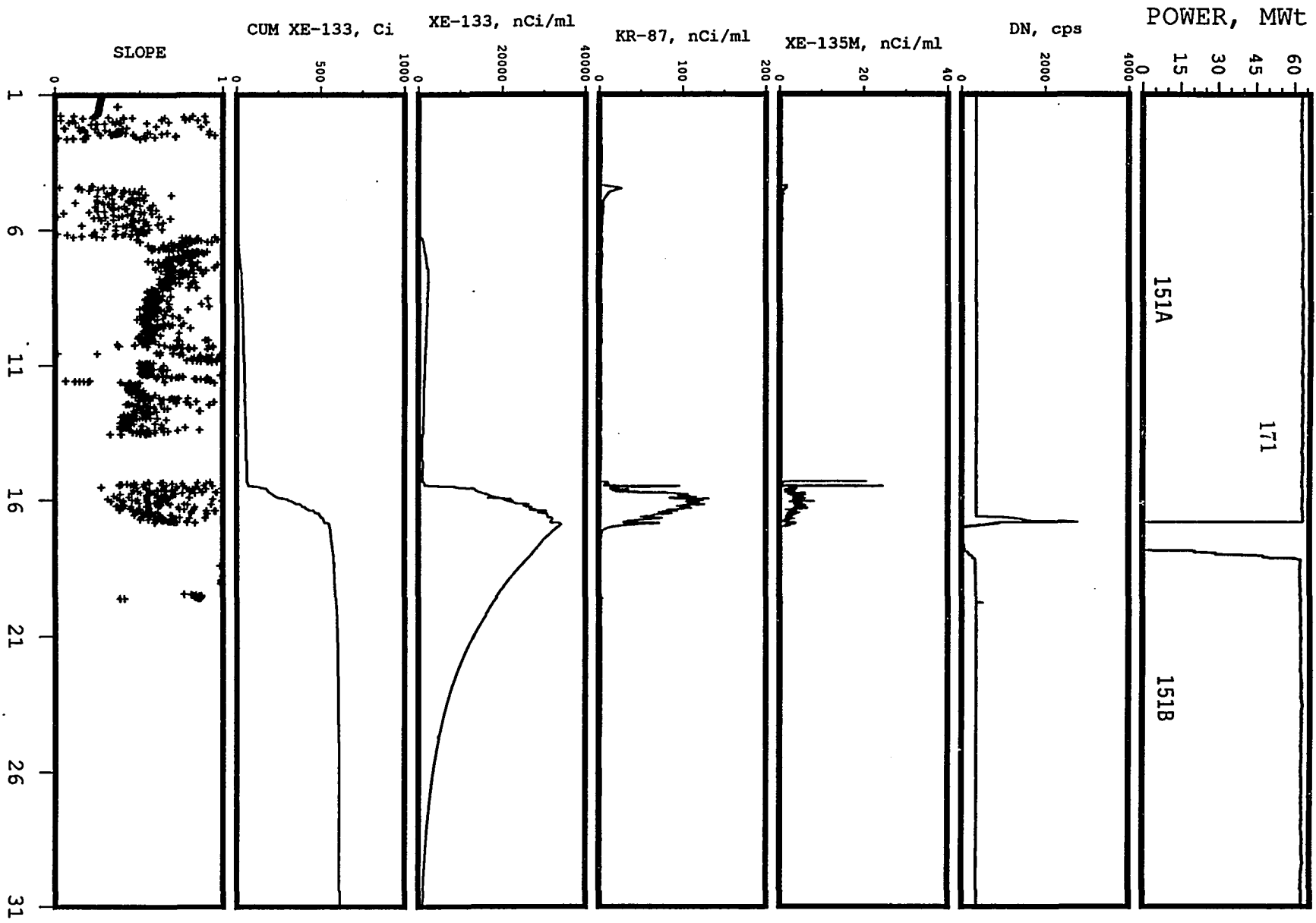


SLOPE

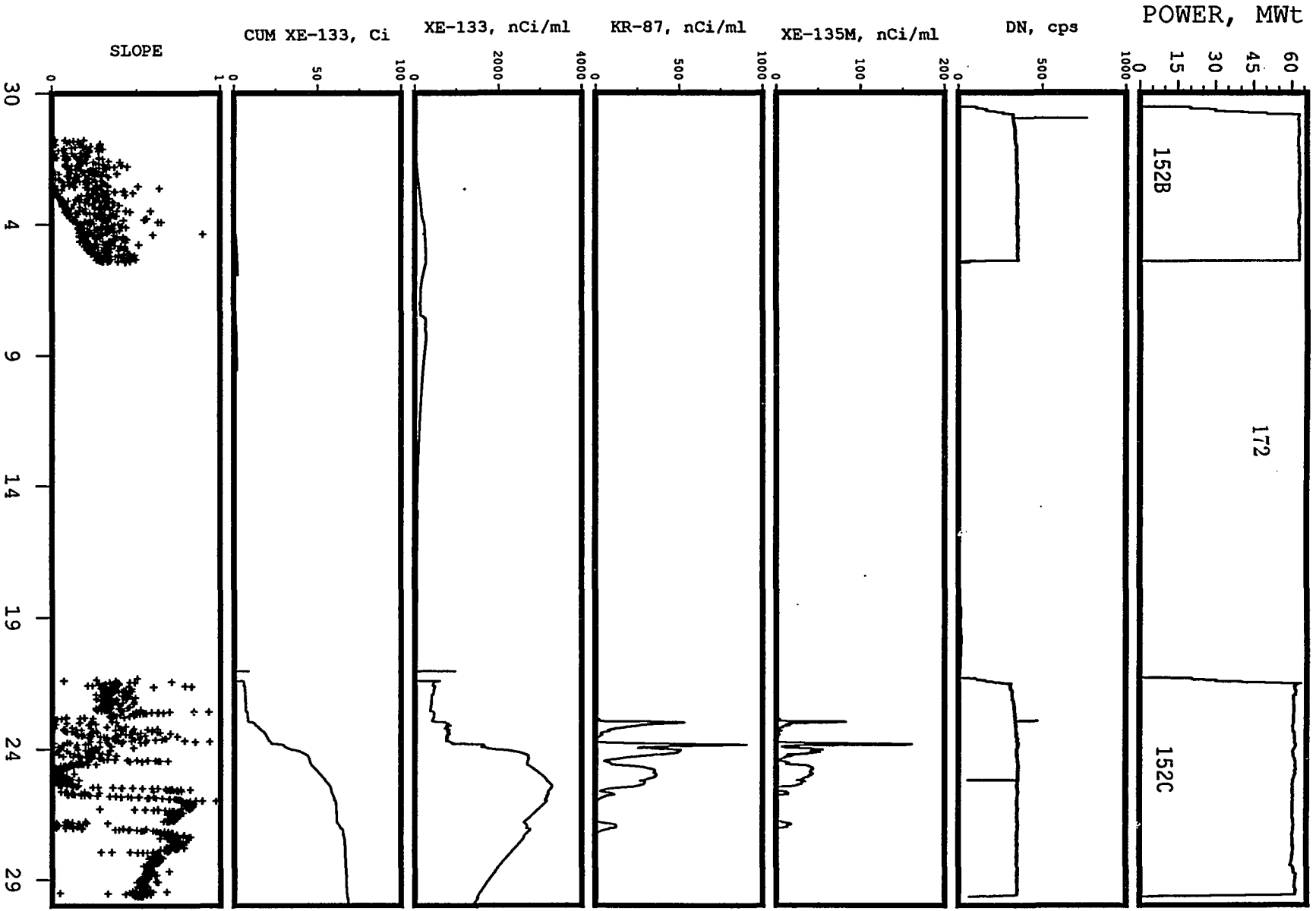


FEBRUARY
1989

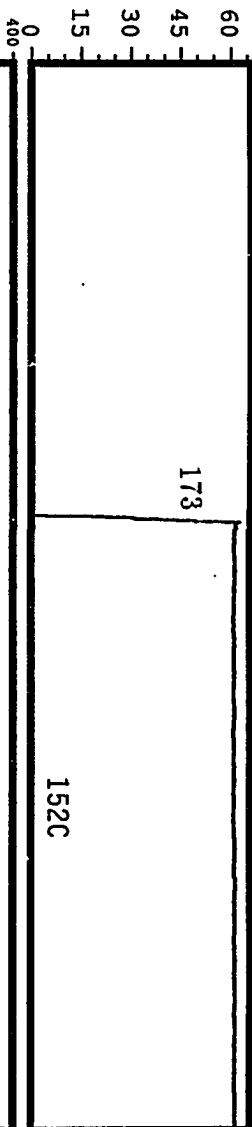
MARCH
1989



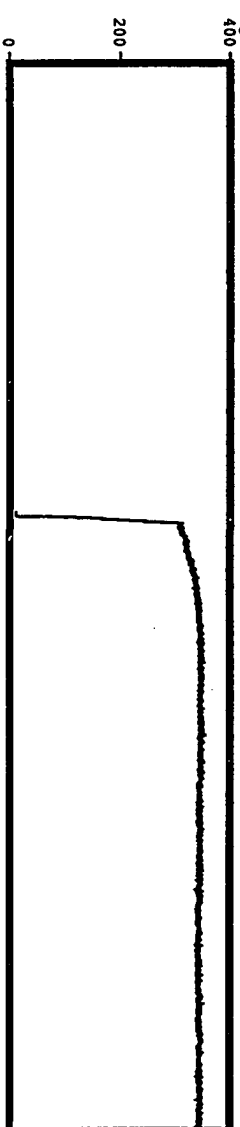
NOVEMBER
1989



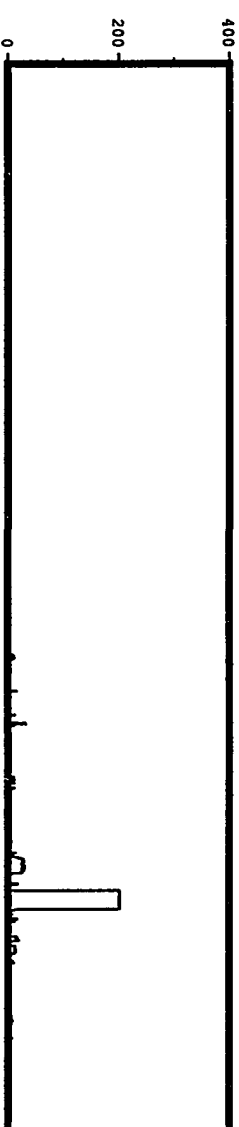
POWER, MWt



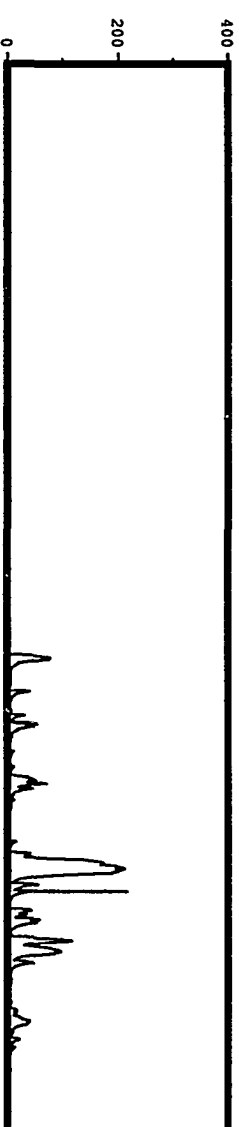
DN, cps



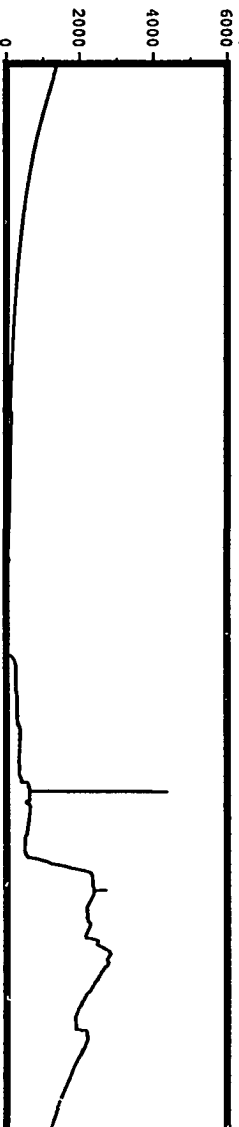
XE-135M, nCi/ml



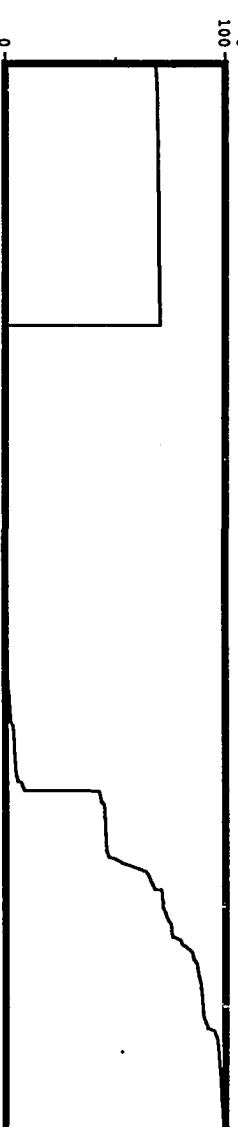
KR-87, nCi/ml



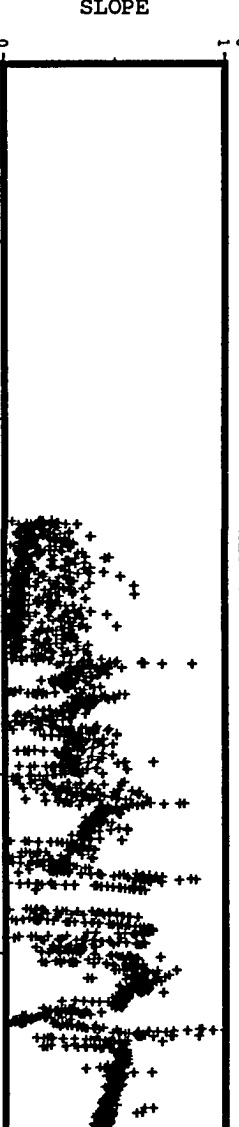
XE-133, nCi/ml



CUM XE-133, Ci

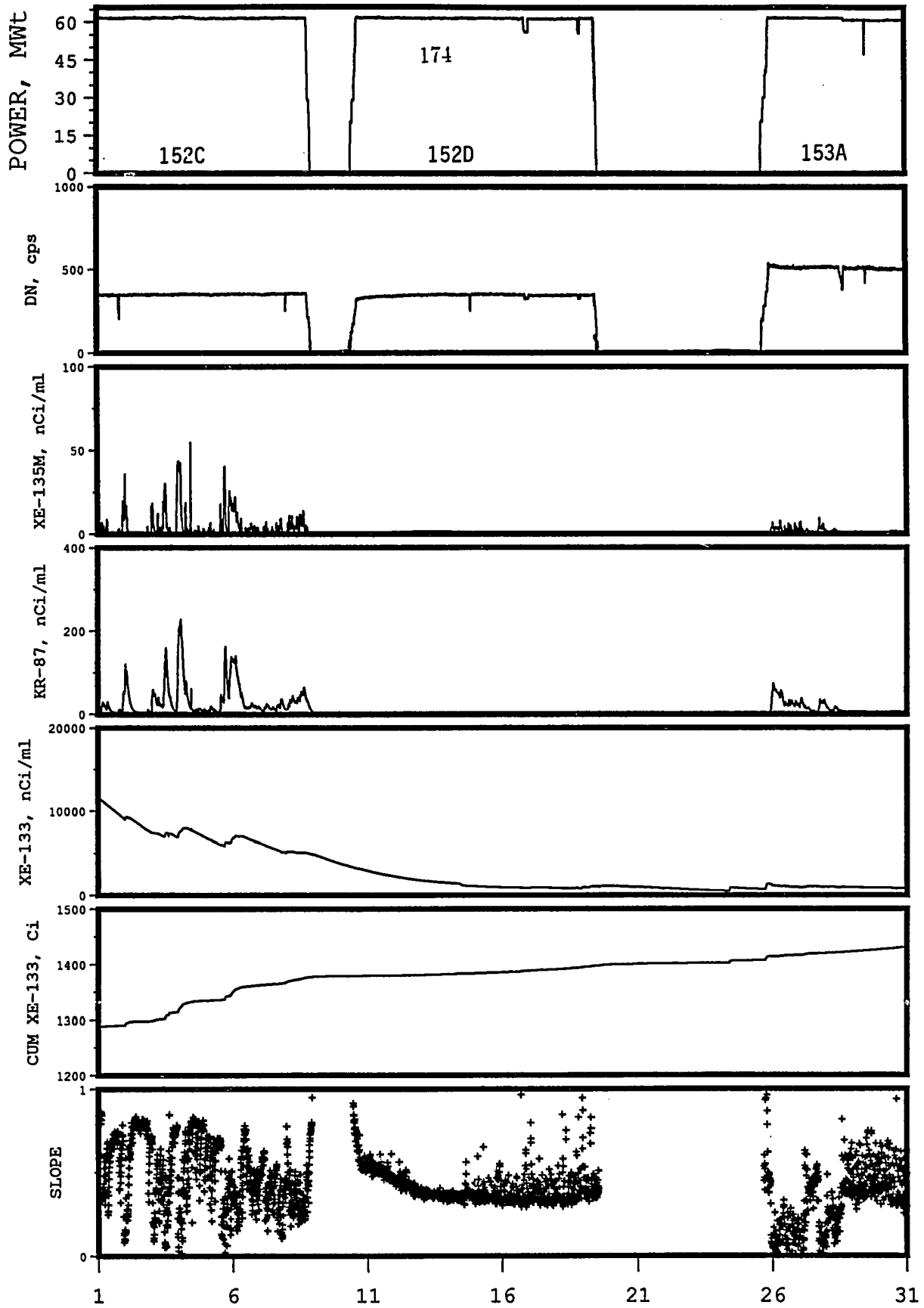


SLOPE



1 6 11 16 21 26 31

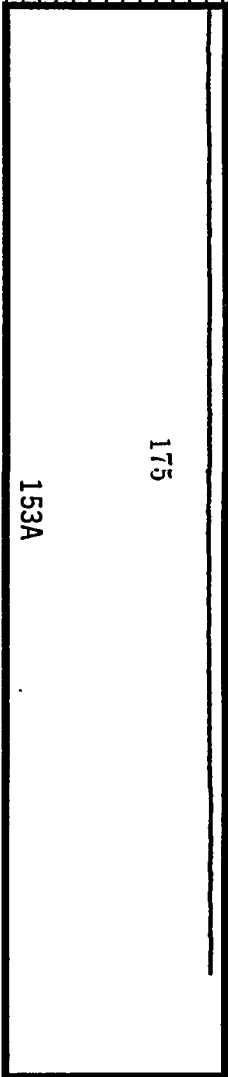
DECEMBER
1989



JANUARY
 1990

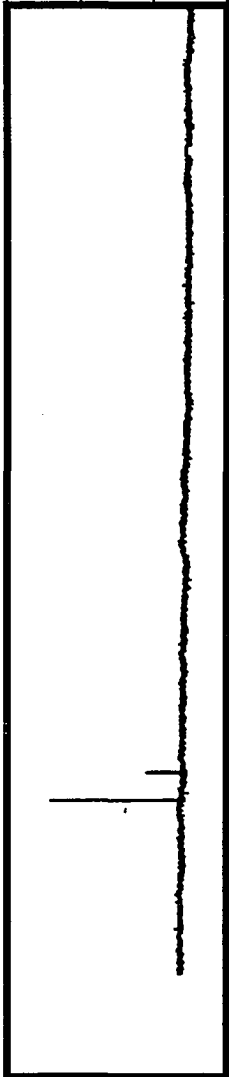
POWER, MWt

60
45
30
15
0



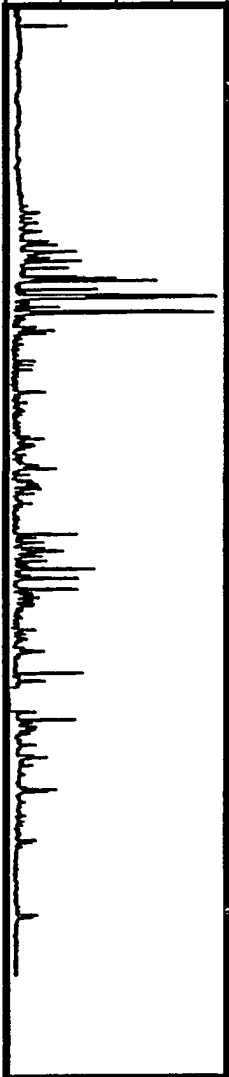
DN, cps

200
400



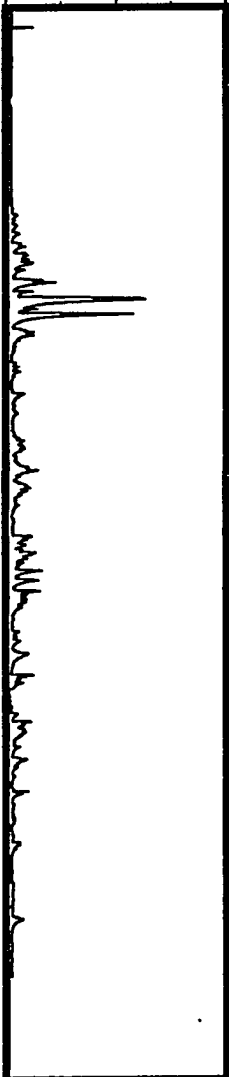
XE-135M, nCi/ml

0
10
20



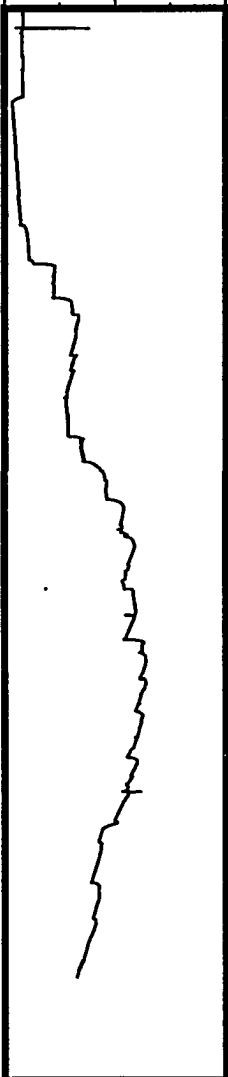
KR-87, nCi/ml

0
100
200



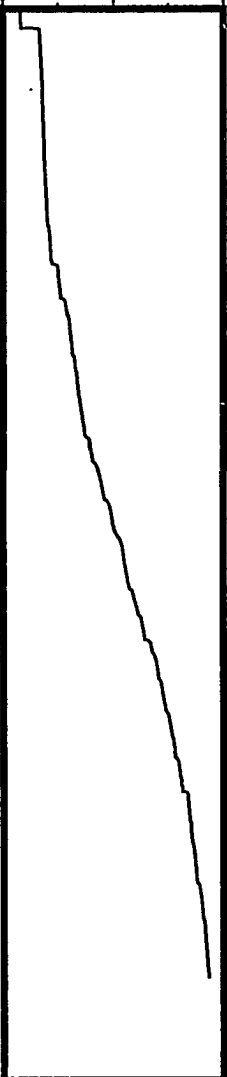
XE-133, nCi/ml

0
5000
10000



CUM XE-133, Ci

1400
1600
1800



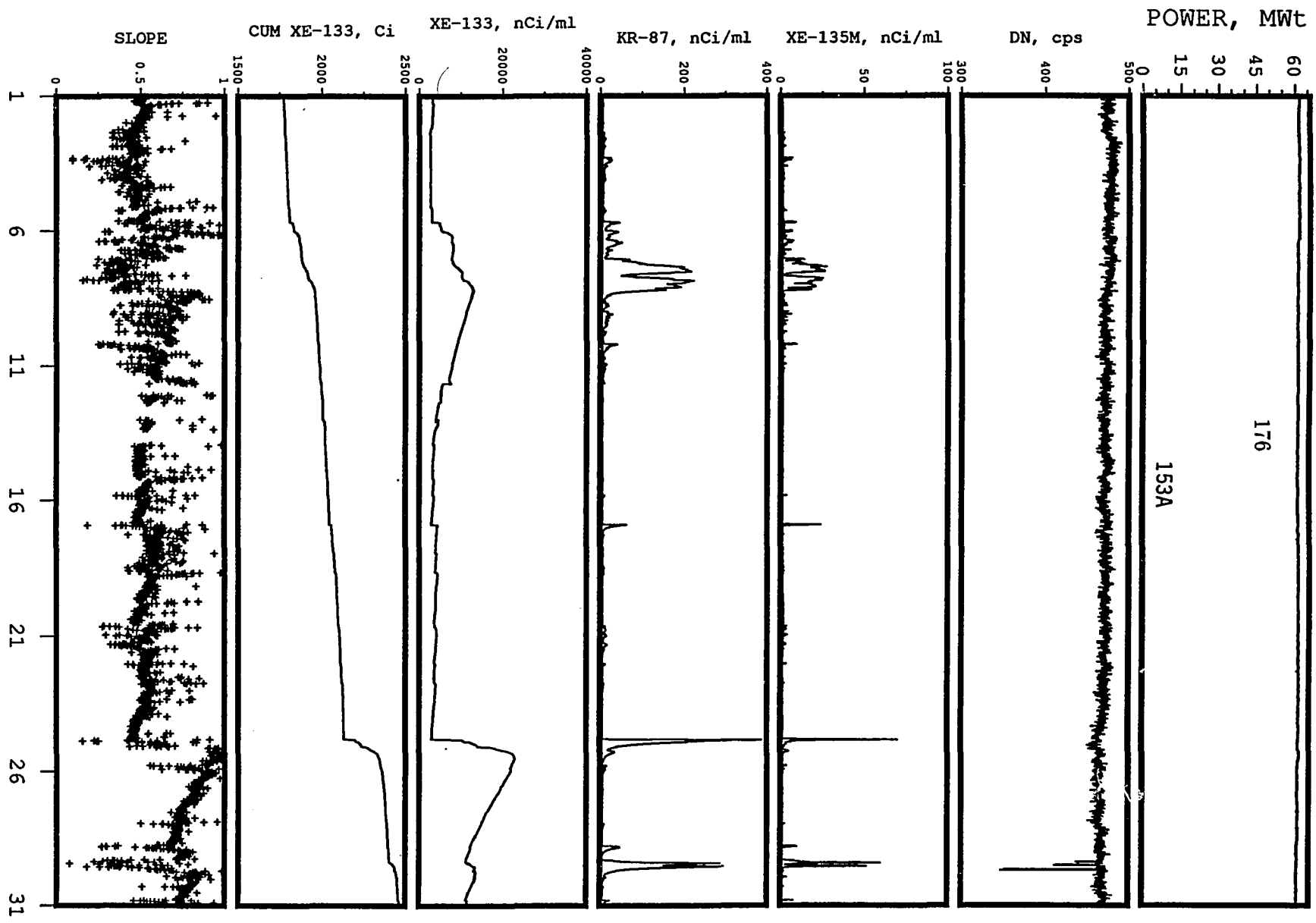
SLOPE



1
6
11
16
21
26

FEBRUARY
1990

MARCH
1990



APRIL
1990

